Federal University of Rio Grande do Sul
School of Engineering
Postgraduate Program in Civil Engineering

Constitutive modelling of fibre-reinforced sands under cyclic loads

Anderson Peccin da Silva

Porto Alegre
2017

ANDERSON PECCIN DA SILVA

CONSTITUTIVE MODELLING OF FIBRE-REINFORCED SANDS UNDER CYCLIC LOADS

Dissertation presented to the Postgraduate Program in Civil Engineering of the Federal University of Rio Grande do Sul as part of the requirements of the Degree of Master in Engineering.

Porto Alegre
2017

CIP - Catalogação na Publicação

Silva, Anderson Peccin da
Constitutive modelling of fibre-reinforced sands under cyclic loads / Anderson Peccin da Silva. -- 2017.
139 f.

Orientador: Nilo Cesar Consoli.
Coorientador: Lucas Festugato.

Dissertação (Mestrado) -- Universidade Federal do Rio Grande do Sul, Escola de Engenharia, Programa de Pós-Graduação em Engenharia Civil, Porto Alegre, BR-RS, 2017.

1. Constitutive modelling. 2. cyclic loads. 3. liquefaction. 4. fibre-reinforced sands. I. Consoli, Nilo Cesar, orient. II. Festugato, Lucas, coorient. III. Título.

Elaborada pelo Sistema de Geração Automática de Ficha Catalográfica da UFRGS com os dados fornecidos pelo(a) autor(a).

ANDERSON PECCIN DA SILVA

CONSTITUTIVE MODELLING OF FIBRE-REINFORCED SANDS UNDER CYCLIC LOADS

This Master's dissertation was assessed by the Board of Examiners and was considered suitable for obtaining the title of MASTER IN ENGINEERING, in the field of Geotechnical Engineering. Its final version was approved by the supervising professor and the Postgraduate Program in Civil Engineering of the Federal University of Rio Grande do Sul.

Porto Alegre, January 20th 2017.

Prof. Nilo Cesar Consoli
PhD, Concordia University, Canada
Supervisor

Prof. Lucas Festugato
D. Eng. UFRGS, Brazil
Supervisor

Prof. Carlos Torres Formoso
PPGEC/UFRGS Coordinator

BOARD OF EXAMINERS

Prof. Fernando Schnaid (UFRGS)
PhD, University of Oxford, UK

Prof. Karla Salvagni Heineck (UFRGS)
D. Eng. UFRGS, Brazil

Prof. Michéle Dal Toé Casagrande (PUC-Rio)
D. Eng. UFRGS, Brazil

To my parents, Alaor and Marines.

ACKNOWLEDGEMENTS

I wish to express my gratitude to Professor Nilo Consoli for his supervision, knowledge and continuous encouragement during the development of this research. His enthusiasm and optimism were essential to achieve the final aims of my dissertation and to shape my career goals so far.

I would like to thank Dr Lucas Festugato for the patience and guidance in supervising not only this research but also all my laboratory work that lead to fruitful results.

I wish to express my sincere thanks to Dr Andrea Diambra from the University of Bristol for all his help, guidance and patience during the development of this work. Despite the distance, the time zone difference and the language barriers, Dr Diambra was always there to help me and provide invaluable advice either by Skype or by email. The implementation of the Matlab code would not have been possible without his assistance.

I want to thank all my Master colleagues who somehow helped me towards this achievement, especially my friends “Los Gaveteros” (Francisco, Jonatas and Larissa). The many afternoons of group study were indispensable to me. Special thanks to Alejandro Quiñonez and Jorge Florez for their help at the laboratory.

Also, acknowledged is expressed to UFRGS and PPGEC for giving me the opportunity of studying in such a qualified University and Programme; to CAPES and CNPq for sponsoring me during my research.

I also would like to thank Cecília, who always supported me and gave uncountable moments of joy in the last 3 years. Her love and company made me forget all the struggle I faced to conclude this research.

Finally, I would like to thank my family and friends for your support and apologize for my absence during the last 2 years, especially my parents Alaor and Marines and my sister Caroline. The values and the education you provided me allowed me to pursue all my achievements.

The only place where success comes before work is in the dictionary.

Vince Lombardi

ABSTRACT

PECCIN DA SILVA, A. **Constitutive modelling of fibre-reinforced sands under cyclic loads.** 2017. Master's Dissertation (Master of Engineering) – Postgraduate Program in Civil Engineering, Federal University of Rio Grande do Sul, Porto Alegre.

Cyclic loads are induced by several sources, such as traffic, waves, wind and earthquakes. Particularly in the last years, more attention has been given to such loading conditions due to the development of the offshore engineering. Additionally, ground improving techniques have been employed to alter the characteristics of natural soils in order to increase its strength and delay – or avoid – liquefaction. Previous studies have developed complete constitutive laws for fibre-reinforced sands under monotonic loading conditions, but no previous work on modelling granular soils under cyclic loading has been reported. Hence, this research develops and validates a new constitutive modelling which is capable to fully assess the behaviour of fibre-reinforced soils under cyclic loads for undrained conditions. This model is based on two previous models developed by Diambra et al. (2013) and Diambra and Ibraim (2014), which employed a homogenisation technique to scale sand and fibre contribution. The behaviour of the sand follows the Severn-Trent Sand Model proposed by Gajo and Muir Wood (1999). Once the model is structured and its calculation procedure is defined, a parametric analysis is carried out in order to show the influence of each fibre and sand parameter in the composite response. An adjustment factor to account for the change in the interparticle forces caused by the fibres is proposed. Finally, the model is calibrated with experimental results and an analysis of its competences and limitations is performed. The calibration process showed that the model is able to capture important trends caused by the fibre reinforcement, such as a reduction in axial strain and in pore pressure generation, delaying the occurrence of liquefaction. The proposed model was shown to be more effective in reproducing the response of loose sands, i.e. those whose stress states are above the critical state line.

Keywords: *cyclic loading; liquefaction; fibre-reinforced sands; constitutive modelling.*

RESUMO

PECCIN DA SILVA, A. **Modelagem constitutiva de areias reforçadas com fibras sob carregamento cíclico.** 2017. Dissertação (Mestrado em Engenharia) – Programa de Pós-Graduação em Engenharia Civil, Universidade Federal do Rio Grande do Sul, Porto Alegre.

Carregamentos cíclicos são causados de diversas maneiras, como tráfego de veículos, ondas, vento e terremotos. Nos últimos anos, particularmente, tem-se aumentado o número de estudos para este tipo de carregamento devido ao desenvolvimento da engenharia offshore. Além disso, técnicas de melhoramento de solos granulares têm sido empregadas para alterar as características dos solos naturais, com o objetivo de aumentar sua resistência e retardar - ou evitar - a ocorrência de liquefação. Alguns estudos anteriores desenvolveram leis constitutivas completas para areias reforçadas com fibras sob carregamento monotônico, mas não são encontrados na literatura trabalhos sobre a modelagem deste tipo de solos sob carregamentos cíclicos. Sendo assim, essa dissertação desenvolve e valida um novo modelo constitutivo capaz de avaliar o comportamento de solos granulares reforçados com fibras sob carregamento cíclico sob condições não-drenadas. Este modelo é baseado em dois modelos previamente desenvolvidos por Diambra et al. (2013) e Diambra e Ibraim (2014), que utilizam uma técnica de homogeneização para considerar a contribuição da areia e das fibras. O comportamento da areia segue o Modelo Severn-Trent Sand, proposto por Gajo e Muir Wood (1999). Uma vez estruturado o modelo e definido seu procedimento de cálculo, realiza-se uma análise paramétrica, a fim de demonstrar a influência de cada parâmetro das fibras e da areia no comportamento do compósito. Um fator de ajuste para levar em consideração a mudança nas forças interparticulares causada pelas fibras é proposto neste trabalho. Ao final, o modelo é calibrado com resultados experimentais e faz-se uma análise de suas competências e limitações. O processo de calibração mostrou que o modelo é capaz de capturar importantes tendências causadas pela inserção de fibras, como a redução nas deformações axiais e na geração de poropressões, retardando a ocorrência de liquefação. O modelo proposto mostrou-se mais efetivo em reproduzir o comportamento de areias fofas, ou seja, aquelas cujo estado de tensões se encontra acima da linha do estado crítico.

Palavras-chave: *carregamento cíclico; liquefação; areias reforçadas com fibras; modelo constitutivo.*

LIST OF FIGURES

LIST OF TABLES

LIST OF SYMBOLS AND ABBREVIATIONS

a_{sf} - adhesive bond between sand and fibre surface

A – multiplier in flow rule

AF – adjustment factor

b – distance between the yield and strength surfaces

b_{max} – maximum value that b can assume

B – parameter controlling hyperbolic stiffness relationship

CSL – critical state line

d – stress-dilatancy relationship

d_f – fibre diameter

$\mathbf{D}^e$ – elastic matrix

e – void ratio

E – Young's elastic modulus

E_f – elastic modulus of the fibres

f – yield function

f_b – sliding function between fibres and sand grains

F – bounding surface function

g – plastic potential

G – shear modulus

G_f – specific gravity of the fibres

G_s – specific gravity of the sand

H – hardening parameter

I_D – relative density index

k_r – link between changes in state parameter and current strength

k_d – state parameter contribution in flow rule

K – bulk modulus

l_f – fibre length

L – vector of unknowns

m – unit direction of plastic flow

m_c, m_e – slope of the yield locus with respect to its axis on the compression/extension side

M_b – slope of the bounding strength surface

M_c, M_e – stress ratio at critical state in compression/extension

M^* – relationship between distortional strain and volumetric strain

N_{cyc} – total number of cycles

$\mathbf{n}$ – unit vector normal to the yield surface

p – mean stress of the composite

p^* – effective mean stress of the composite

q, q^* – deviatoric stress of the composite

q_{up}, q_{down} – higher and lower stress value of the cycle

r – ratio of sizes of strength surface and critical state surface

R – ratio of sizes of yield surface and strength surface

s – isotropic component of $\boldsymbol{\sigma}$, with respect to $\boldsymbol{\alpha}$

t – deviatoric component of $\boldsymbol{\sigma}$, with respect to $\boldsymbol{\alpha}$

u – pore water pressure

w_f – fibre content in terms of volume

$\boldsymbol{\alpha}$ – unit vector defining the direction of the axis of the yield surface

ς – damage rule parameter

δ_{sf} – friction component on the interface between fibres and grains

$\boldsymbol{\varepsilon}$ – vector defining the strains in the composite

$\boldsymbol{\varepsilon_f}$ – vector defining the strains in the fibres

$\boldsymbol{\varepsilon_m}$ – vector defining the strains in the matrix

ε_a – axial strains

ε_q – distortional strains

ε_r – radial strains

ε_v – volumetric strains

ε_θ – strain in the composite in the direction θ

$\varepsilon_{\theta f}$ – strain in the fibres in the direction θ

ξ – state parameter

φ' – peak friction angle

φ_{cs} – critical state friction angle

φ_y – friction angle of the yield surface

λ – slope of the critical state line on υ_m - ln p' plane

κ – elastic parameter of Cam Clay

μ – Poisson's ratio

η – effective stress ratio

$\bar{\rho}$ – average volumetric concentration of fibres

$\rho(\theta)$ – volume concentration of fibres as function of the angle θ

ψ – dilatancy angle

$\boldsymbol{\sigma}$ – vector defining the stress state of the composite

$\boldsymbol{\sigma^*}$ – vector defining the effective stress state of the composite

$\boldsymbol{\sigma'}$ – vector defining the stress state of the matrix

σ_a, σ_r – axial/radial stress of the composite

$\boldsymbol{\sigma_c}$ – image stress vector

σ_f^L – pull-out stress of the fibres

σ_θ – stress in the composite in the direction θ

$\sigma_{\theta f}$ – stress in the fibres in the direction θ

ζ – multiplier in the adjustment factor

Γ – intercept for critical state line on υ_m - ln p' plane at p'=1 kPa

υ – specific volume of the composite

υ_f – specific volume of the fibres

υ_m – specific volume of the matrix

SUMMARY

1 INTRODUCTION

Soil materials have been widely used to build engineering systems such as embankments, dams, road and railway subgrades and foundations for buildings. With the twentieth and twenty-first century development of the cities, the construction works started taking place in areas where the behaviour of the soil would not match the characteristics needed for engineering uses. Therefore many techniques have been employed in order to improve the soil characteristics and make its behaviour more adequate.

The techniques of ground improvement have been employed for repairing failed slopes, stabilizing thin layers of soil and strengthening the soil around footings (DIAMBRA et. al, 2010). These techniques have also been used to improve the behaviour of soils subjected to cyclic loading conditions. Cyclic loads have been traditionally induced by different sources, such as traffic, industrial sources, repeated filling and emptying operations and environmental sources such as earthquakes, waves and wind (WICHTMANN; TRIANTAFYLLIDIS, 2012). However, in the last years more attention has been given to such loading conditions due to the increasingly development of the offshore engineering sector (CORTI, 2016).

Including tension resisting elements and adding cementing agents have been the most important techniques ever since practicing engineers first tried to stabilize near surface soil layers (DIAMBRA et al., 2010). The behaviour of these kinds of artificially reinforced soils has been broadly studied by many authors worldwide and notably at the Postgraduate Program in Civil Engineering (PPGEC) at the Federal University of Rio Grande do Sul (UFRGS) (e.g. ULBRICH, 1997; FEUERHARMEL, 2000; CASAGRANDE, 2001; CASAGRANDE, 2005; FESTUGATO, 20015; FESTUGATO, 2011).

Most of the work done so far has focused on the experimental analysis concerning shear strength, and some studies have shown the fibre reinforced soils' response when loaded under cyclic conditions.

In addition to the aforementioned experiments, many authors have proposed modelling approaches for predicting the contribution of the fibres to shear strength, however fewer authors have tried to introduce a general constitutive law for reinforced soils (DIAMBRA et al., 2010).

On the other hand, Corti (2016) has proposed a constitutive modelling framework to predict the behaviour of granular soils subjected to cyclic loadings. Nevertheless, no previous studies are found in the literature concerning the constitutive modelling of fibre reinforced soils under cyclic loading conditions.

In this context, this research aims to propose a constitutive model for predicting the triaxial behaviour of granular soils under cyclic loading conditions, using the concepts proposed by Gajo and Muir Wood (1999) and matching the models proposed by Diambra et al. (2013) and Diambra and Ibraim (2014).

1.1 RESEARCH OBJECTIVES

The main objective of this research is to develop and validate a new constitutive model to predict the response of fibre reinforced sands under cyclic loads.

The specific objectives are summarized below:

a) To evaluate the range of applicability of the model regarding soil parameters and initial conditions.

b) To validate the model by comparing its results with tests performed at different initial conditions and different sands.

1.2 RESEARCH STRUCTURE

After this introductory chapter, which aims to present the motivations and objectives for the here presented research, Chapter 2 presents the literature review, including previous constitutive models for – reinforced and non-reinforced – granular soils and experimental results for fibre reinforced soils. Chapter 3 describes the model structure and the calculation procedure. Chapter 4 plays a parametric analysis of the proposed model and Chapter 5 validates the model by comparing its results with experimental data from previous works. Finally, Chapter 6 presents the concluding remarks of the present research.

1.3 NOTATION

The notation adopted in this research is conveniently developed for axisymmetric triaxial conditions, once the whole outline of this thesis is based on triaxial tests. The stress states are defined by the vector $\boldsymbol{\sigma}$, as defined on equation (1.1), and the strains are defined by equation $\boldsymbol{\varepsilon}$ on equation (1.2).

$$\boldsymbol{\sigma} = \begin{bmatrix} p \\ q \end{bmatrix} \tag{1.1}$$

$$\boldsymbol{\varepsilon} = \begin{bmatrix} \varepsilon_v \\ \varepsilon_q \end{bmatrix} \tag{1.2}$$

where p is the mean stress; q is the deviatoric stress; ε_v is the volumetric strain and ε_q is the distortional strain. These stress and strain quantities are related to axial and radial stresses and strains according to equations (1.3) to (1.6).

$$q = \sigma_a - \sigma_r \tag{1.3}$$

$$p = \left(\frac{\sigma_a + 2\sigma_r}{3}\right) \tag{1.4}$$

$$\varepsilon_q = \frac{2}{3}(\varepsilon_a - \varepsilon_r) \tag{1.5}$$

$$\varepsilon_v = (\varepsilon_a + 2\varepsilon_r) \tag{1.6}$$

where σ_a is the axial stress, σ_r is the radial stress, ε_a is the axial strain and ε_r is the radial strain.

Compression is assumed positive along the research, both for representing stress and strain. The void ratio of soils is defined by equation (1.7).

$$e = \frac{V_v}{V_s} \tag{1.7}$$

where e is the void ratio; V_v is the total volume of voids and V_s is the total volume of solids. The specific volume (υ) is given by $\upsilon = 1 + e$ and it is linked to volumetric strains in the incremental form, as presented on equation (1.8).

$$\dot{\varepsilon}_v = -\frac{\dot{\upsilon}}{\upsilon} \tag{1.8}$$

where $\dot{\varepsilon}_v$ is the incremental volumetric strain and $\dot{\upsilon}$ is the incremental specific volume.

Effective stresses are denoted by the variables p^* and q^*. The effective deviatoric stress (q^*) is the same as the total deviatoric stress (q) whereas the effective mean stress (p^*) is given by equation (1.9).

$$p^* = p - u \tag{1.9}$$

where u is the pore water pressure.

All the variables in the equations above may or may not be followed by the subscripts '$_m$' or '$_f$', denoting matrix and fibres. In order to make the notation clearer, a summary of stresses and strains is presented on Table 1.1.

Table 1.1 – Summary of the notation adopted in this research

	Stresses		Strains
	Total	Effective	
Composite	$\boldsymbol{\sigma} = [p, q]^T$	$\boldsymbol{\sigma}^* = [p^*, q^*]^T$	$\boldsymbol{\varepsilon} = [\varepsilon_v, \varepsilon_q]^T$
Matrix	–	$\boldsymbol{\sigma'} = [p', q']^T$	$\boldsymbol{\varepsilon_m} = [\varepsilon_{mv}, \varepsilon_{mq}]^T$
Fibres	–	$\boldsymbol{\sigma_f} = [p_f, q_f]^T$	$\boldsymbol{\varepsilon_f} = [\varepsilon_{fv}, \varepsilon_{fq}]^T$

The word "liquefaction" will be widely employed during this research. Therefore, it is important to define the two criteria to define the occurrence of this phenomenon. In this research, the criteria to define liquefaction are those defined by Ishihara (1996):

a) 100% pore water pressure build-up (effective mean pressure *p'*=0); or

b) 5% axial strain.

These criteria will be referred to as "1st Ishihara's criterion" (a) and "2nd Ishihara's criterion" (b). In certain situations, these criteria will be used as failure criterion. That happens because for denser sands liquefaction is not likely to occur. Further details will be given in Chapter 5.

2 LITERATURE REVIEW

2.1 INTRODUCTION

The action of fibres for improving the engineering properties of soils has been largely observed in nature over the years, especially through the presence of plant roots. Early studies by Waldron (1977) showed that the inclusion of plant roots into the soil on slopes increased shearing resistance to as much as 5 times that of uncultivated soil. Also, Wu et al. (1979) analysed the stability of slopes before and after removal of forest covers and reported the reduction in the shear strength of the soil caused by the decay of tree roots. Such an approach, despite being appropriate for analysing slope stability, may not be adequate for evaluating the soil behaviour due to the addition of fibres (MICHALOWSKI; ZHAO, 1996).

More recently, the inclusion of fibres has also been employed in a wide range of situations, such as embankments and subgrade stabilization beneath footings and pavements (GRAY; OHASHI, 1983). In the last decades the geosynthetics have emerged as an important engineering material as it has a wide range of applications, with many advantages over the previous technologies: the quality control, as they are manufactured in a factory environment; the easy and rapid installation; the competitive cost against other construction materials; the regulation of its use in many cases (KOERNER, 2012). Still, several authors have reported the addition of randomly distributed short fibres as an effective and cost effective technique for improving the strength of near surface soil layers, even in field application (FEUERHARMEL, 2000; CONSOLI et al., 2003; CASAGRANDE, 2005; HEINECK et al., 2005; CONSOLI et al., 2009a; DIAMBRA, 2010).

In spite of all the previous research on the behaviour of fibre reinforced soils under static loading, little has been studied on the effects of the addition of tension resisting elements in soils subjected to cyclic loading conditions, and there are as yet little studies on constitutive modelling of soils under such conditions.

So, this chapter aims not only to present the previous works on the response of fibre reinforced soils under cyclic loading, but also to expose the constitutive models which are relevant to the present research.

2.2 MECHANICAL BEHAVIOUR OF FIBRE REINFORCED SOILS

Fibre reinforced soils are part of a group of materials named composite materials. These mixtures of two or more different materials are composed of two phases: the matrix (concrete, soil, etc.) and the reinforcement element (fibres, steel, etc.). They are developed to optimize the strong points of each of these phases (BUDINSKI, 1996).

The mechanical response of the soil-fibre composite depends on the fibre content (weight ratio between fibres and soil), the characteristics of the fibres (mechanical properties, length, shape and material) as well as on the properties of the soil matrix (CURCIO, 2008). These remarks confirm the postulates of Hannant (1994), who observed that the performance of fibre reinforced soils is controlled mainly by the fibre content, the length of the fibres, the physical properties of fibre and matrix and the bond between the two phases. Still, Johnston (1994) adds the effect of fibre orientation and the distribution of the fibres in the matrix as important aspects regarding the composite behaviour.

The orientation of the fibres plays a fundamental role on their contribution to the overall behaviour of the soil-fibre system. Once the fibres are tension-resisting elements, only the ones oriented within the tensile strain domain of the sample can mobilize tensile stress and then contribute to the overall shear strength of the composite (DIAMBRA et al., 2013). So, depending on the application of the technique, it may be interesting to employ the fibres in a preferred orientation, using continuous planar synthetic inclusions such as geotextiles (KOERNER; WELSH, 1980). When the tensile strength is required in a wide range of orientations, short, flexible fibres randomly distributed throughout the soil mass are very effective as reinforcement elements (DIAMBRA et al., 2013).

Several test types can be carried out in order to better understand the influence of these many factors in the behaviour of fibre-reinforced soils. The main tests are described as follows.

2.2.1 Test types

The direct shear was one of the first tests employed to evaluate the inclusions in granular soil masses, as reported by McGown et al. (1978) and Gray and Ohashi (1983). Results mainly evidence the effectiveness of fibres in increasing the strain at failure, in reducing the peak strength loss and in increasing the peak strength of soils. This type of test has also been used in recent studies by Yetimoglu and Salbas (2003), who showed that the fibre reinforcements

reduced soil brittleness (confirming the reduction in the post-peak strength loss reported by the previous authors) and increased the residual shear strength angle.

Ring shear tests were performed in fibre reinforced sands by Heineck et al. (2005) and Consoli et al. (2007). The former showed that the reinforcement significantly influences the shear strength, even at very large displacements, while the latter observed that the increase was more pronounced for longer fibres, higher fibre contents and denser samples.

Heineck et al. (2005) also carried out an investigation on the initial stiffness of the composite with the bender element technique. This research suggests that the inclusions do not change the initial stiffness of those materials.

Consoli et al. (2005) carried out high-pressure isotropic compression tests on uniform sand at different void rations. This study showed that the fibres work under tension even under isotropic load, what was confirmed by exhumation after testing, showing that fibres had either extended or broken.

Despite these few studies using other apparatus, most of the research developed so far was based on triaxial tests. For this reason, this seems to be the more suitable test to be analysed in order to fully understand the influence of the initial conditions of the fibre-soil composite on tests response.

2.2.2 Drained triaxial tests

Most of the triaxial tests found in former studies were carried out under drained conditions. Some concluding remarks are common to nearly all the authors, whereas definitive conclusions regarding others aspects cannot be drawn.

The first important conclusion is that the inclusion of randomly distributed fibres increases the peak shear strength (RANJAN et al., 1996; MICHALOWSKI; ZHAO, 1996; CONSOLI et al., 1998) and hence the failure stress (GRAY; AL-REFEAI, 1986; MICHALOWSKI; CERMAK, 2003). This seems to be a well-accepted statement among all the authors. Michalowski and Cermak (2003) found that the increase in failure stress can be as much as 70% at a fibre concentration of 2% (by volume) whereas the effect drops to about 20% when this concentration is 0.5% (Figure 2.1). The same authors observed that the reinforcing effect is stronger in fine sands.

Another relevant remark is the one that the reinforcement reduces the post-peak loss of strength. This behaviour was reported by Gray and Al-Refeai (1986), by Ranjan et al. (1996) and by Teodoro and Bueno (1998), among others.

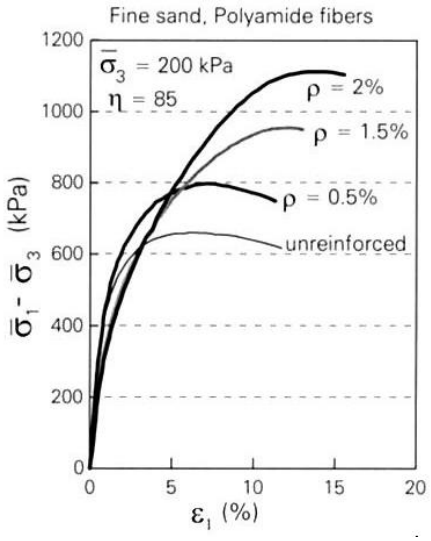

Figure 2.1 – Effect of fibre concentration on stress-strain behaviour (MICHALOWSKI; CERMAK, 2003)

It has also been observed that the fibre reinforcement causes a substantial increase of the strain to failure (MICHALOWSKI; ZHAO, 1996; GRAY; AL-REFEAI 1986; MICHALOWSKI; CERMAK, 2003). Conducting triaxial tests, Consoli et al. (1998) also showed that fibre reinforcement increase the residual strengths, confirming the conclusion observed by Yetimoglu and Salbas (2003) with direct shear tests.

Regarding the effect of fibre inclusions in the stiffness of samples, there does not seem to be a common statement in the literature. While some authors acknowledged that the inclusions caused an increase of the stiffness (LEE et al., 1973; GRAY; AL-REFEAI, 1986; FREITAG, 1986; MICHALOWSKI; ZHAO, 1996), others noticed the opposite behaviour (CONSOLI et al., 1998). According to Gray and Al-Refeai (1986), adding randomly distributed discrete fibres resulted in a loss of compressive stiffness at low strains (less than 1%). Still, Michalowski and Cermak (2003) observed the same drop in initial stiffness for synthetic fibres, but not for steel fibres. In more recent studies, Diambra et al. (2010) affirm that it seems to be clear that the effect of fibres become more important under medium and large strains and for this reason the inclusions do not influence the stiffness in some studies. More conclusive results were presented by Heineck et al. (2005), who showed that fibre inclusions did not influence the initial stiffness of soils ranging from a silty sand, a uniform sand and also a bottom ash.

The triaxial test apparatus also allows the determination of the volumetric behaviour of the samples. Hence the effect of the fibre reinforcement on dilation (the increase in volume during shearing) was studied by some authors. Drained triaxial tests carried out by Michalowski and Zhao (1996) and Michalowski and Cermak (2003) concluded that the presence of fibres inhibited the dilative behaviour soil. Oppositely, Diambra et al. (2010) showed that in both compression and extension the composite showed a more dilative response in relation to the unreinforced soil.

Figure 2.2 and Figure 2.3 depict the contrary dilative behaviour between these studies.

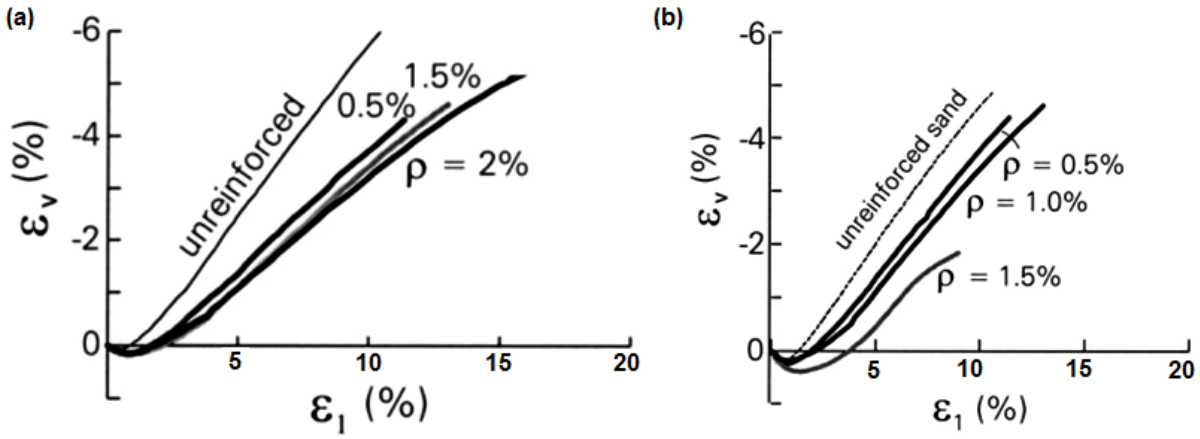

Figure 2.2 – Effect of reinforcement: reduction on the dilative behaviour for (a) fine and (b) coarse sand (MICHALOWSKI; CERMAK, 2003)

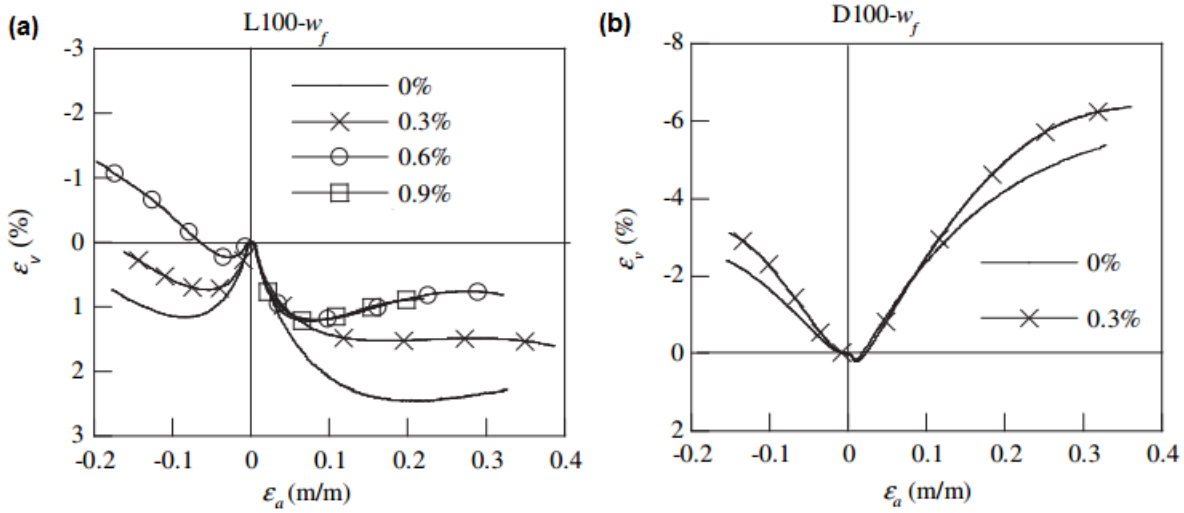

Figure 2.3 – Effect of reinforcement: increase on the dilative behaviour for (a) loose and (b) dense sand (DIAMBRA et al., 2010)

2.2.3 Undrained triaxial tests

The undrained behaviour of sands is of particular interest to the geotechnical engineering once it is associated with liquefaction. Liquefaction under monotonic undrained loading is also called static liquefaction and it commonly occurs in loose and very loose saturated sands and silty sands under low confining pressures. This phenomenon consists of a significant generation of pore pressure leading to a large reduction of mean effective pressure (IBRAIM et al., 2010).

To the author's knowledge, few studies are reported on the undrained behaviour of fibre reinforced sands. Some of these are presented as follows.

Ahmad et al. (2010) performed consolidated undrained (CU) tests on silty sands reinforced with oil palm fibres. This study suggested that there is not a clear effect of fibre inclusions on peak strength. However, the positive pore water pressure generated during shear increased with increasing the fibre content and fibre length, causing an increase in the shear strength of the reinforced sand. The inclusions also increased cohesive intercept and friction angle linearly with fibre content. Furthermore, the authors observed that fibre reinforcement restrains the dilatancy of the reinforced soil, as noticed in drained tests by Michalowski and Zhao (1996) and Michalowski and Cermak (2003).

However, the first extensive study on the undrained behaviour of fibre reinforced sands was carried out by Ibraim et al. (2010) and Diambra (2010). The authors found that the addition of fibres reduce the liquefaction potential in both compression and extension, but a higher concentration of inclusions is needed in extension. Still, it was shown that the inclusions convert a strain softening response (typical for loose unreinforced sands) into a strain hardening response. Some results of the aforementioned study are presented in Figure 2.4.

More attention has been addressed towards the cyclic undrained behaviour of reinforced sands. When subjected to undrained cyclic compression loading, reinforced specimens show an increased resistance if compared with unreinforced specimens (MAHER; HO, 1993). The number of cycles and the magnitude of strains required to reach failure is increased significantly as a result of fibre inclusion. In the case of undrained cyclic loading at small strains, fibre reinforced sands show a higher linear elastic modulus than unreinforced sands but the modulus deteriorates with loading repetition (LI; DING, 2002).

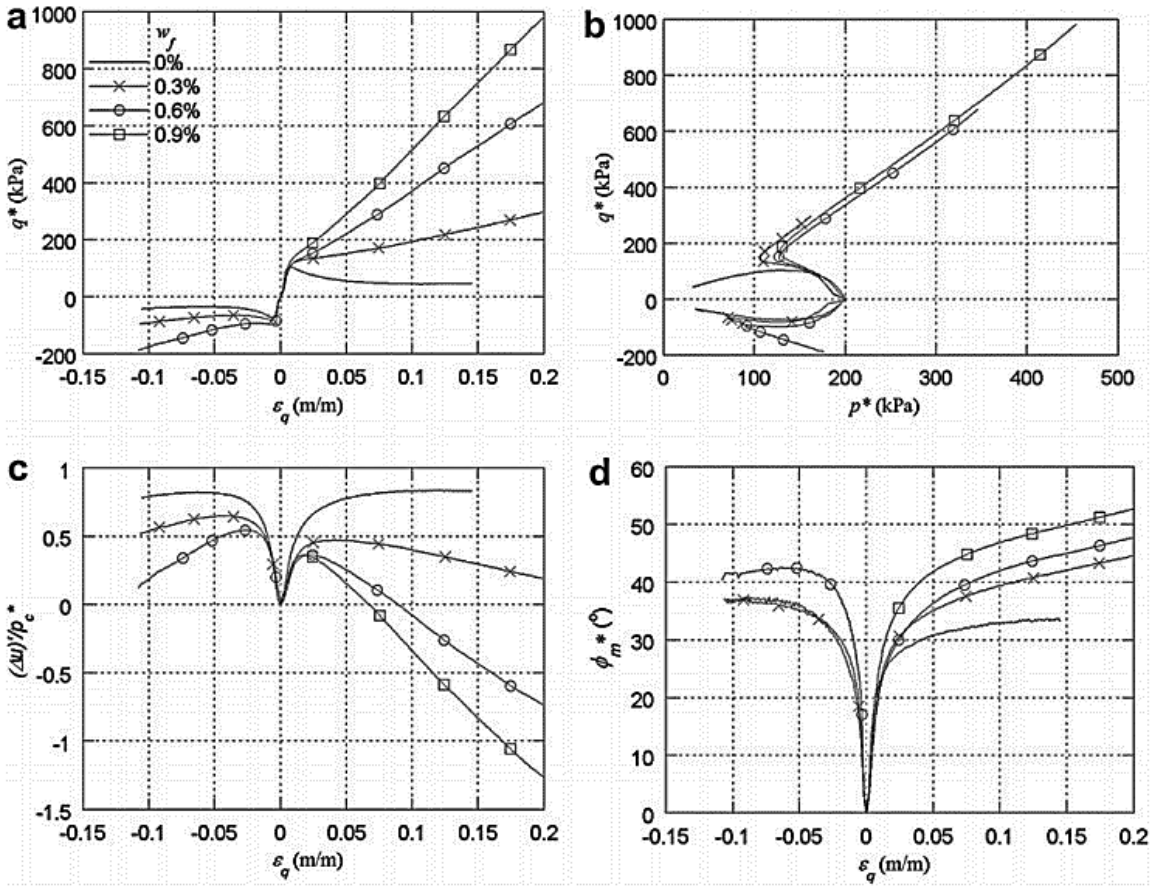

Figure 2.4 – Triaxial undrained compression and extension tests; 200 kPa initial confining pressure (IBRAIM et al., 2010)

2.2.4 Influence of test conditions

2.2.4.1 Confining stress

Several authors have reported the form of failure envelopes for randomly distributed fibre reinforced sands. The pioneering approach was given by Gray and Ohashi (1983) who observed that the shear envelopes for fibre reinforced sands tended to parallel the envelope for sand for confining stresses exceeding a threshold value, referred to as critical confining stress σ_{crit}. A few years later, studies developed by Gray and Al-Refeai (1986) and Maher and Gray (1990) suggested that this critical stress is influenced by the aspect ratio (η), which is defined as the ratio between fibre length (l_f) and diameter (d_f). Still, the latter authors found that uniform, rounded sands present curved-linear behaviour whereas well-graded or angular sands tend to show bilinear failure envelopes. Figure 2.5 illustrates the bilinear effect of fibre inclusions on strength envelope of granular soils.

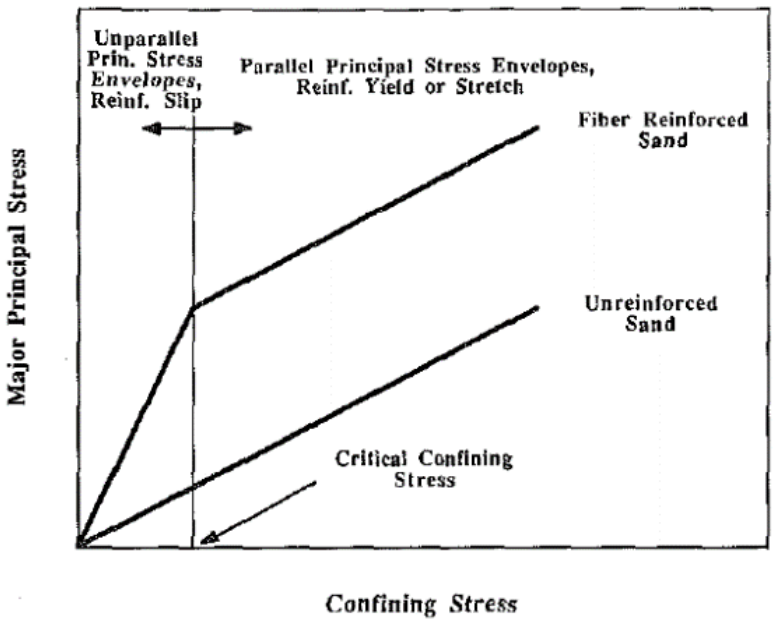

Figure 2.5 – Effect of fibre inclusions on failure envelope of sands
(MAHER; GRAY, 1990)

When the fibre-reinforced sand is under a confining stress lower than σ_{crit}, the failure of the composite is associated with a slip of the fibres, and plastic yielding of fibres do not take place. On the other hand, when the composite is subjected to a confining stress higher than σ_{crit}, the limit state is associated with plastic stretching or breakage of fibres (MICHALOWSKI; CERMAK, 2003).

2.2.4.2 Specimen density

Experimental results from triaxial tests carried out by Gray and Ohashi (1983) showed that the average increase in shear strength caused by fibre inclusions is approximately the same for dense and loose sands. However, this increase is more significant in the loose sands because initial unreinforced strengths are lower. In these (loose) sands, larger strains are required to mobilize the peak strength provided by the fibres.

Diambra (2010) suggested that higher relative densities increase the stress contribution of the fibres. That can be explained because fibres occupy some voids in the matrix, making the samples denser. As dense samples dilate more, they provide extra confinement to the grains and induce the development of higher tensile strains in the fibres. Nevertheless, the author warns that this topic may be object of further studies, as there has not been an agreement among researchers on a definition of void ratio and relative density of reinforced soils.

2.2.5 Influence of fibre characteristics

Several studies on the influence of fibre characteristics have been developed with many kinds of natural and synthetic inclusions: polypropylene, PVC, fibre glass, rubber, steel, oil palm, coconut, among others. This section presents some of the previous accumulated experience on the factors influencing the effectiveness of the reinforcements.

2.2.5.1 Elastic modulus of the fibres

It has been reported by Gray and Ohashi (1983) that higher elastic modulus of the fibres result in higher magnitudes of shear strength, although the strength is not proportional to the fibre modulus. Additionally, Gray and Al-Refeai (1986) observed that rougher fibres tended to be more effective in increasing strength than stiffer ones. This can be explained due to the increase in the friction between the inclusions and the soil grains. Still, Maher and Gray (1990) showed that fibres with higher modulus decrease the values of critical confining stress. That means that fibres with low modulus increase the pull-out resistance but contribute little to shear strength.

2.2.5.2 Fibre length and aspect ratio

The first remarkable studies on the influence of fibre length were performed by Gray and Ohashi (1983). The authors showed that increasing fibre length increases shear strength up to a limiting or asymptotic level beyond which any further increase had no effect. Gray and Al-Refeai (1986) observed that not only the length but also the aspect ratio had an influence on the composite behaviour, being roughly proportional to the shear resistance.

This conclusion was enhanced by Michalowski and Zhao (1996) who also noted that peak shear strength increased with increasing aspect ratio.

The influence of fibre length was assessed by several authors in the PPGEC at UFRGS, such as Ulbrich (1997), Feuerharmel (2000) and Casagrande (2001). A full analysis on the influence of fibre length, diameter and aspect ratio was provided by Festugato (2008).

2.2.5.3 Fibre content

It has been reported that increasing fibre content causes an almost linear increase in strength at high confining stresses or fibre ratios. For lower values of these two parameters, the shear resistance has an initial increase and then approaches an asymptotic upper limit (GRAY; AL-REFEAI, 1986; MAHER; GRAY, 1990). It is also known that an increase in the fibre content

with constant aspect ratio causes a significant increase in the peak shear strength and in the strain to failure, besides leading to a considerable decrease in stiffness (MICHALOWSKI; ZHAO, 1996).

Regarding the effect of fibre content in undrained triaxial tests, Ahmad et al. (2010) found that the pore water pressure generated during shear increased with increasing fibre content and fibre length, which leaded to an increase on shear strength. This behaviour had been reported in undrained tests in clays performed by Li and Zornberg (2003).

As cited before, Diambra (2010) and Ibraim et al. (2010) showed that an increase in fibre content leads to a reduction in liquefaction potential and that a higher content is required to prevent this phenomenon in extension. These authors also found that the higher the fibre content, the higher the hardening effect on the specimens.

2.2.5.4 Fibre orientation

It is known that fibres work in tension and that geosynthetics are responsible for the main field applications of fibre reinforcement. In these cases, the inclusions usually come in the form of strips or grids oriented at some specific direction. The selection of this orientation is usually made considering the direction where tensile strains will occur.

Gray and Ohashi (1983) carried out direct shear tests placing fibres at predetermined orientations. They observed that the inclusion of fibres oriented at an angle of 60° with the shear surface produced the greatest strength increase. The results were consistent with the reported by Jewel (1980) who showed that the principal tensile strain in dense sands is oriented at approximately 60° to the shear surface. The same author affirms it is expected that the reinforcement is oriented in the direction of principal tensile strains in order to mobilise as much tensile resistance as possible.

Michalowski and Zhao (1996) proposed that only fibres subjected to tension contributed to soil strength, which was latterly confirmed by Michalowski and Cermak (2002). For that reason, fibre contribution will be more significant for those oriented in the direction of maximum specimen extension. This orientation is frequently horizontal in engineering problems, as the vertical loads cause vertical compression and horizontal extension.

However, when it comes to discrete short fibre inclusions, most of the studies assume that the inclusions are randomly oriented throughout the soil mass. Such a distribution of orientation

provides a strength isotropy, preventing the development of localised failure planes, especially those parallel to the fibres (GRAY; AL-REFEAI, 1986; DIAMBRA et al., 2010).

Considering that fibre distribution is isotropic may lead to inaccuracies when predicting the composite strength. If the load is perpendicular to the plane where most of the fibres are oriented, for example, isotropic models will under-predict the increase in strength provided by inclusions. On the contrary, isotropic models may overestimate the fibre contribution when they are oriented at an angle close to the load direction (MICHALOWSKI; CERMAK, 2002).

Consequently, it is not only necessary to take into account the way fibre orientation distribution occurs inside the soil mass, but also to propose models which allow the users to apply such anisotropic distributions. Diambra et al. (2007) proposed a procedure to determine the fibre orientation distribution in samples prepared using a moist tamping technique, which is the most common procedure to preparing reinforced specimens. In this research, the authors found that 97% of fibres were oriented between -45° and 45° of the horizontal plane, which can be considered as a sub-horizontal orientation. This is far from isotropic, making necessary the models which allow anisotropic fibre distributions.

So, a fibre distribution function proposed by Michalowski and Cermak (2002) comes together with the necessity of outlining such anisotropic behaviour. One possible form for this function is based on the assumption that the distribution is axisymmetric with respect to the axis normal to the compacted layers, which for most engineering cases is the vertical axis. A spherical coordinates system is employed, as shown in Figure 2.6.

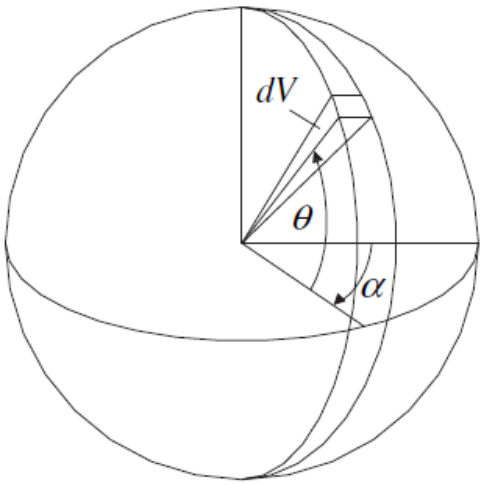

Figure 2.6 – Spherical coordinate system used to define the orientation distribution function (DIAMBRA et al., 2010)

A generalised fibre orientation function can now be defined as in equation (2.1) (MICHALOWSKI; CERMAK, 2002):

$$\rho\,(\theta) = \bar{\rho}\,(A' + C|cos^{n}\,\theta|) \tag{2.1}$$

where $\rho\ (\theta)$ represents the volumetric concentration of fibres per infinitesimal volume dV having an orientation of θ above the horizontal; $\bar{\rho}$ is the average volumetric concentration of the fibres and is given by the total volume of fibres (V_f) per total sample volume (V); and A', C and n are constants linked by the equation (2.2):

$$C = \frac{1 - A'}{\int_0^{\pi/2} cos^{n+1}(\theta)\,d\theta} \tag{2.2}$$

Other functions may be employed as long as the form depicted in equation (2.3) is fulfilled:

$$\bar{\rho} = \frac{1}{V}\int_V \rho(\theta)dV \tag{2.3}$$

2.3 FIBRE-SOIL INTERACTION

The fibre-soil interaction mechanism plays a fundamental role in the behaviour of reinforced sands. Not only are important the fibre characteristics, but also the confinement the inclusions are subjected to. The bond between fibres and sand grains affects the transfer of stresses between the two components.

Fibres contribution may cease in two different situations: due to fibre slip or tensile rupture. However, these failure mechanisms may occur simultaneously: even if a tensile breakage takes place, the ends of the fibres will slip. This phenomenon happens because the tensile strength of the inclusions are not mobilised throughout the entire fibre length (MICHALOWSKI; ZHAO,

1996). Figure 2.7(a) shows the fibre-matrix shear stress distribution whereas Figure 2.7(b) presents the axial stress distribution for a rigid-perfectly plastic fibre.

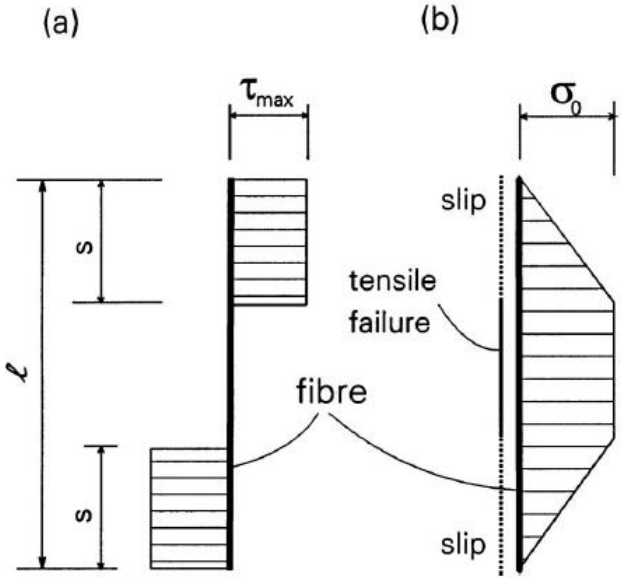

Figure 2.7 – Fibre-reinforced sand: (a) fibre-matrix shear stress; (b) fibre axial stress (MICHALOWSKI; ZHAO, 1996)

According to Michalowski and Zhao (1996), when a fibre rupture occurs, the slip mechanism develops at both fibre ends up to the distance s (equation (2.4)).

$$s = \frac{r}{2}\,\frac{\sigma_0}{\sigma_n\, tan(\sigma_w)} \tag{2.4}$$

where r is the fibre radius; σ_o is the yield stress of the fibre material; σ_n is the confining stress at the fibre surface; σ_w is the interface friction angle between fibre and matrix.

Pure slip will occur when if the fibre length l becomes less than 2s, or when the aspect ratio (η) fulfils the condition given by equation (2.5).

$$\eta < \frac{1}{2}\,\frac{\sigma_0}{\sigma_n\, tan(\sigma_w)} \tag{2.5}$$

However, such slide mechanism can be considered in a simpler way in constitutive models. The imperfection of the interfacial bond can be accounted for with the introduction of a dimensionless sliding factor f_b representing the relation of fibre strain ($\dot{\varepsilon}_f$) to the composite strain ($\dot{\varepsilon}$). A factor f_b = 1 represents a perfect fibre-matrix bond while f_b = 0 stands for full sliding (MACHADO et al., 2002).

Several expressions for the factor f_b can be adopted. Such factor will be analysed during the development of the constitutive model on Chapter 3 and a parametric analysis on this function will be presented on Chapter 4.

2.4 THE THEORY OF PLASTICITY AND THE CRITICAL STATE THEORY

The concepts of critical state soil mechanics were developed from the application of the theory of plasticity to soil mechanics. Therefore, a full understanding of critical state requires some knowledge of plasticity theory, whose basic concepts are presented as follows.

2.4.1 Plasticity theory

Even though this research is focused on fibre-reinforced soils, the essential ideas of plasticity theory can be better understood in metals. Figure 2.8 shows the stress-strain behaviour of a metal bar in a tension test. If the bar is loaded up to any point in OA, the stress path will follow the same path for either loading or unloading. That means that if we fully unload the bar, the stress state will take the reverse direction back to the origin. If the bar is then loaded up to B, the stress path is still reversible but not linear in the AB section. However, if it is loaded beyond point B, unload will not be reversible. This point B is called the yield point of the material. From this point on, if the bar is unloaded, a different path will be followed (CD, for example). In this case, part of the strain is not recovered (OD). This permanent strain is known as plastic strain. So, it can be said that up to point B the material is experiencing an elastic behaviour and from the point B on plastic strain occurs. It is worth highlighting that it is the reversibility rather than the linearity which determines the elasticity or plasticity of a material (BRITTO; GUNN, 1987).

If the metal bar is reloaded from D to C, it will experience elastic strains up to point C, beyond which plastic strains will occur. Point C is then the new yield point rather than point B. This

phenomenon of increasing the yield point of the material is called hardening (BRITTO; GUNN, 1987).

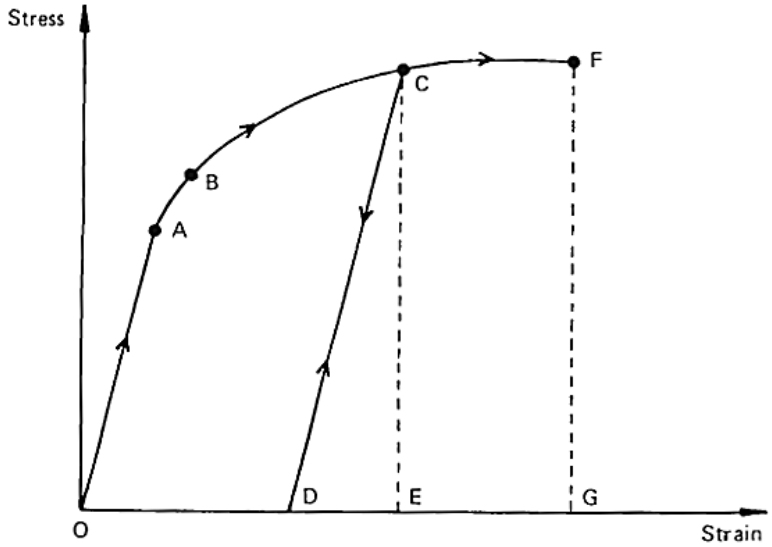

Figure 2.8 – Stress-strain curve typical of many metals (BRITTO; GUNN, 1987)

This discussion of plastic behaviour applies for uniaxial straining, i.e. with stresses and strains in only one direction. In most of practical problems, considering more than one dimension is necessary. For this reason, a yield function – or yield criterion – may apply rather than just a yield point. In three-dimensional problems, it is commonly named yield surface.

2.4.1.1 Yield functions

The yield functions are the mathematical expressions of yield criterions, in other words, an equation which defines the limit of elasticity and the beginning of plasticity. As mentioned above, yield functions are represented by a point in one-dimensional loading, by a curve in two dimensional problems and by a surface in three dimensional loading. When the stress state is within the yield surface, the material behaves elastically. Once the surface is reached, plastic deformation occurs (YU, 2006).

Mathematically, a general form of yield functions can be expressed as follows in equation (2.6):

$$f(\sigma_{ij}) = f(I_1, I_2, I_3) = 0 \tag{2.6}$$

where σ_{ij} is the stress tensor and I_1, I_2 and I_3 are the stress invariants. If the function has a value less than zero, the stress state is inside the yield surface. If the value reaches zero, plastic deformation will be produced.

2.4.1.2 Plastic potential and flow rules

Besides knowing whether plasticity has begun, it is also essential to determine how plastic strains occur after yielding. The answer to this question is given by the flow rule, which gives the ratios of plastic strain increments when the material is yielding (BRITTO; GUNN, 1987; YU, 2006). A general form of flow rule general form is given by equation (2.7).

$$\dot{\varepsilon}_{ij}^{p} = m \frac{\partial g}{\partial \sigma_{ij}} \tag{2.7}$$

where $\dot{\varepsilon}_{ij}^{p}$ is the plastic strain rate, m is a scalar and g is the plastic potential expressed in equation (2.8).

$$g = g\left(\sigma_{ij}\right) = g\left(I_1, I_2, I_3\right) = 0 \tag{2.8}$$

The strain increment vectors are always normal to the plastic potential, which may or may not be the same as the yield surface, depending on the material. When $f(\sigma_{ij}) = g(\sigma_{ij})$ then the flow rule (equation (2.7)) is called an associated flow rule, also known as normality rule. On the contrary, it is called non-associated flow rule (BRITTO; GUNN, 1987; YU, 2006).

2.4.1.3 The hardening laws

The idea of raising the yield point of some materials was presented above in paragraph 3.1. However, that concept is applied to one-dimensional cases. As well as for the yield function, the hardening laws need to be expanded for two and three dimensional stress states.

Hardening may occur when the yield surface changes in size or position through expansion or translation, respectively. The choice of either the former or the latter way the yield surface changes will determine the kind of hardening: isotropic or kinematic.

The rule of isotropic hardening assumes that the yield surface maintains its shape and centre but changes its size by expanding or contracting uniformly (Figure 2.9 (a)). On the other hand, kinematic hardening assumes that the yield surface does not change in size and shape but translates in the stress space (Figure 2.9 (b)).

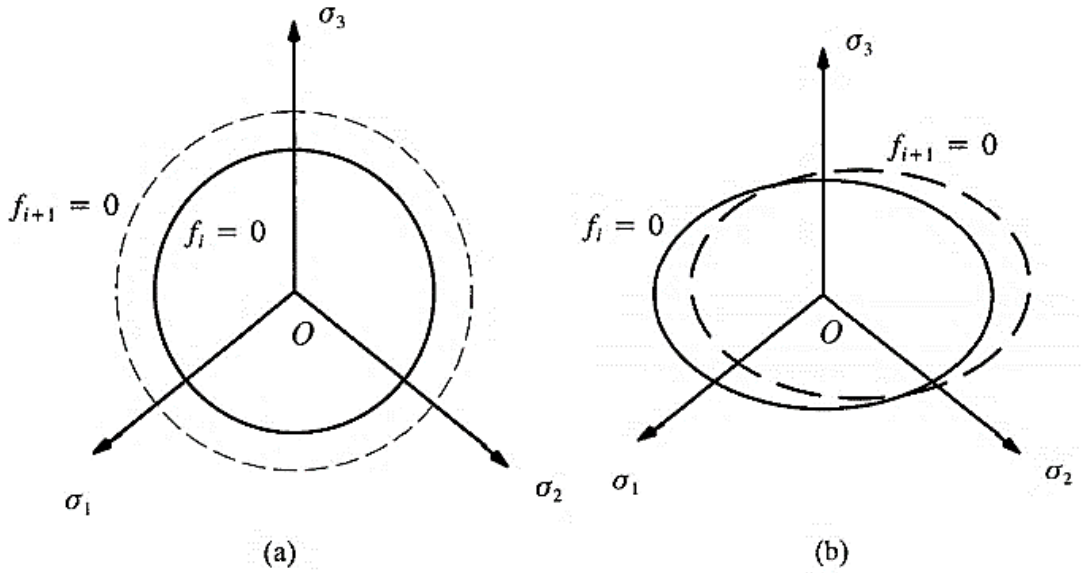

Figure 2.9 – (a) Isotropic hardening; (b) Kinematic hardening (adapted from YU, 2006)

2.4.2 The critical state theory

The critical state theory was firstly introduced by Schofield and Wroth (1968) who describe the concept of critical states as a well-defined state reached by soil when continuously distorted until they flow as a frictional fluid. This state, according to the authors, is determined by two equations ((2.9) and (2.10)).

$$q = Mp' \tag{2.9}$$

$$\Gamma = v + \lambda\, ln(p) \tag{2.10}$$

where q is the deviatoric shear stress; M is the slope of the critical state line in the q-p plane, also called stress ratio; p' is the effective mean stress; Γ is the intercept of the critical state line

on *v*-ln(*p'*) plane at *p'* = 1 kPa; v is the specific volume; and λ is the slope of the critical state line on the *v*-ln(*p'*) plane.

The critical state is graphically represented by two straight lines: one on the *v*-ln(*p'*) plane and another one on the *q*-*p'* plane (Figure 2.10).

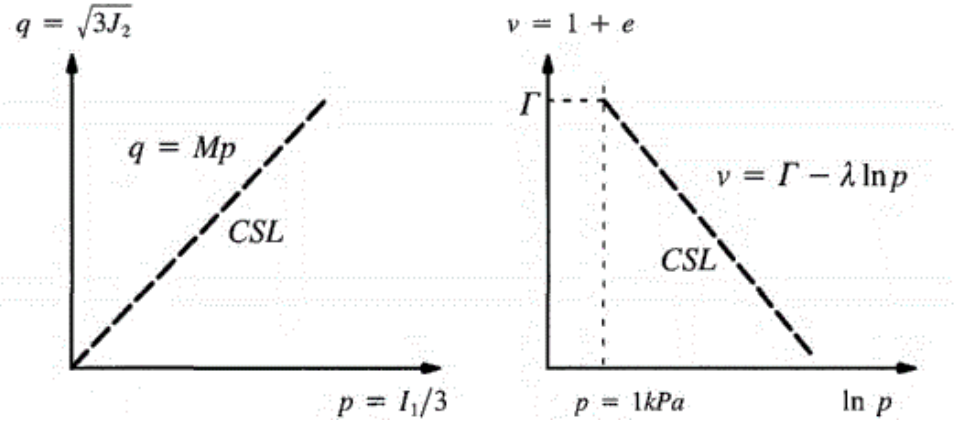

Figure 2.10 – The critical state line (CSL) on the *q*-*p'* and on the *v*-ln(*p'*) planes (YU, 2006)

The critical state can be thought of as a condition of perfect plasticity, where plastic shearing continues indefinitely with no changes in volume and effective stresses (MUIR WOOD, 1990), as follows on equation (2.11).

$$\frac{\partial p'}{\partial \varepsilon_q} = \frac{\partial q}{\partial \varepsilon_q} = \frac{\partial v}{\partial \varepsilon_q} = 0 \tag{2.11}$$

where ε_q is the shear strain.

The critical state is reached when the equation (2.12) is fulfilled, in other words, when the effective stress ratio (η) is the same as the stress ratio in the critical state.

$$\frac{q}{p} = \eta = M \tag{2.12}$$

2.4.3 The state parameter

The state parameter was proposed by Been and Jefferies (1985) and aimed to represent sand behaviour in a single parameter that would combine the influence of void ratio and stress level. The authors found through a testing programme that several sands with different silt contents behaved similarly if they had the same proximity to critical state.

So, the state parameter was defined as the difference between void ratio (or specific volume) and the void ratio (or specific volume) at the critical state at the same effective mean stress, as depicted in Figure 2.11. In this way, positive values of state parameter indicate a loose sample whilst negative values represent dense samples.

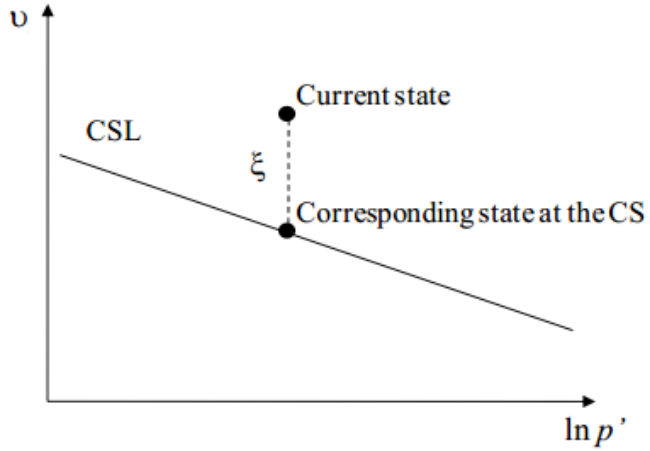

Figure 2.11 – Representation of the state parameter (adapted from DIAMBRA, 2010)

The state parameter has been found to be of great application in practical engineering. It has been demonstrated by Been and Jefferies (1985) that many sand properties, such as angles of friction and dilation, can be related to the state parameter. Even the formulation of some constitutive models such as Cam Clay (which is presented as follows) takes simpler forms if formulated in terms of the state parameter (YU, 2006).

2.4.4 The Cam Clay Model

Historically, the Cam Clay is of great importance because it was the first hardening plastic model adopted for soils). Even though this model was originally developed for soft clays, many of its patterns of response can be expressed by Cam Clay (MUIR WOOD, 1990; 2004).

So, it is of great interest to know the main features of this model. It is well-known that an elastic-plastic model requires four basic ingredients to be fully expressed: *elastic properties*, *yield surface*, *plastic potential* and *hardening rule*. These four aspects, as well as other relevant ones, are presented as follows.

First of all, getting to know the soil response to oedometric tests is necessary. Such test consists in loading a cylindrical sample vertically prohibiting any horizontal deformation, just as it usually occurs in the ground (DAVIS; SELVADURAI, 2002). Typical soil response to oedometric tests is shown in Figure 2.12.

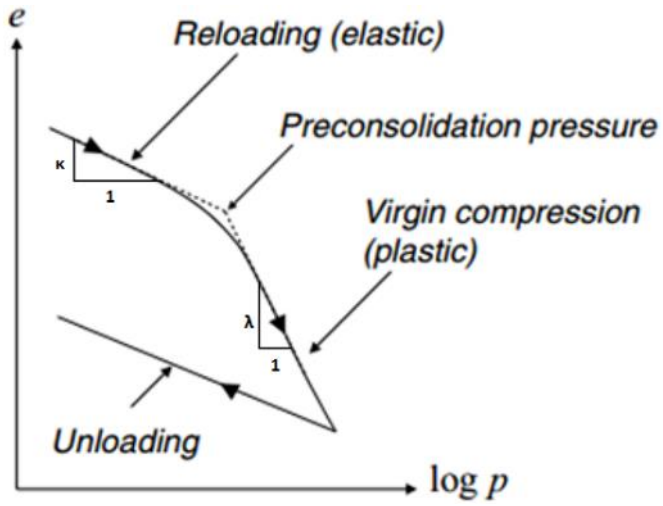

Figure 2.12 – Typical soil response to an oedometric test (adapted from DAVIS; SELVADURAI, 2002)

The graph depicted above presents two straight lines joined by a "knee", whose stress level is called preconsolidation pressure. It represents the greatest vertical effective stress the soil has been subjected to in its past history. The upper line represents the reloading from this past state, which continues until the preconsolidation pressure is reached. From this point on the soil experiences a new loading regime, the virgin compression. If the soil is then unloaded, the soil response will be approximately parallel to the first line (DAVIS, SELVADURAI, 2002).

In such a way, it is possible to obtain the parameters which are required to express the Cam Clay elastic properties – the first of the four ingredients to express the model – as presented in equation (2.13)

$$\dot{\varepsilon}_p^e = \kappa \frac{\dot{p}'}{v p'}, \tag{2.13}$$

where $\dot{\varepsilon}_p^e$ is the incremental volumetric elastic strain; κ is the elastic parameter of Cam Clay (see Figure 2.12); $\dot{p}'$ is the incremental effective mean stress and v is the specific volume.

This equation implies a linear relation between specific volume v and logarithm of effective mean stress p'. It is worth noting that this equation is closely related to the bulk modulus K, as shown in equation (2.14).

$$K = \dot{p}'/\dot{\varepsilon}_p^e \tag{2.14}$$

The second elastic constant can be obtained by assuming either a constant Poisson ratio (μ) or a constant value of shear modulus (G), according to equations (2.15) and (2.16), respectively (MUIR WOOD, 1990; YU, 2006).

$$G = \frac{3\,(1-2\mu)}{2\,(1+\mu)} K \tag{2.15}$$

$$\mu = \frac{3K - 2G}{2G + 6K} \tag{2.16}$$

As the elastic properties of the Cam Clay model were obtained, it is then possible to express its yield surface f. It is assumed for this model that the soil obeys an associated flow rule in such a way that the plastic potential g is coincident with the yield locus f (equation (2.17)).

$$f = g = \frac{q}{Mp} + ln\left(\frac{p}{p_0}\right) = 0 \tag{2.17}$$

where p_0 is the preconsolidation pressure, which serves as a hardening parameter.

The Cam Clay yield function is graphically expressed in Figure 2.13, in *q-p* space (a) and in principal stress space (b).

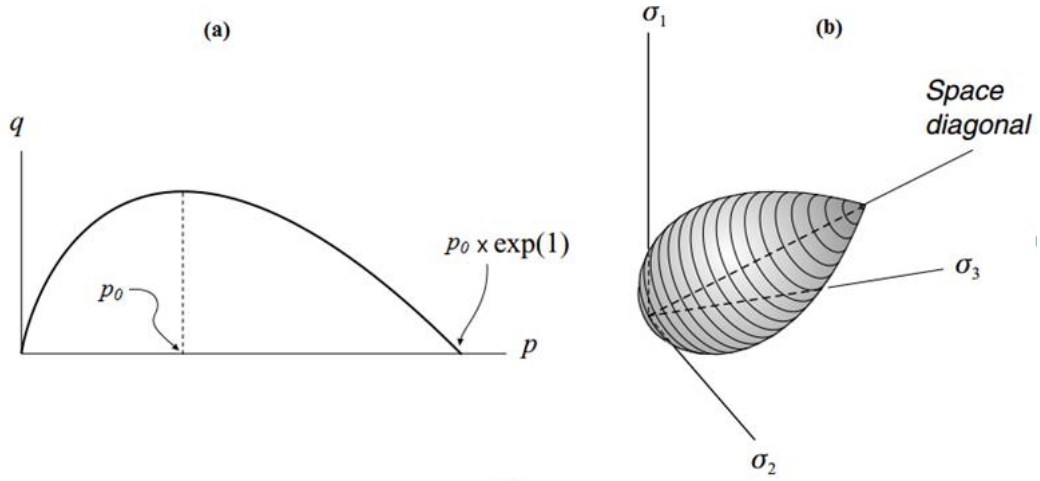

Figure 2.13 – Yield surface of Cam Clay model represented in (a) q-p plane and (b) principal stress plane (adapted from DAVIS; SELVADURAI, 2002)

Analysing Figure 2.13 (a) it is clear that the preconsolidation pressure p_0 controls the size of the yield surface. For this reason, in Cam Clay p_0 is assumed to change with the plastic volumetric strain according to equation (2.18), which also expresses the hardening rule of the model.

$$dp_0 = \frac{vp_0}{\lambda - \kappa} d\varepsilon_p^p \tag{2.18}$$

where p_0 is the preconsolidation pressure; v is the specific volume; λ and κ are material properties as presented above in Figure 2.12.

It is worth noting that variations in mean pressure do not produce plastic shear strains, as expressed in equation (2.19).

$$\frac{dp_0}{d\varepsilon_q^p} = 0 \tag{2.19}$$

Even though the Cam Clay model provided great advance in terms of geotechnical models, some aspects were still deficient (BRITTO; GUNN, 1987). These aspects were improved with the proposition of Modified Cam Clay (ROSCOE; BURLAND, 1968), which is presented as follows.

2.4.5 The Modified Cam Clay

Modified Cam Clay highlights two differences with respect to original Cam Clay: a particular point on the yield locus and the predicted value of the coefficient of earth pressure at rest, K_0. The problem is on the point where the yield locus crosses p' axis. Cam Clay associated flow rule would predict high shear strains for very low stress ratios, which is not verified experimentally. Furthermore, Cam Clay predicted a value of $K_0 = 1$ for normally consolidated soils whilst measured values range from 0.5 to 0.7 (BRITTO; GUNN, 1987).

These changes leaded to a different yield function (equation (2.20)) (YU, 2006) and consequently a different form of the yield surface (Figure 2.14)

$$f = g = \left(\frac{q}{pM}\right) - \frac{p}{p_0} + 1 = 0 \tag{2.20}$$

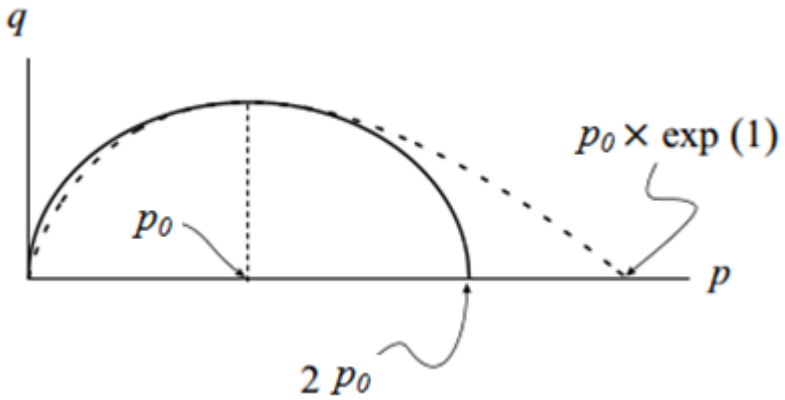

Figure 2.14 – Comparison between Cam Clay and Modified Cam Clay yield surface (adapted from DAVIS; SELVADURAI, 2002)

Despite these adjustments, many modifications have been proposed to the Cam Clay models over the years. This occurs due to some persisting limitations, as cited by Yu (2006):

a) Cam Clay models fail to predict a behaviour that is commonly observed in undrained tests on loose sands and some clays, which is a peak in the deviatoric stress before critical state is reached;

b) Cam Clay models are much less successful for modelling granular materials; those models, for example, are unable to predict softening and dilatancy of dense sands and the undrained behaviour of very loose sands.

More recently, Gajo and Muir Wood (1999) proposed a constitutive model that is able to assemble critical state concepts with a satisfactory prediction of the aforementioned aspects of granular soils: the Severn-Trent model for sands, which will be further explained in 2.5.2.

2.5 MODELLING OF GRANULAR SOILS

Most of the constitutive models were initially developed for metals. Nevertheless, many of them were employed to describe the behaviour of concrete and soil, even though their prediction did not accurately match soil response.

However, getting to know the basic concepts of constitutive modelling is fundamental to understand more complex and recent models. Hence, this section aims to present some constitutive models whose frameworks are important to fully understand the model proposed in this research.

2.5.1 Elastic-perfectly plastic Mohr Coulomb model

The elastic properties of a material are described by a pair of elastic constants. Initial constitutive models based on Hooke's law of elasticity to express general states of stress employed E (Young's modulus) and μ (Poisson ratio) as the elastic constants (MUIR WOOD, 2004). It is convenient though using K (bulk modulus) and G (shear modulus) as the elastic parameters as they control the volumetric and the distortional elastic response, respectively (ESCRIBANO, 2004). Thus, the latter constants can be easily associated to q and p', as expressed in equation (2.21).

$$\begin{bmatrix} \dot{p'} \\ \dot{q} \end{bmatrix} = \begin{bmatrix} K & 0 \\ 0 & 3G \end{bmatrix} \begin{bmatrix} \dot{\varepsilon_v} \\ \dot{\varepsilon_q} \end{bmatrix} \tag{2.21}$$

where p' is the effective mean stress, q is the deviatoric stress, K is the bulk modulus, G is the shear modulus, ε_v is the volumetric strain and ε_q is the distortional strain.

The plastic range of elastic-perfectly plastic models for soils is usually represented by Mohr-Coulomb's failure criterion. Mohr-Coulomb theory defines a linear failure envelope represented in the plane of normal (σ) and shear stresses (τ). The two parameters which describe the failure envelope are friction angle (ϕ') and cohesive intercept (c'), as presented in equation (2.22).

$$\tau = c' + \sigma \, tan(\phi') \tag{2.22}$$

Hence, for an elastic-perfectly plastic Mohr Coulomb model, soil behaviour is linear for stress states inside the yield surface and has a perfectly plastic failure when reaches the yield surface defined by equation (2.22). In terms of q and p', such surface for a purely frictional soil can be defined by a straight line whose slope is represented by M, as previously presented in equation (2.9). Consequently, the yield function is the one given by equation (2.23).

$$f(p', q) = q - Mp' \tag{2.23}$$

The parameter M is expressed in terms of friction angle for compression (equation (2.24)) and extension (equation (2.25)).

$$M_c = \frac{6\,sin(\phi')}{3 - sin(\phi')} \tag{2.24}$$

$$M_e = -\frac{6\,sin(\phi')}{3 + sin(\phi')} \tag{2.25}$$

When the soil yields, the relationship between incremental plastic strains is given by equation (2.26).

$$\frac{\dot{\varepsilon}_v^p}{\dot{\varepsilon}_q^p} = -M^* \tag{2.26}$$

As well as the relationship between M and φ', there is also a relationship between M^* and the dilatancy angle (ψ) (equations (2.27) and (2.28) for compression and extension, respectively). Dilatancy was first defined by Rowe (1962) as the ratio of plastic volumetric strain increments to plastic shear strain increments, exactly as expressed above.

$$M_c^* = \frac{3\,tan(\psi)}{3 + tan(\psi)} \tag{2.27}$$

$$M_e^* = \frac{3\,tan(\psi)}{tan(\psi) - 3} \tag{2.28}$$

Soils that contract when sheared have negative angles of dilation: $\psi < 0$ and $M^* < 0$; soils that expand have positive angles of dilation: $\psi > 0$ and $M^* > 0$ (MUIR WOOD, 2004), as depicted in Figure 2.15.

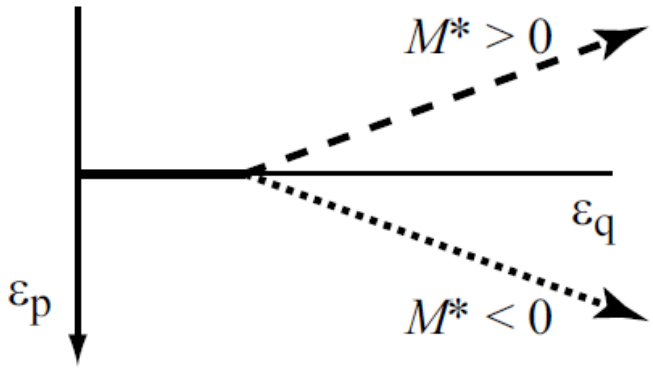

Figure 2.15 – Dependence of volumetric strain on M^* (adapted from MUIR WOOD, 2004)

Despite being broadly used in geotechnical engineering, Mohr-Coulomb model has several limitations when it comes to constitutive modelling. The original model assumed an associated flow rule, which means the plastic potential is the same as the yield function (equation 2.22). However, this assumption overestimates volumetric expansion of the soil and, for this reason, dilatancy angle (ψ) often replaces friction angle (φ'), originating a non-associated flow rule (ESCRIBANO, 2014).

Even with the aforementioned change in plastic potential, Mohr-Coulomb model still has other limitations. As it does not include the stress dependency on soil stiffness, the model does not capture the non-linear soil behaviour. Still, the straight line representation of failure is not suitable for some types of soil (ESCRIBANO, 2014).

2.5.2 The Severn-Trent sand model

The Severn-Trent sand model is the basis of the constitutive model which is the objective of this research. For this reason, it is presented here in a more detailed form than the other models.

The Severn-Trent sand model consists of a bounding-surface, kinematic-hardening constitutive model and was developed by Gajo and Muir Wood (1999). The model embraces aspects of different theories and approaches of geotechnical engineering. It combines Mohr-Coulomb failure, critical state concepts, such as the dependence of strength and stiffness on the state parameter, and a flow rule similar to that of Cam Clay. The model has a simple formulation and

requires two elastic and eight plastic parameters which can be obtained or calibrated from soil tests.

2.5.2.1 Surfaces and regions

First of all, it is important understand the surfaces that are part of the model (Figure 2.16). The strength surface is the bounding surface, and it always encloses the yield surface, which delimitates a purely elastic region. Both the strength and yield surfaces are represented as wedges in the *q-p'* plane. The size of the strength surface depends on the state parameter, which describes the distance of the actual void ratio from the one of critical state. In the *q-p'* plane, the critical state strength can be lower or higher than the bounding (strength) surface. For soils which are looser than the critical state, the current strength surface is lower than the critical state strength; for soils which are denser than the critical state, the current strength is higher than the critical state strength.

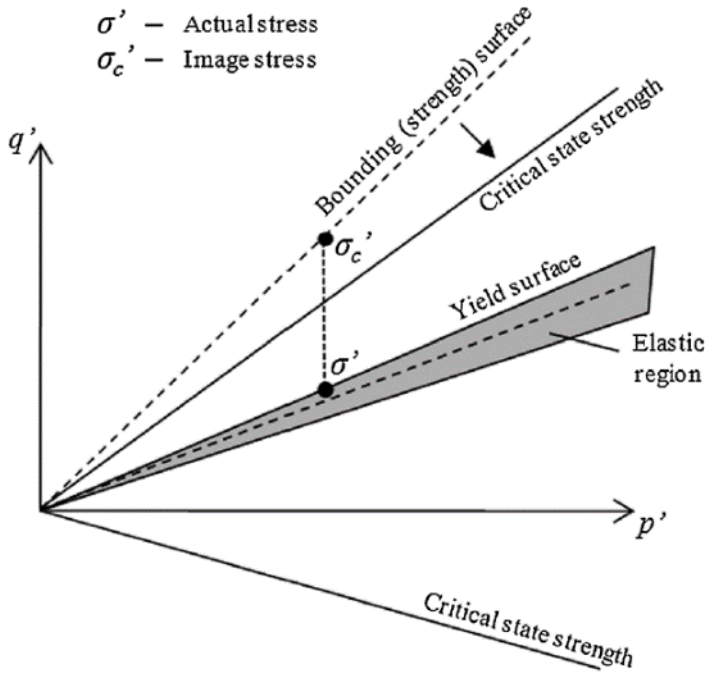

Figure 2.16 – Schematic view of the surfaces and the elastic region for the Severn-Trent sand model (DIAMBRA et al., 2013)

Mathematical development of the model is required in order to better understand the relationships between the surfaces. In the *q-p'* space, the slope of the critical state strength (M_{cs}) is given by equation 2.23 (when in compression) or 2.24 (when in extension) for the critical state friction angle (φ_{cv}). The bounding strength surface – whose slope is represented by M_b – is related to M_{cs} through a function r (ξ), as expressed in equation (2.29).

$$M_b = r(\xi) M_{cs} \tag{2.29}$$

The function $r\,(\xi)$ is given by equation (2.30).

$$r(\xi) = 1 - k_r \xi \tag{2.30}$$

where ξ is the state parameter and k_r is a constitutive parameter. Equation (2.29) ensures that as the soil approaches the critical state ($\xi = 0$), the parameter $r\,(\xi)$ approaches the unity and then the bounding surface tends to coincide to the critical state strength.

2.5.2.2 Stress space and surfaces

The model was originally developed in a normalised stress space in order to maintain constant the size of the strength surface. In such stress space, the deviatoric stress q is divided by $r\,(\xi)$. However, the model proposed in this research is developed in a not-normalised stress space, in order to provide a better understanding and an easier mathematical approach. For this reason all the equations presented herein refer to this space. Therefore the stress state $\boldsymbol{\sigma}$ is defined in equation (2.31).

$$\boldsymbol{\sigma} = \begin{bmatrix} q' \\ p' \end{bmatrix} \tag{2.31}$$

Once the normalised stress space is defined, the bounding surface $F(\boldsymbol{\sigma})$ can be expressed as follows in equation (2.32).

$$F(\boldsymbol{\sigma}) = q' - M_{cv}\, p' \tag{2.32}$$

The yield surface, which bounds the elastic states of the soil, can be defined by the direction of its axis, represented by a unit vector $\boldsymbol{\alpha}$ (equation (2.33)), and the opening m.

$$\boldsymbol{\alpha} = [\alpha_q, \alpha_p] \tag{2.33}$$

where $\alpha_q = \sin\beta$ and $\alpha_p = \cos\beta$ and β is the angle between the axis of the yield surface and the p axis (Figure 2.17).

The yield function can then be defined in terms of α_q and α_p as follows in equation (2.34).

$$f(\boldsymbol{\sigma}, \boldsymbol{\alpha}) = t - m_y s \tag{2.34}$$

where $\boldsymbol{\sigma} = [t, s]^T$ is defined by equations (2.35) and (2.36) and m_y represents either m_c or m_e, depending on whether triaxial compression or extension is taking place. The openings m_c and m_e are linked to the friction angle of the yield surface (φ'_y) by equations (2.37) and (2.38).

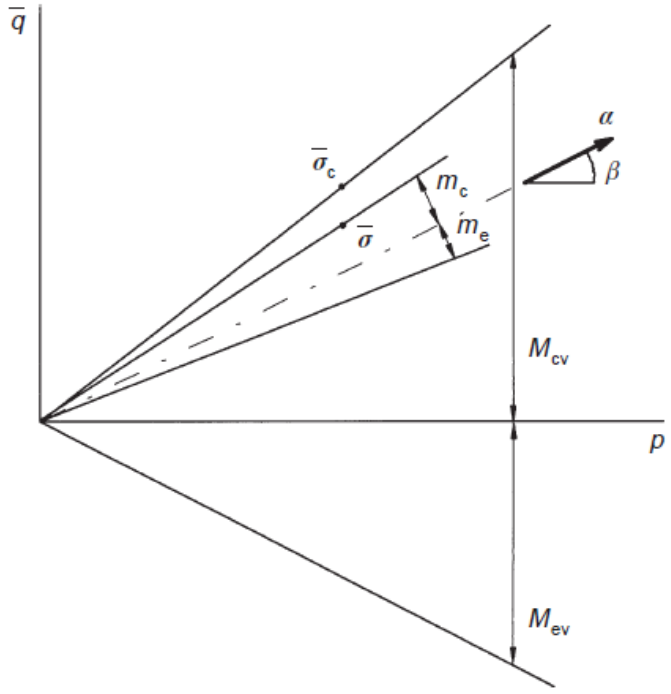

Figure 2.17 – Schematic view of the orientation vector **α** and the opening m for the yield surface (GAJO; MUIR WOOD, 1999)

$$t = q\alpha_p - p\alpha_q \tag{2.35}$$

$$s = q\alpha_q + p\alpha_p \tag{2.36}$$

$$m_c = \frac{6\ sin(\phi'_y)}{3 - sin(\phi'_y)} \tag{2.37}$$

$$m_e = -\frac{6\ sin(\phi'_y)}{3 + sin(\phi'_y)} \tag{2.38}$$

where φ_y' is related to the friction angle by equation (2.39).

$$sin\left(\phi'_y\right) = R\ sin(\phi') \tag{2.39}$$

where R is a constitutive parameter which represents the ratio of sizes of yield surface and strength surface.

The strength surface $F(\boldsymbol{\sigma})$ can then be defined by equation (2.40).

$$F(\boldsymbol{\sigma}) = \pm(q' - Mp') \tag{2.40}$$

where the function is positive (+) for compression and negative for extension (–) failure.

When the stress state reaches the yield surface, the direction of loading is defined by the vector $\boldsymbol{n}$ (equation (2.41)), which is normal to the yield surface (Figure 2.18).

$$\boldsymbol{n} = \begin{bmatrix} n_q \\ n_p \end{bmatrix} = \begin{bmatrix} \pm \dfrac{1}{r \times \sqrt{\dfrac{1}{r^2} + \left[\dfrac{k_r q'}{r^2}\left(\dfrac{\lambda}{p'} - \dfrac{\upsilon_m}{K}\right) - \dfrac{q'}{r\,p'}\right]^2}} \\ \pm \dfrac{\dfrac{k_r q'}{r^2}\left(\dfrac{\lambda}{p'} - \dfrac{\upsilon_m}{K}\right) - \dfrac{q'}{r\,p'}}{\sqrt{\dfrac{1}{r^2} + \left[\dfrac{k_r q'}{r^2}\left(\dfrac{\lambda}{p'} - \dfrac{\upsilon_m}{K}\right) - \dfrac{q'}{r\,p'}\right]^2}} \end{bmatrix} \tag{2.41}$$

where the signals (+) and (–) stand for compression and extension, respectively.

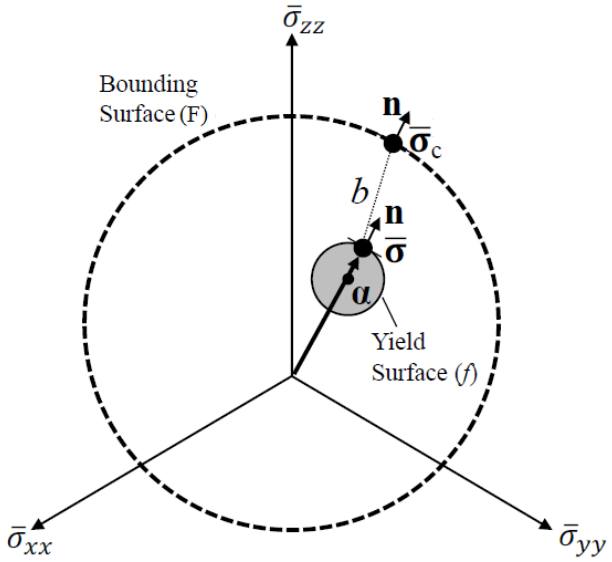

Figure 2.18 – Representation of the direction of vector **n** in deviatoric stress space (adapted from CORTI, 2016)

2.5.2.3 Elastic properties

Soil experiences elastic behaviour when the condition $f < 0$ is satisfied. In such case, the incremental stress-strain relationship is given by equation (2.21) previously presented. In a generalised form, this relationship can be expressed as in equation (2.42).

$$\dot{\boldsymbol{\sigma}} = \boldsymbol{D}^{\boldsymbol{e}}\,\dot{\boldsymbol{\varepsilon}} \tag{2.42}$$

where D^e is expressed in equation (2.43).

$$\boldsymbol{D^e} = \begin{bmatrix} 3G & 0 \\ 0 & K \end{bmatrix} \tag{2.43}$$

where *G* is the shear modulus and *K* is the bulk modulus.

The elastic shear modulus can be calculated according to the expression suggested by Hardin and Black (1966) in equation (2.44).

$$G = 323\, p_{atm}\, \frac{(3.97-\mu)^2}{\mu} \sqrt{\frac{p}{p_{atm}}} \tag{2.44}$$

where p_{atm} is a reference value (100 kPa) and μ is the Poisson ratio.

The bulk modulus can now be obtained assuming a constant value of the Poisson ratio (equation (2.45)).

$$K = \frac{2G(1+\mu)}{3(1-2\mu)} \tag{2.45}$$

2.5.2.4 Flow rule and stress-dilatancy relationship

As the stress state reaches the yield surface f, the soil behaves elasto-plastically and the flow rule is applied. The employed flow rule is similar to that of Cam Clay model and it is controlled by the stress-dilatancy relationship *d* which is governed by the state parameter ξ, as expressed in (2.46).

$$d = \frac{\dot{\varepsilon}_v^p}{\dot{\varepsilon}_q^p} = A\,[M_{cs}(1 + k_d\xi) - \eta] \tag{2.46}$$

where A and k_d are constitutive parameters and $\eta = q/p$. It is worth noticing that when $A = 1$ and $k_d = 0$ the flow rule is identical to the one of Cam Clay model.

Even though the flow rule is not explicitly defined, the direction of plastic flow can be defined through the unit vector $\boldsymbol{m}$, which is expressed in equation (2.47).

$$\boldsymbol{m} = \begin{bmatrix} m_p \\ m_q \end{bmatrix} = \begin{bmatrix} \dfrac{d}{\sqrt{1+d^2}} \\ \dfrac{1}{\sqrt{1+d^2}} \end{bmatrix} \tag{2.47}$$

2.5.2.5 Hardening rule

Before defining the hardening parameter H, it is essential to understand the stress states that govern it. The hardening modulus is assumed to be dependent on the distance between the current stress state $\boldsymbol{\sigma}$ and correspondent stress on the strength surface $\boldsymbol{\sigma_c}$ for the same effective mean pressure p'. This stress $\boldsymbol{\sigma_c}$ (which is called the *image stress*) is defined in equation (2.48) and the distance b is expressed in equation (2.49). Distance b can be visually checked on Figure 2.17 and Figure 2.18.

$$\boldsymbol{\sigma_c} = \begin{bmatrix} q_c \\ p \end{bmatrix} = \begin{bmatrix} M_{cs} p \\ p \end{bmatrix} \tag{2.48}$$

$$b = n_q (q_c - q) \tag{2.49}$$

The maximum value that b can be assume is defined by b_{max} in equation (2.50).

$$b_{max} = n_q [(M_c - M_e) - (m_c - m_e)]\, p \tag{2.50}$$

The hardening modulus can now be defined as equation (2.51).

$$H = H_f + H_b \tag{2.51}$$

where H_f (equation (2.52))is the hardening parameter given by Gajo and Wood (1999) in the normalised stress space and H_b (equation (2.53)) is an extra term added to convert the expression to the not-normalised space.

$$H_f = \frac{b^2}{B\ b_{max}} \tag{2.52}$$

$$H_b = m_p\ \frac{(-v_m k_r q')}{r^2} \frac{1}{\sqrt{\frac{1}{r^2} + \left[\frac{k_r q'}{r^2}\left(\frac{\lambda}{p'} - \frac{v_m}{K}\right) - \frac{q'}{r\ p'}\right]^2}} \tag{2.53}$$

The vector of plastic strain increments is then defined in equation (2.54).

$$\dot{\varepsilon}^p = \frac{1}{H}\boldsymbol{m}\ \boldsymbol{n^T}\dot{\boldsymbol{\sigma}} \tag{2.54}$$

2.5.2.6 Stress-strain relationships

The complete stress-strain relationship in the normalised stress space takes the form of equation (2.55).

$$\dot{\boldsymbol{\sigma}} = \left[\boldsymbol{D^e} - \frac{\boldsymbol{D^e m\ n^T D^e}}{H + \boldsymbol{n^T D^e m}}\right]\dot{\boldsymbol{\varepsilon}} \tag{2.55}$$

where the vector ***m*** represents the direction of the plastic flow in the regular stress space (equation (2.47)).

These equations provide the complete Severn-Trent sand model framework and they will be the basis for the further development of this research final model.

2.6 MODELLING OF FIBRE REINFORCED SANDS

The first models concerning fibre reinforced sands predicted solely the shear strength of such soils. As the models evolved, complete constitutive modelling frameworks were proposed. This section aims to present some remarkable contributions on modelling of fibre reinforced sands.

2.6.1 Models for predicting the shear strength

The first noteworthy model for predicting the shear strength of fibre reinforced soils was proposed by Gray and Ohashi (1983) and Gray and Al-Refeai (1986). The model was based on force-equilibrium analysis and it considered the stress contribution of individual fibres oriented either perpendicularly or inclined to the shear surface in sands (Figure 2.19). The model assumed that shearing stress developed in the sand mobilized tensile resistance in the fibers via friction at the fiber-sand interface. This model was further expanded by Maher and Gray (1990) in order to account for randomly oriented fibres.

An important contribution on predicting a failure criterion for fibre-reinforced soils was given by Michalowski and Zhao (1996). The authors employed an energy-based homogenization approach to arrive at a macroscopic failure stress (peak strength) of the fibrous granular composite. This model considered that the fibres could deform at the same rate as the matrix or slip in it. It also assumed that the fibres were distributed isotropically in the space with a random distribution of orientation. Such features were accounted for in a model for the first time, as well as other typical aspects of constitutive models such as a flow rule and a Mohr-Coulomb failure criterion for the matrix. An anisotropic distribution of fibre orientation was accounted for by Michalowski and Cermak (2002) with the proposition of the well-known function previously presented in equation 2.1. In this model, specimens with initially isotropic distribution were found to exhibit a kinematic hardening effect. Such behaviour was caused by the evolution of fibre orientation in the deformation process. Yet again, the model was based on energy dissipation concepts. Work dissipation was assumed to occur during sliding of the

fibres in the sand matrix or during plastic deformation of the inclusions after the elements reached the yield stress. The model predictions showed to be satisfactory.

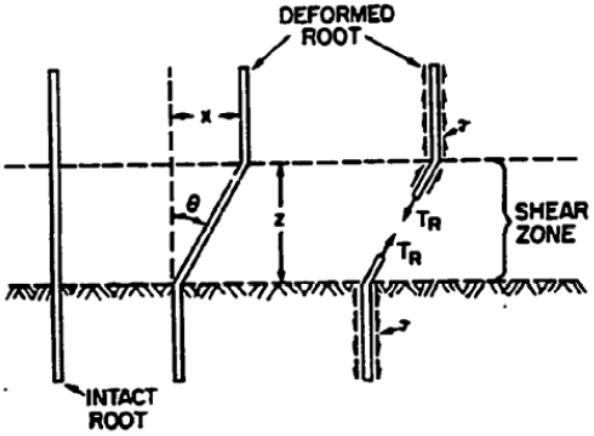

Figure 2.19 – Basic model for predicting the stresses mobilized in the fibres (GRAY; OHASHI, 1983)

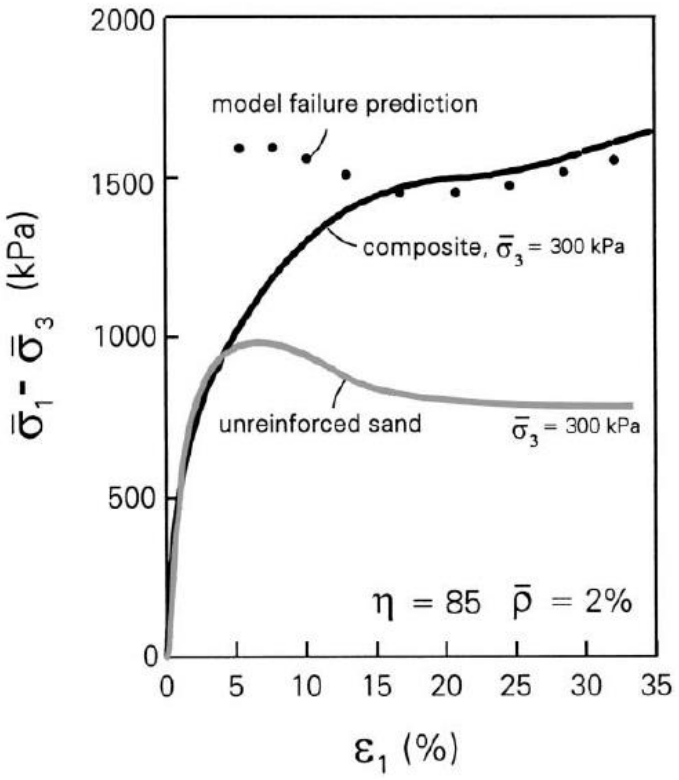

Figure 2.20 – Experimental results and model predictions for the model proposed by Michalowski and Cermak (2002)

2.6.2 Constitutive models for fibre-reinforced soils

Few authors have proposed a general constitutive law for fibre-reinforced soils. A non-linear stress-strain relationship of soil reinforced with flexible geofibres was proposed by Ding and

Hargrove (2006) for static loading conditions. Such model was based on the homogenization technique to find the volume average stress and strain tensors. As a result, it was possible to predict shear stress-axial strain response of soil and compare it to experimental data. The influence of distribution, content and geometrical features of geofibres was evaluated by employing an elastic energy method. Modelling under cyclic loading conditions was carried out by Li and Ding (2002) through cyclic shear tests using conventional triaxial apparatus. The influence of fibre content, confining pressure and loading repetition on shear modulus was evaluated. The authors proposed a hyperbolic function to describe the non-linear stress-strain curve under cyclic loading. The key factor of this model is the expression of elastic modulus as a function of shear modulus and two other parameters which are related to initial tangential modulus and ultimate cyclic loading stress. However, this model only captured soil response at small strain level.

Several models employed the superposition of sand and fibre thread effects in terms of their volumetric fractions (VILLARD; JOUVE, 1989; VILLARD et al., 1990; DI PRISCO; NOVA, 1993; SIVAKUMAR BABU et al., 2008). A complete constitutive model was also proposed by Villard and Jouve (1989) for assessing the behaviour of granular soils reinforced by continuous threads. The authors assumed the composite as a continuum material, consisting of a superposition of the granular material and the network of continuous threads, each of them being modelled separately. The threads were modelled as an elastic multidirectional network. The sand model took into account the phenomena of dilatancy and hardening and it was able to describe its behaviour under loading, unloading and reloading conditions. The model required just five parameters. The elastic behaviour of the sand matrix was described by a non-linear (power) law whereas the plastic response used a yield function and a non-associate potential function. The model was also able to predict plastic strains due to isotropic compression. Besides simulating soil response under axisymmetric problems, allowing a comparison to triaxial test results, the authors also adapted the model to plane strain problems and applied it to the calculation of retaining walls and banks. A similar model developed by Villard et al. (1990) recognises the importance of thread orientation on the effectiveness of soil reinforcement. Di Prisco and Nova (1993) proposed a model that assumes soil-threads strain compatibility and stresses summation. Both model phases were modelled with a linear elastic-perfectly plastic approach. Despite recreating quite well the response for conventional triaxial compression, the model is unable to reproduce certain features such as softening, dilatancy at failure and influence of confining stress on the volumetric strains.

Sivakumar Babu et al. (2008) used an advanced finite element method software to reproduce results from conventional triaxial tests on sands reinforced with coir fibres. Elastic-perfectly plastic Mohr-Coulomb model was used to simulate the matrix behaviour. The fibres were modelled as cable elements of uniform cross-sectional area between two nodal points. The behaviour of the cables was described one-dimensionally by the elastic Young's modulus. Even though experimental results are in accurate agreement with the numerical results, volumetric response is not assessed in this model.

Recently, important contributions on both drained and undrained behaviour of sands reinforced with randomly oriented fibres have been given by Diambra and his co-workers (DIAMBRA et al., 2007; 2010; 2011; 2013; IBRAIM et al., 2010). This group of contributions will be the basis for the development of the constitutive model proposed in this research.

Fibre orientation in specimens prepared using moist tamping technique has been shown to be typically oriented within $\pm$ 45° of the horizontal plane (DIAMBRA et al., 2007). Due to this finding, accounting for any fibre orientation distribution was necessary in the next models. For such consideration, the authors employed the generalised function presented on equation 2.1. The rule of mixtures was applied in the models. This rule accounts for sand matrix and fibre contribution according to their volumetric contribution. Each phase is governed by its own constitutive law. Hence, drained behaviour of fibre-reinforced sands under monotonic loading was satisfactorily reproduced by Diambra et al. (2010). Additional features were captured by Diambra et al. (2013) concerning the volume of voids. The authors suggest that part of the total volume of voids is “attached” to the sand matrix and other part is attached to the fibres. In such way, part of the voids is “stolen” by the fibres and a densification of the sand matrix is induced in the model. The undrained response of fibre reinforced loose sands was modelled by Ibraim et al. (2011) using the same axioms of the former models. This type of soil is very susceptible to the phenomenon of static liquefaction and the inclusion of tension resisting elements is frequently carried out as an attempt to avoid such sort of problems. The authors performed compression and extension triaxial tests under monotonic loading and they found that the inclusions decrease the susceptibility of static liquefaction by densifying the specimen and converting strain softening into a strain hardening response. The soil behaviour aspects from this research were modelled by Diambra et al. (2011), which was able to reproduce the experimental results very well.

2.6.3 Micromechanical approaches

Discrete Element Method (DEM) approaches was firstly introduced by Cundall (1971) for the analysis of blocky rock systems. A few years later, Cundall and Strack (1979) modelled particles individually to simulate the response of granular assemblies.

Recently, the some authors have developed models based on micromechanical approaches, using DEM. Ibraim et al. (2006) and Maeda and Ibraim (2008) employed two-dimensional DEM simulation to understand how fibres generate a bond within the soil and affect the kinematics of the granular matrix. Sand grains were modelled as rigid disks and their interaction was reproduced by contact elements, such as springs. Fibre elements were modelled by connecting small circular particles with a bond contact which had tension and shear strength without rotation constraints. Numerical results, enhanced by experimental data, suggested that fibres form a network with some resisted strength. The simulations also confirmed that the dilatancy is affected by the amount of inclusions and that the presence of fibres increases micro-confinement for the granular matrix.

Further research on DEM approaches to the response of fibre-reinforced granular soils was also carried out by Ferreira (2010), whose simulations successfully captured the influence of fibre content and fibre stiffness in the composite response. Additionally, Velloso et al. (2012) incorporated fibre elements into an existing DEM code (GeoDEM) through a linear elastic-perfectly plastic sliding model at particle contacts. The 2D simulations successfully reproduced the increase in shear strength of the reinforced soil in comparison with pure sand. However, the increase in ductility reported in the literature was not fully observed, indicating that the model for the fibres needs to be improved.

3 MODEL STRUCTURE

As cited in the literature review, most of the models concerning fibre-reinforced sands have focused on predicting the shear strength of such composites. Still, most of these model approaches have concentrated on soils reinforced with continuous threads or geotextiles, and fewer models have proposed a general constitutive law for soils reinforced with randomly distributed fibres.

This chapter aims to propose and describe a complete constitutive model for sands reinforced with randomly distributed fibres under cyclic loading, for both drained and undrained conditions. Special focus will be given to the undrained response of the composite, due to the susceptibility of liquefaction under such drainage conditions. It is worth noticing that the proposed model aims to reproduce the response of cyclic triaxial tests. Dynamic effects are not accounted for in the simulations, i.e. the simulations aim to reproduce triaxial tests subjected to compression-extension loads at a constant standard strain rate. For this reason, more complex approaches should be developed in order to simulate certain dynamic situations such as earthquakes.

In the previous chapter, several factors were shown to affect the response of reinforced materials. Previous studies have shown that not only the characteristics of matrix and fibres play a fundamental role in the composite response, but also the sample preparation technique and test conditions affect the material behaviour (DIAMBRA, 2010). The model proposed aims to capture the main aspects governing the behaviour of reinforced sands and to reproduce some experimental results.

3.1 RULE OF MIXTURES

Several approaches have been proposed to account for the contribution of the different phases of composite materials. Particularly on fibre-reinforced soils, these approaches can be divided into two big groups: micro-mechanical models, which usually discretize the inclusions and soil elements, and macro-mechanical models, which express the composite as a single material. The latter approach usually employs a homogenisation technique.

As previously mentioned in the literature review, Michalowski and Zhao (1996) and Michalowski and Cermak (2002) proposed a homogenisation technique based on energy

concepts. The strength of the composite was determined by the superposition of the work dissipation rate of its constituents. However, the simplest homogenisation technique is the rule of mixtures (or mixing theory).

Hence, the rule of mixture has been chosen here for its simple formulation and also for the previous experience of some authors, who showed that this technique is accurate enough for predicting soil response.

The rule of mixture usually follows three basic axioms (DIAMBRA et al., 2010):

a) each component of the composite satisfies its own constitutive law;

b) each component is homogeneously distributed throughout the composite;

c) the individual contribution of each phase to the overall composite behaviour is scaled according to their volumetric fractions.

In an unreinforced specimen, the volume of a specimen is simply made up of solids (V_s) and voids (V_v), which may or may not be filled with water. On the other hand, the total volume of a composite is made up of sand, fibres and voids. Sand and fibres constitute the solid phase whereas the volume of voids is separated into two parts: some voids are attached to the sand (V_{vs}) particles and others are attached to the fibres (V_{vf}). The phase diagram displayed on Figure 3.1 can better explain such aspects.

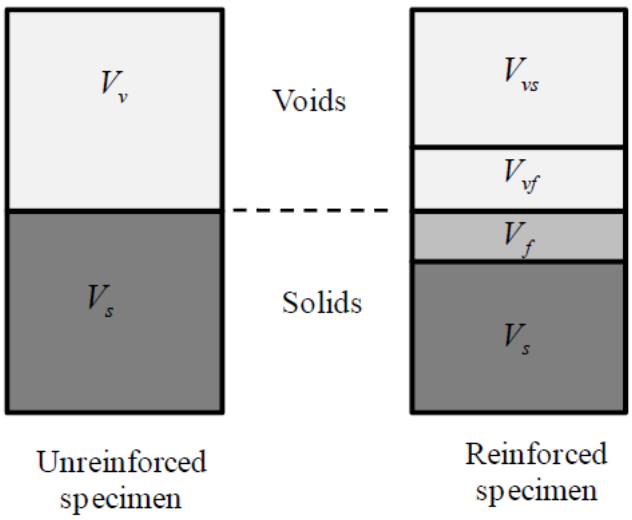

Figure 3.1 – Phase diagram for unreinforced and reinforced specimen (DIAMBRA, 2010)

The specific volumes of composite, sand and fibres are defined on equations (3.1), (3.2) and (3.3). They are linked by the relationship presented on equation (3.4).

$$\upsilon = \frac{V}{V_s + V_f} \tag{3.1}$$

$$\upsilon_m = \frac{V_{vs} + V_s}{V_s} \tag{3.2}$$

$$\upsilon_f = \frac{V_{vf} + V_f}{V_f} \tag{3.3}$$

$$\upsilon = \left(\upsilon_m + \upsilon_f \frac{G_s w_f}{G_f}\right) \frac{G_f}{G_f + G_s w_f} \tag{3.4}$$

where υ is the specific volume of the composite; V is the total volume of the composite; V_s is the total volume of solids; V_f is the total volume of fibres; υ_m is the specific volume of the matrix; V_{vs} is the volume of voids attached to the sand; V_s is the volume of sand grains; υ_f is the specific volume of fibres; V_{vf} is the volume of voids attached to the fibres; G_s is the specific gravity of soil; G_f is the specific gravity of the fibres and w_f is the fibre content in terms of volume.

As stated by in the third axiom of the rule of mixtures, the contribution of sand and fibres is accounted for according to their volumetric fractions. This scaled contribution applies to the incremental stresses and strains of the composite. The relationship between incremental composite strains and its constituents is defined by equation (3.5).

$$\dot{\boldsymbol{\varepsilon}} = \dot{\boldsymbol{\varepsilon}}_{\boldsymbol{m}}\mu_m + \dot{\boldsymbol{\varepsilon}}_{\boldsymbol{f}}\mu_f = \begin{bmatrix}\dot{\varepsilon}_{mv}\\ \dot{\varepsilon}_{mq}\end{bmatrix}\mu_m + \begin{bmatrix}\dot{\varepsilon}_{fv}\\ \dot{\varepsilon}_{fq}\end{bmatrix}\mu_f \tag{3.5}$$

where μ_m and μ_f are the volumetric contents of sand matrix and fibres and its voids, given by equations (3.6) and (3.7).

$$\mu_m = \frac{V_s + V_{vs}}{V} \tag{3.6}$$

$$\mu_f = \frac{V_f + V_{vf}}{V} \tag{3.7}$$

where V is the total volume of the composite. Likewise, the stress state of the composite is given by the superposition of the stresses of its constituents (equation (3.8)).

$$\boldsymbol{\sigma}^* = \mu_m\boldsymbol{\sigma}' + \mu_f\boldsymbol{\sigma}_f \tag{3.8}$$

In the incremental form, it is represented as in equation (3.9).

$$\dot{\boldsymbol{\sigma}}^* = \mu_m\dot{\boldsymbol{\sigma}}' + \dot{\mu}_m\boldsymbol{\sigma}' + \mu_f\dot{\boldsymbol{\sigma}}_f + \dot{\mu}_f\boldsymbol{\sigma}_f \tag{3.9}$$

3.2 FIBRE CONTRIBUTION

In this section, an expression for the overall stress contribution will be proposed, taking into account the distribution of fibre orientation. Initially, the stress-strain relationship of a single

fibre will be defined. Next, the overall stress contribution will be derived by the summation of all the fibres in all the angular domains.

3.2.1 Stress-strain relationship for a single fibre

As cited in the literature review, Michalowski and Cermak (2002) proposed a function for the distribution of fibre orientation (equations (2.1) and (2.2)), for each of *n* angular domains. Once the angular domains are defined, it is necessary to derive strains and stresses for each orientation. For now, it is assumed that strains of the composite and of the fibres are coincident. So, the incremental strains of the composite in the direction θ is defined in equation (3.10).

$$\dot{\varepsilon}_\theta = \dot{\varepsilon}_a \, sin^2(\theta) + \dot{\varepsilon}_r \, cos^2(\theta) \tag{3.10}$$

where $\dot{\varepsilon}_\theta$ is the incremental strain of the composite in the direction θ; $\dot{\varepsilon}_a$ and $\dot{\varepsilon}_r$ are the incremental axial and radial strain, respectively.

The function f_b is now introduced in order to account for the slide between fibres and sand grains. As cited in the literature review, several expressions have been proposed for this function and even constant values can be assumed (DIAMBRA; IBRAIM, 2014). In the present research, a constant sliding function f_b is calibrated. In such way, the stress developed in a fibre oriented at an angle θ is defined in equation (3.11). The influence of different values for the sliding function will be analysed hereafter.

$$\dot{\varepsilon}_{\theta f} = f_b \, \dot{\varepsilon}_\theta \tag{3.11}$$

where $\dot{\varepsilon}_{\theta f}$ is the incremental strain of a fibre in the direction θ.

The stress-strain relationship in a single elastic fibre can then be defined by equation (3.12). Stress is only mobilised if the fibre is in extension, in other words, when tensile strain occurs ($\dot{\varepsilon}_{\theta f} < 0$). Compressive resistance and bending stiffness are completely neglected. Moreover, the stress contribution of the fibres is not only dependent on whether the strain is positive or negative, but also it is limited by a pull-out stress (σ_f^L).

$$\dot{\sigma}_{\theta f} = E_f \, \dot{\varepsilon}_{\theta f} \leq \sigma_f^L \; for \; \dot{\varepsilon}_{\theta f} < 0 \tag{3.12}$$

$$\dot{\sigma}_{\theta f} = 0 \; for \; \dot{\varepsilon}_{\theta f} > 0$$

where $\dot{\sigma}_{\theta f}$ is the incremental stress in a fibre oriented at an angle θ; E_f is the elastic modulus of the fibres and σ_f^L is the pull-out stress.

The incremental stress in a single fibre oriented at an angle θ can then be decomposed in terms of axial (equation (3.13)) and radial (equation (3.14)) stress.

$$\dot{\sigma}_{fa} = \dot{\sigma}_{\theta f} \, sin^2(\theta) \tag{3.13}$$

$$\dot{\sigma}_{fr} = \dot{\sigma}_{\theta f} \frac{cos^{\,2}(\theta)}{2} \tag{3.14}$$

Once the stress contribution of a single fibre is defined, it is now necessary to account for the contribution of an agglomerate of fibres, which is presented as follows.

3.2.2 Fibre-soil bonding

As previously presented in equation (3.11), a sliding function f_b relates the strain in the composite to the strain in a fibre. This function can assume many forms, depending or not on the confining pressure. In this research, a constant value will be assumed for the sake of simplicity.

A limiting value for the stress transference from sand to fibre elements must be applied in order to account for the pull-out of the fibres within the soil matrix. Such phenomenon has been reported by Maher and Gray (1990) and Maher and Ho (1994). Thus the limit shear stress mobilised between fibre and sand may be calculated employing equilibrium of forces. The expression of pull-out stress is presented on equation (3.15).

$$\sigma_f^L = 2\,\frac{l_f}{d_f}(a_{sf} + \bar{p}\,tan\,\delta_{sf}) \tag{3.15}$$

where l_f is the length of the fibres; d_f is the diameter of the fibres; a_{sf} is the adhesive bond between sand and fibre surface, represented by a shear stress; δ_{sf} is the friction component on the interface and $\bar{p}$ is the average normal stress on the fibre. The value of $\bar{p}$ is taken approximately as the mean pressure in the composite (MICHALOWSKI; CERMAK, 2003).

When the threshold σ_f^L is reached, the incremental fibre contribution is equals zero and hence the stress state in the fibres remain unchanged.

3.2.3 Fibre orientation

In this research, fibre orientations are defined by the angles θ and α, which represent the orientation to the horizontal plane and to the vertical plane. Each angular domain is defined by an element with an area ($\Delta\theta$) x ($\Delta\alpha$). In terms of spherical coordinates, the fibre orientations are then divided into n x m angular domains (Figure 3.2).

The angle θ goes from $-\pi$ to $+\pi$ and the angle α goes from 0 to 2π. Hence, it follows that the angular amplitudes $\Delta\theta$ and $\Delta\alpha$ are defined by equation (3.16).

$$\Delta\theta = \pi/m;\ \Delta\alpha = 2\pi/n \tag{3.16}$$

Once the fibre orientations are defined, the fibre orientation distribution may be introduced. As presented in the literature review, Michalowski and Cermak (2002) proposed equation (2.1) to express the distribution of fibre orientation. In this research, such function is assumed to be the one presented in equation (3.17), which is a simplified form proposed by Diambra (2010) and Diambra et al. (2013).

$$\rho_\theta = a + b\,cos^n(\theta) \tag{3.17}$$

where $\rho\ (\theta)$ is the volumetric concentration of fibres per infinitesimal volume dV oriented at an angle θ; and a, b and n are constants linked by equation (3.18).

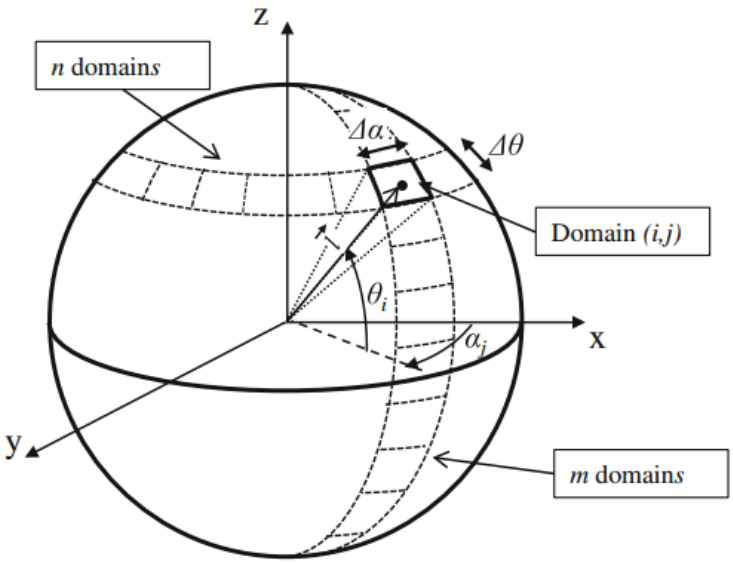

Figure 3.2 – Division of the fibre orientation distribution into angular domains (DIAMBRA et al., 2013)

$$b = \frac{1 - a}{\int_0^{\pi/2} cos^{n+1}(\theta)\, d\theta} \tag{3.18}$$

3.2.4 Overall fibre contribution

Once the contribution of a single fibre is defined, it is possible to calculate the overall fibre contribution, which takes into account the contribution of a single fibre and the volumetric concentration of fibres. This can be achieved by discretising the Gauss-Ostrogradsky theorem, which states that the flow of a vector field through a closed surface is equal to the volume integral of the region inside the surface (KATZ, 1979; RAM, 2009). Equation (3.19) expresses the overall fibre contribution over a whole spherical volume along a general direction k.

$$\bar{\sigma}_{fk}(\theta, \alpha) = \frac{1}{V} F_k(\theta, \alpha)\, l_k(\theta, \alpha) \tag{3.19}$$

where F_k is the equivalent tensile force mobilised on the spherical surface of the general direction k; l_k is the direction vector oriented at the direction k.

If the volume V is taken equal the unity, the force is given per unit volume of fibres, becoming a stress value. Therefore the axial and radial stresses of all the fibre oriented at the direction (θ, α) can be expressed (equations (3.20) and (3.21)).

$$\bar{\sigma}_{fa}(\theta,\alpha) = \frac{1}{2}\sigma_{f\theta}\, sin^2(\theta)\, \rho_\theta\, cos(\theta)\, \Delta\theta\, \Delta\alpha \tag{3.20}$$

$$\bar{\sigma}_{fr}(\theta,\alpha) = \frac{1}{4}\sigma_{f\theta}\, cos^3(\theta)\, \rho_\theta\, \Delta\theta\, \Delta\alpha \tag{3.21}$$

where $\bar{\sigma}_{fa}(\theta,\alpha)$ and $\bar{\sigma}_{fr}(\theta,\alpha)$ are the overall axial and radial stresses of the fibre phase at the direction (θ, α); $\sigma_{f\theta}$ is the stress of a single fibre oriented at an angle θ; $\Delta\theta$ and $\Delta\alpha$ are defined on Figure 3.2.

The contribution of all fibres oriented at all θ and α directions can be obtained through the summation of all the m x n angular domains. Assuming axisymmetric fibre orientation, frequently applied in modelling triaxial tests, the overall contributions are expressed as follows (equations (3.22) and (3.23)).

$$\bar{\sigma}_{fa} = \pi \sum_{i=1}^{m} \sigma_{f\theta}\, \rho_\theta\, sin^2(\theta)\, cos(\theta)\, \Delta\theta \tag{3.22}$$

$$\bar{\sigma}_{fr} = \frac{\pi}{2} \sum_{i=1}^{m} \sigma_{f\theta}\, cos^3(\theta)\, \rho_\theta\, \Delta\theta \tag{3.23}$$

where $\bar{\sigma}_{fa}$ and $\bar{\sigma}_{fr}$ are the overall axial and radial stresses of the fibre phase accounting for all the fibre orientations.

These equations can also be expressed using triaxial stress coordinates, according to equations (3.24) and (3.25).

$$p_f = \frac{\bar{\sigma}_{fa} + 2\bar{\sigma}_{fr}}{3} \tag{3.24}$$

$$q_f = \bar{\sigma}_{fa} - \bar{\sigma}_{fr} \tag{3.25}$$

3.3 CALCULATION PROCEDURE

In this section, the complete step-by-step calculation procedure of the model is described.

3.3.1 Definition of input parameters and initial test conditions

Before starting to run the model, defining the input parameters of soil, fibres and the initial test conditions is necessary. As aforementioned in the literature review (chapter 2), the Severn-Trent sand model proposed by Gajo and Muir Wood (1999) is employed herein. This model requires two parameters to define the elastic behaviour and eight parameters to simulate the plastic behaviour of the sand matrix. Table 3.1 presents a list of these parameters. A multiplier ζ in the adjustment factor *AF* is added to the input parameters. Further explanations on the adjustment factor are given in paragraph 3.3.8.

Next, the fibre parameters may be defined. The model requires seven input parameters as well as the parameters for the function of fibre distribution ρ (θ), which requires the parameters *a*, *b* and the number of angular divisions *n*. From this set of parameters, it is possible to calculate additional fibre characteristics. Table 3.2 presents the list of fibre parameters.

Initial test conditions and loading conditions may be defined as well. They are shown in Table 3.3.

Table 3.1 – List of input soil parameters

Parameter	Description
κ	Slope of the elastic line on the υ-ln p' plane (see Figure 2.12)
μ	Poisson's ratio
ϕ'	Friction angle
Γ	Intercept of critical state line on υ-ln p' plane (see Figure 2.10)
λ	Slope of critical state line on υ-ln p' plane (see Figure 2.10)
k_r	Link between changes in state parameter and current strength
B	Parameter controlling hyperbolic stiffness relationship
R	Ratio of sizes of yield surface and strength surface
A	Multiplier in flow rule
k_d	State parameter contribution in flow rule
ζ	Multiplier in adjustment factor

Table 3.2 – List of input fibre parameters

Parameter	Description
E_f	Elastic modulus of the fibres
l_f	Fibre length
d_f	Fibre diameter
f_b	Sliding function
υ_f	Specific volume of the fibres
G_f	Specific gravity of the fibres
$\rho\ (\theta)$	Fibre orientation distribution

Table 3.3 – List of input test and loading conditions

Parameter	Description
p_0	Initial confining pressure
υ	Specific volume of the composite
q_{up}	Higher stress value of the cycle
q_{down}	Lower stress value of the cycle
N_{cyc}	Total number of cycles
w_f	Fibre content in terms of volume

Once the input parameters and initial test and load conditions are defined, some other important features can be calculated. From the friction angle, the slope of the critical state line for

compression (M_c) and extension (M_e) can be calculated. The initial shear modulus G_0 can be calculated employing equation (2.44). Then the bulk modulus can be obtained from equation (2.45), which calculates *K* from the Poisson's ratio and the shear modulus. The specific volume of the matrix can be calculated from equation (3.4).

The state parameter can then be calculated by equation (3.26).

$$\xi = v_m - \Gamma + \lambda \, ln(p_0) \tag{3.26}$$

The deviatoric stress q_c of the image stress (which was represented by $\boldsymbol{\sigma_c}$ in Figure 2.17) can be calculated through equation (3.27), for initial conditions.

$$q_c = M_{cs} \, p_0 \, r \tag{3.27}$$

where q_c is the image stress, *M* is the slope of the critical state line and *r* is the ratio of sizes of strength surface and critical state surface (equation (2.30)).

3.3.2 Definition of strain increments

Triaxial tests can be stress-driven or strain-driven. Stress-driven tests have an important disadvantage: they are not able to capture post-peak behaviour of soils in case of a post-peak strength loss. As many reinforced sands present such behaviour, the model presented herein employs strain increments rather than stress increments. The size of the strain increment must be small enough to capture the behaviour of the composite in all the aspects analysed: stress-strain, v-ln p', q-p', ε_v- ε_a. Several values of composite strain increments were analysed. A value of 10^{-5} (0.001 %) was found to accurately reproduce the composite response. This value is similar to the one adopted by Diambra et al. (2013), who used a strain increment of 10^{-4}.

3.3.3 Vector of unknowns and vector of fibres

Once the strain increment is chosen, defining the vector of unknowns and the vector of fibres is required. Initially, these vectors will be composed of the initial states of soil, composite and

fibres. It is assumed that the composite, the matrix and the fibres are not subjected to any stress or strain (except the confining stress) and that the initial test conditions apply.

The vector of unknowns $\boldsymbol{L}$ must include all the incremental quantities that will be necessary to solve the equation system for each step of incremental strain. This vector is composed of seven unknowns related to the soil and seven unknowns related to the composite, which is shown in equation (3.28).

$$\boldsymbol{L} = [\dot{p}', \dot{q}, \dot{q}_c, \dot{v}_m, \dot{\varepsilon}_v, \dot{\varepsilon}_q, \dot{\xi}, \dot{p}, \dot{q}^*, \dot{v}, \dot{\varepsilon}_{mv}, \dot{\varepsilon}_{mq}, \dot{p}^*, \dot{u}]^T \tag{3.28}$$

where the first seven elements refer to the matrix and the last seven elements refer to the composite. The notation can be checked on paragraph 1.3.

The vector of fibres consist of the stresses in each orientation, depending on the number of orientations adopted. In this research, 9 angles were chosen to represent the fibre orientations, ranging from θ = 80° to θ = -80°. Initially, all the components of this vector are null, since the stress in the fibres have not been mobilised yet. As the increments of step occur, the stress is given by the stress-strain relationship presented on equation (3.12). Equation (3.29) shows the stress vector for fibres.

$$\boldsymbol{\sigma_f} = [\sigma_{f,80°}, \sigma_{f,60°}, \sigma_{f,40°}, \sigma_{f,20°}, \sigma_{f,0°}, \sigma_{f,-20°}, \sigma_{f,-40°}, \sigma_{f,-60°}, \sigma_{f,-80°}]^T \tag{3.29}$$

where the numbers in the subscript represent the angular domains adopted as fibre orientations.

3.3.4 Running the elastic function

Once the vector of unknowns and the vector of fibres are defined, it is possible to solve the system of fourteen differential equations, which will provide an $\boldsymbol{L}$ vector (equation (3.28)), for each strain increment. The set of equations is provided in Table 3.4. These equations are also presented in the matrix form in the Appendix. Most of them have been presented in the literature review, but they will again be shown herein in order to make it clearer.

Table 3.4 – Set of equations for the elastic function

Equation number	Description	Comments
1	$\dot{\varepsilon}_q = t$	Boundary condition
2	$\dot{q} - 3\dot{p} = 0$	Boundary condition
3	$\dot{u} = 0$ (drained) or $\dot{\varepsilon}_v = 0$ (undrained)	Boundary condition
4	$\dot{q}' = 3G\ \dot{\varepsilon}_{mq}$	Stress-strain relationship
5	$\dot{p}' = K\ \dot{\varepsilon}_{mv}$	Stress-strain relationship
6	$\dot{\varepsilon}_{mv} = -\dot{v}_m / v_m$	Specific volume for the matrix
7	$\dot{\xi} = \lambda \frac{\dot{p}'}{p'} - v_m \dot{\varepsilon}_{mv}$	State parameter relationship
8	$M\ r\ \dot{p}' - M\ k_r\ p' \dot{\xi} = \dot{q}_c$	Image stress
9	$\mu_m\ \dot{p}' + (\dot{\mu}_m\ p' - \dot{\mu}_m\ p_f)\dot{v}_m - \dot{p} + \dot{u} = -(1-\mu_m)\dot{p}_f$	Rule of mixtures – mean stress
10	$\mu_m\ \dot{q}' + (\dot{\mu}_m\ q' - \dot{\mu}_m\ q_f)\dot{v}_m - \dot{q} = -(1-\mu_m)\dot{q}_f$	Rule of mixtures – deviatoric stress
11	$\dot{\varepsilon}_v = \mu_m \dot{\varepsilon}_{mv}$	Rule of mixtures – volumetric strains
12	$\dot{\varepsilon}_q = \mu_m \dot{\varepsilon}_{mq}$	Rule of mixtures – distortional strains
13	$\dot{\varepsilon}_v = -\dot{v}/\dot{v}_m$	Specific volume for the composite
14	$\dot{u} = \dot{p} - \dot{p}^*$	Pore water pressure for the composite

A Runge-Kutta Fourth Order Method is employed to solve the system of differential equations. This method can be used not only to achieve approximate values, but also the whole solution for differential equations. For this reason, it is often used in computer programs and programming routines (RALSTON; RABINOWITZ, 1978). Given a strain increment *h* and a time increment *T*, the Runge-Kutta Fourth Order Method calculates the solution vector for the system of equations four times and adopts a weighted average to calculate the final increments. At the step *n*, the increment vector is given by equation (3.30).

$$L_{n+1} = L_n + \frac{h}{6}\,(K_1 + 2K_2 + 2K_3 + K_4) \tag{3.30}$$

where K_1, K_2, K_3 and K_4 are given by equations (3.31), (3.32), (3.33) and (3.34).

$$K_1 = f(T_n, L_n) \tag{3.31}$$

$$K_2 = f\left(T_n + \frac{h}{2}, L_n + \frac{h}{2}\,K_1\right) \tag{3.32}$$

$$K_3 = f\left(T_n + \frac{h}{2}, L_n + \frac{h}{2}\,K_2\right) \tag{3.33}$$

$$K_4 = f(T_n + h, L_n + h\,K_3) \tag{3.34}$$

In every step of strain increment, it is initially assumed that the stress state is in the elastic range. This assumption is made for the sake of simplicity in programming the Matlab code. However, after calculating it, it is necessary to check whether the stress state remains inside the elastic wedge after each incremental step. This verification is made through the yield function.

It is worth noting that the shear modulus *G* and the bulk modulus *K* must be recalculated after each step incremental step, as they depend on the mean pressure (*p'*) and on the specific volume of the matrix (υ_m), which go changing inside the $\boldsymbol{L}$ vector in every strain increment of the elastic function. The same applies to the volumetric content of sand matrix and its void ratios (μ_m), as it also depends on the specific volume υ_m.

3.3.5 Checking the yield function

The yield function checks whether the stress state is inside the elastic range or whether it has reached the yield surface. In this case, plastic strains occur. The yield function of the Severn-Trent sand model was presented on equation (2.34). However, in order to save numerical work, this yield function is not employed in this research. Instead, the yield surface is represented by the orientation of the stress state.

An imaginary vector $\overrightarrow{qp}$ is introduced in order to better understand how the yield surface is accounted for. If the simulation is following a stress path like the one in Figure 3.3, then $\widehat{qp}$ represents the angle of the vector passing on the origin and on the current stress state with the horizontal axis *p'*. The angles $\widehat{m}_c$ and $\widehat{m}_e$ represent the angles of the yield locus (on the compression and extension side, respectively) with the *p'*-axis. When loading, the model checks, after each small stress increment, if the angle $\widehat{qp}$ is bigger or smaller than the angle $\widehat{m}_c$. If $\widehat{qp}$ is smaller than $\widehat{m}_c$, then the stress state is inside the elastic range and the yield surface remains the same. On the contrary, if $\widehat{qp}$ is bigger than $\widehat{m}_c$, then the stress state crossed the yield surface. In practice, the stress state cannot lie outside the yield surface. For this reason, when the stress state crosses the yield surface, the whole surface rotates in order to make the stress state lie on the locus. This reproduces the kinematic hardening which is one of the features of Severn-Trent model. This verification is made after every strain increment, in such a way that the stress state will never be outside the yield surface.

Figure 3.3 shows a schematic view of the yield surface, the stress state and the aforementioned angles, whilst Figure 3.4 summarises the process described in the previous paragraph, for both compression and extension conditions.

Once the stress state reaches the yield surface, the soil starts developing plastic strains. Then, the elastic function is no longer adequate to describe the soil response. Hence the model must run the plastic function, which is described on 3.3.6.

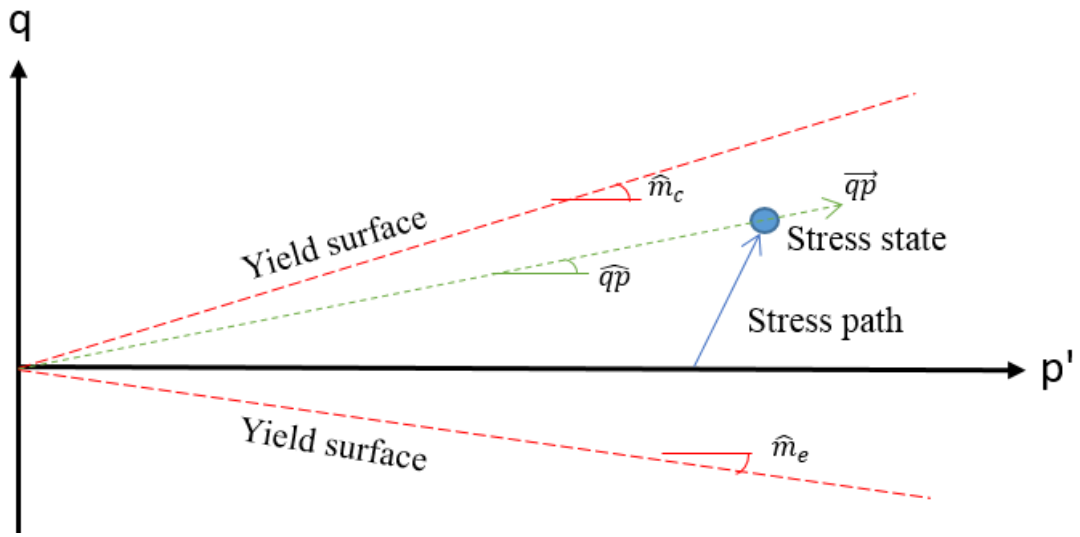

Figure 3.3 – Schematic view of the yield surfaces, stress state and orientation angles and vectors

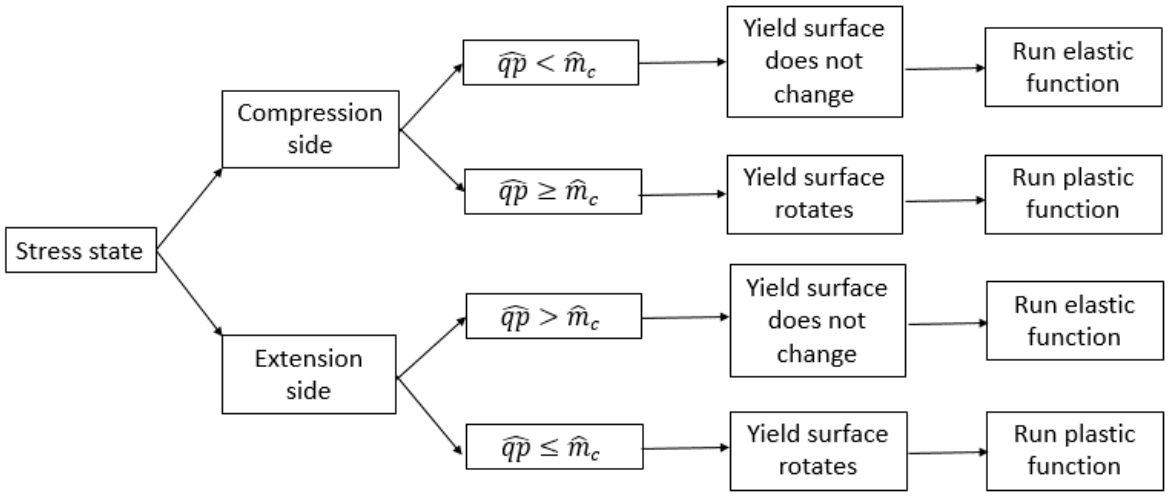

Figure 3.4 – Flowchart with the process followed by the model after checking the yield function

3.3.6 The plastic function

The Severn-Trent model is employed to describe the plastic behaviour of the soil. This model has been successfully employed to predict the matrix behaviour of fibre-reinforced soils (DIAMBRA, 2010; DIAMBRA et al., 2010; 2011; 2013; IBRAIM et al., 2010). The theoretical and mathematical framework of this model were provided in the literature review, paragraph 2.5.2. Nevertheless, this model was originally developed in the normalised stress state, where the deviatoric stress q is replaced by $\bar{q} = q/r$ (see equation (2.31)). The model proposed in this research is developed in the not-normalised stress space and, for this reason, some mathematical adjustments are made to make the equations compatible.

As mentioned in the preceding paragraph (3.3.5), the programming routine initially assumes that the stress state is inside the yield surface and then it calculates the yield criterion in order to check if it is really in the elastic range. In case the yield criterion tells the model to run the plastic function, the solution vector from the elastic function is suppressed and replaced by the one from the plastic function.

As well as in the elastic function, the system of equations for the plastic function is composed of fourteen equations. The vector of unknowns $\boldsymbol{L}$ is the same as presented on equation (3.28).

Before solving the system of equations, some other properties of the plastic response must be calculated for every step of strain increment, as they depend on unknowns from the vector $\boldsymbol{L}$ which change from step to step. These properties are listed below:

a) as well as in the elastic function, the shear (G) and bulk (K) modulus must be recalculated before every step, as it depends on p' and υ_m;

b) as well as in the elastic function, μ_m must be recalculated before every step, as it depends on υ_m;

c) the dilatancy relationship d (equation (2.46)) is recalculated before every step, as it depends on the state parameter ξ;

d) the ratio r is recalculated before every step (equation (2.30)) as it depends on the state parameter ξ;

e) the vector $\boldsymbol{n}$ (direction of loading) is recalculated (equation (2.41)), as it depends on q and p;

f) the vector $\boldsymbol{m}$ (direction of plastic flow) is recalculated (equation (2.47)), as it depends on the dilatancy d;

g) the distance b from the current stress state $\boldsymbol{\sigma}$ and the image locus $\boldsymbol{\sigma_c}$ and its maximum value b_{max} are recalculated (equations (2.49) and (2.50)) as they depend on n, q_c, q and p';

h) the hardening modulus H is recalculated, as it depends on b and b_{max}.

Once all these items above have been calculated, the system of fourteen differential equations (Table 3.5) can be solved.

Table 3.5 – Set of equations for the plastic function

Equation number	Description	Comments
1	$\dot{\varepsilon}_q = t$	Boundary condition
2	$\dot{q} - 3\dot{p} = 0$	Boundary condition
3	$\dot{u} = 0$ (drained) or $\dot{\varepsilon}_v = 0$ (undrained)	Boundary condition
4	$\dot{\varepsilon}_{mq} = \frac{m_q n_p}{H}\dot{p}' + \left(\frac{1}{3G} + \frac{m_q n_q}{H}\right)\dot{q}$	Stress-strain relationship
5	$\dot{\varepsilon}_{mv} = \frac{m_p n_p}{H}\dot{q} + \left(\frac{1}{K} + \frac{m_q n_q}{H}\right)\dot{p}'$	Stress-strain relationship
6	$\dot{\varepsilon}_{mv} = -\dot{v}_m / v_m$	Specific volume for the matrix
7	$\dot{\xi} = \lambda\frac{\dot{p}'}{p'} - v_m\dot{\varepsilon}_{mv}$	State parameter relationship
8	$M\ r\ \dot{p}' - M\ k_r\ p'\dot{\xi} = \dot{q}_c$	Image stress
9	$\mu_m\ \dot{p}' + (\dot{\mu}_m\ p' - \dot{\mu}_m\ p_f)\dot{v}_m - \dot{p} + \dot{u} = -(1-\mu_m)\dot{p}_f$	Rule of mixtures – mean stress
10	$\mu_m\ \dot{q}' + (\dot{\mu}_m\ q' - \dot{\mu}_m\ q_f)\dot{v}_m - \dot{q} = -(1-\mu_m)\dot{q}_f$	Rule of mixtures – deviatoric stress
11	$\dot{\varepsilon}_v = \mu_m\dot{\varepsilon}_{mv}$	Rule of mixtures – volumetric strains
12	$\dot{\varepsilon}_q = \mu_m\dot{\varepsilon}_{mq}$	Rule of mixtures – distortional strans
13	$\dot{\varepsilon}_v = -\dot{v}/\dot{v}_m$	Specific volume for the composite
14	$\dot{u} = \dot{p} - \dot{p}^*$	Pore water pressure for the composite

Solving the system of equations concludes one loop of strain increment, accounting for the fibre contribution through equations 9 and 10 of the elastic (Table 3.4) or plastic (Table 3.5) function, depending on the stress state.

The next round of calculation can then start, applying a new strain increment. The incremental stress in the fibres from the previous step is now accounted for using equations (3.22) and (3.23). This procedure is then repeated (from step 3.3.2 to 3.3.6) until the higher (q_{up}) or lower (q_{down}) stress value of the cycle is reached. This point is called the *reverse point* and it represents the change in the direction of the triaxial test: from loading to unloading or from unloading to loading.

3.3.7 The reverse points

The reverse points can be considered critical points in constitutive modelling, because they break the continuity of the plots and this can lead to numerical errors. Some care must be taken in order to avoid such errors.

First of all, the image point must be updated, as it must always be in the direction of loading. So, if the model is simulating triaxial loading, the image point $\boldsymbol{\sigma_c}$ should be situated on the bounding surface on the compression side (Figure 3.5 (a)). On the contrary, when triaxial extension is being simulated, the image point is placed on the extension side (Figure 3.5 (b)). This change in the image point affects the distance *b* from the current stress state to the image stress. Consequently, the hardening modulus *H* is affected as well.

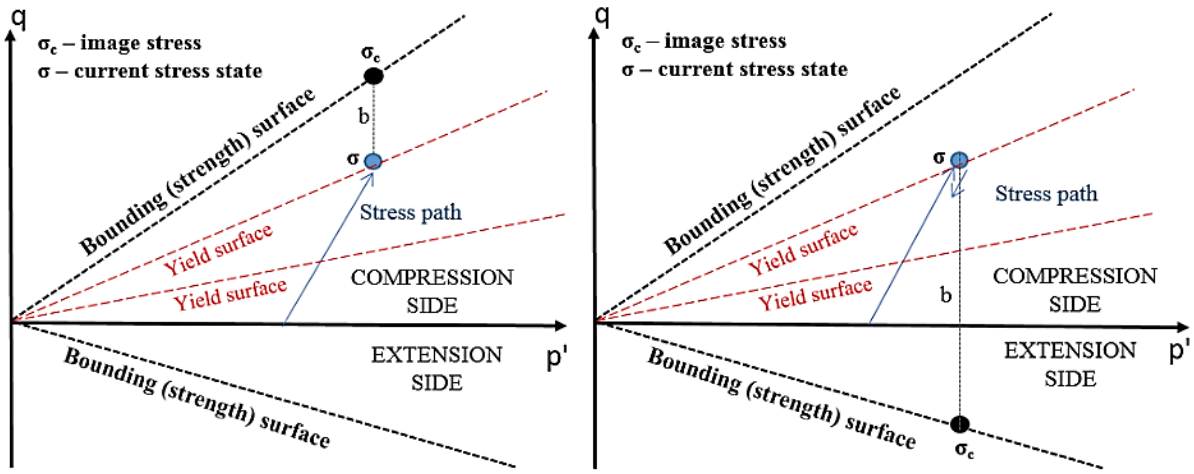

Figure 3.5 – Change in the image stress and distance *b* when reversing the stress path direction: (a) image point on the compression side; (b) image point on the extension side.

The second change to be made when reversing the loading direction is changing the signal of the strain increment. For compression, positive strain increments are imposed; for extension, these increments are negative. Still, the incremental strain must be small enough so that the simulation does not significantly exceed the stress in the reverse point. If one wishes to reverse the loading direction when q = 50 kPa but the strain increment is not sufficiently small, one single step can take the stress from 49 to 54 kPa, for example. Imposing small strain increments avoids such inaccuracies.

Another important aspect to be observed refers to the position of the stress state respect to the yield surface. When the test direction is reversed, the current stress state will be inside the yield surface even if it was experiencing plastic deformations before the reverse point. This happens because the stress state will have to course all the way inside the yield surface until it reaches the surface again in the opposite side.

Once these particular aspects have been observed, the calculation procedure follows the same steps previously mentioned (from 3.3.2 to 3.3.6) until it reaches the next reverse point. Every time the stress path reaches two reverse points, one cycle is completed. This process is repeated until the number of cycles N_{cyc} or failure or liquefaction is reached.

3.3.8 The adjustment factor (AF)

When carrying out model simulations, the author noticed that the effect of fibre inclusions was not well accounted for in the first cycles of load-unload. The reduction in axial strains and in pore pressure was only perceived after a certain number of cycles. To adjust this unconformity, an adjustment factor may be applied in the model. The first attempt was to try different expressions for the sliding function f_b. As mentioned in 3.2.1, previous research proposed stress-dependent or constant sliding functions for monotonic tests. For cyclic tests, several expressions were tried during the development of the proposed model in order to account for fibre contribution in the first cycles. Most of the investigated expressions attempted to relate f_b to the number of cycles N_{cyc} or to the current axial strain. However, none of these expressions was successful in reproducing the effect of fibre inclusion in the first cycles. For this reason, a different approach attempted to apply an adjustment factor upon certain model parameters. It is known from previous studies involving the Severn-Trent model that the parameters B and A depend mainly on the particle-particle interaction within the soil structure. When fibres are included within the sand, soil structure is modified and different interparticle forces appear. For this reason, it seems reasonable that parameters B and A are adjustmed by an empirical factor. Several expressions for the adjustment factor were investigated by the author during the parametric analysis and the model validation. The one that showed best agreement with the experimental trends is presented in equation (3.35).

$$AF = (1 + \zeta\, w_f) \tag{3.35}$$

where AF is the adjustment factor, ζ is a constitutive parameter and w_f is the fibre content. The parameters B and A, thus, need to be raised to this expression to account for the change in the grain contacts caused by the fibre inclusions. In such a way, in every single model simulation with fibre reinforced sands, B and A must be in the form of equations (3.36) and (3.37) as B^* and A^* respectively.

$$B^* = B^{AF} \tag{3.36}$$

$$A^* = A^{AF} \tag{3.37}$$

This sort of modification in the Severn-Trent has been previously proposed by Corti (2016). In that PhD thesis, the researcher included the parameter ς (damage rule parameter) to account for the damage in one of the surfaces of his model (the Memory Surface), avoiding the large strain accumulation caused by continuous cycling. In fact, in the calibration process for distinct sands, the values for Corti's parameter ς were as small as 0.00003. In other words, the inclusion of the damage parameter significantly alters the results of the model. On the contrary, in the model calibration for Osorio and Babolsar sand, it will be shown in Chapter 5 that the adjustment factor AF assumes values between 1.07 (w_f = 0.5% and ζ = 14) for Osorio sand and 1.10 (w_f = 1.0% and ζ = 10) for Babolsar sand. Therefore, the adjustment factor does not affect the model considerably, but it is still important to account for the effect of fibre inclusions in the grain contacts. Parametric analysis on ζ will be presented in Chapter 4.

3.4 KEY ASPECTS OF THE MODEL

Before carrying out the parametric analysis, certain key aspects of fibre-reinforced sands need to be assessed by model simulations. The objective of this paragraph is to verify whether the model is able to capture these key aspects of fibre contribution, even though the simulations

proposed herein are merely theoretical and do not have any relation with experimental data. The first verification is the compatibility between the stresses in fibres oriented at symmetric orientations respect to the horizontal. In other words, fibres oriented at an angle of +20° should be subjected to the same stress as those oriented at -20°, for example. The second verification concerns the agreement between radial strains and the strains in horizontal fibres, considering a full bond between fibres and grains ($f_b = 1$). The plots are presented as a function of the number of strain increments (steps) of the model simulation.

In this chapter, a general standard sand is initially simulated, with most of its properties based on Hostun sand (DIAMBRA et al., 2010; 2013; IBRAIM et al.; 2010). These parameters are summarised in Table 3.6. All the other simulations in this chapter start from this general standard sand.

Table 3.6 – List of input standard soil and fibre parameters

Soil parameter	Standard value	Fibre parameter	Standard value
κ	0.01	G_f	0.91
μ	0.1	w_f	0.5%
ϕ'	35°	υ_f	3.3
Γ	2.08	E_f *(MPa)*	1000
λ	0.031	f_b	1.0
k_r	1.5	l_f *(mm)*	35
B	0.00006	d_f *(mm)*	0.3
R	0.1	a_{sf} *(kPa)*	0
A	0.75	δ_{sf}	30°
k_d	1.5	ζ	10
G_s	2.65		

A set of initial test and loading conditions was chosen in such a way that the analysis would show the most important aspects of the model. A confining pressure p_o' of 100 kPa was chosen. Two initial specific volume of the composite (υ) were chosen: 1.95 (loose sand, I_D = 23%) and 1.7 (dense sand, I_D = 87%). The model was explored under drained and undrained conditions and the repeated loadings were simulated between 0 and 80 kPa and between -50 and 50 kPa.

3.4.1 Symmetry of fibre contribution

In axisymmetric problems, such as triaxial tests, it expected that the composite response is symmetrical in relation to the horizontal axis. This behaviour is also expected for the contribution of fibres, as their stresses and strains are directly related to that of the sand matrix.

The symmetry of fibre contribution for undrained conditions, loose sand and loading from -50 to 50 kPa is shown in Figure 3.6 (a). For loading from 0 to 80 kPa (Figure 3.6 (b)), the symmetry is also verified, for fibres oriented at +- 20° and +-40°. The same pattern is observed for dense sands (Figure 3.6 (a) and (b)).

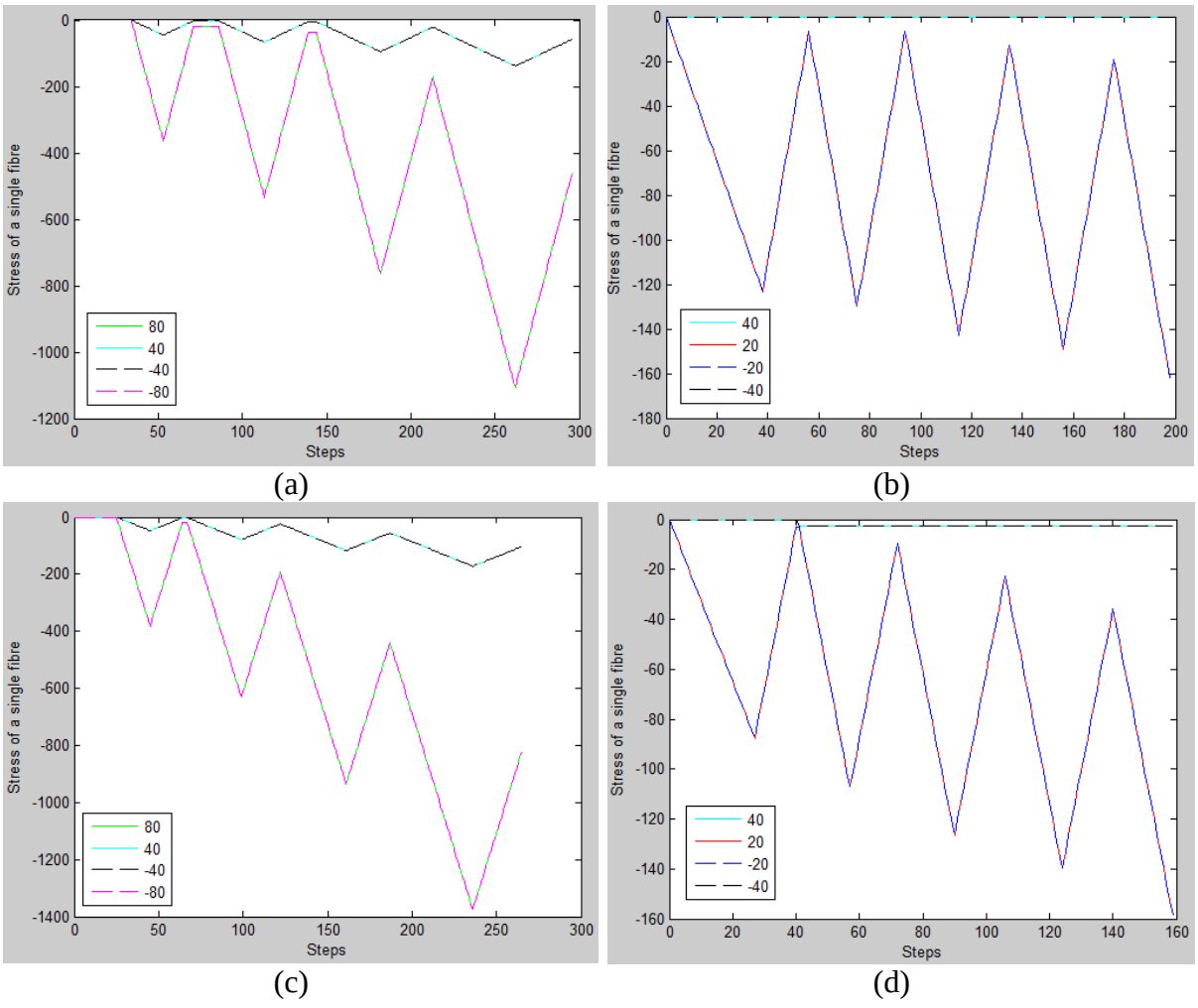

Figure 3.6 – Symmetry of fibre contribution under undrained conditions: (a) loose sand, *q* between -50 and 50 kPa; (b) loose sand, *q* between 0 and 80 kPa; (c) dense sand, *q* between – 50 and 50 kPa; (d) dense sand, *q* between 0 and 80 kPa.

3.4.2 Radial strains and horizontal fibres

Another verification that can be made in order to check the consistency of the model concerns the comparison of the radial strains in the matrix with the strain in the horizontal fibres, i.e. those oriented at 0° with the horizontal. A sliding function $f_b = 1$, which represents perfect sand-fibres bonding, is necessary in such verification. Otherwise, sliding between fibres and sand would occur and the stresses would always be different. Figure 3.7 portrays these results.

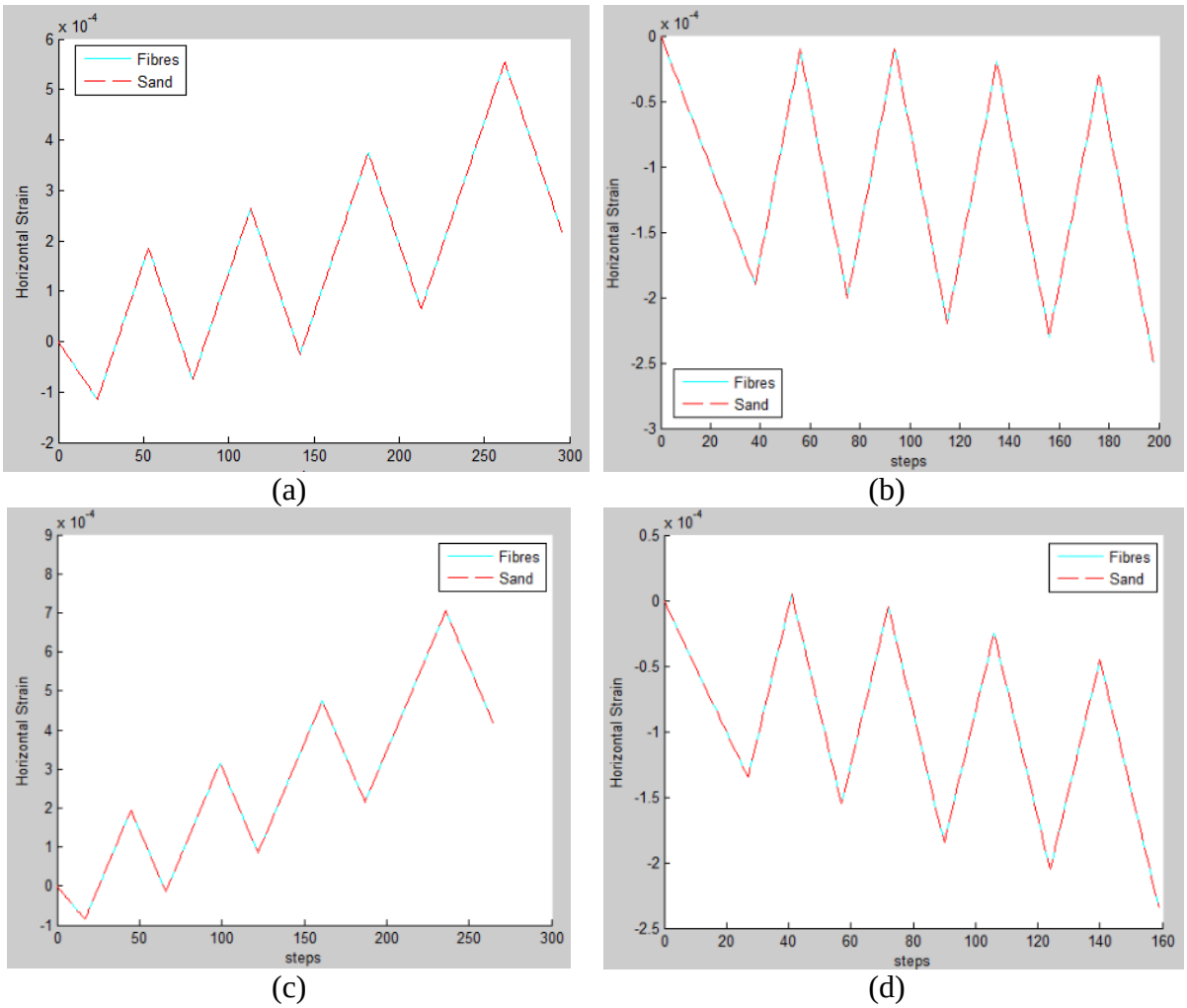

Figure 3.7 – Compatibility between radial stresses and stresses in the fibres under undrained conditions: (a) loose sand, q between -50 and 50 kPa; (b) loose sand, q between 0 and 80 kPa; (c) dense sand, q between – 50 and 50 kPa; (d) dense sand, q between 0 and 80 kPa.

According to the figure, perfect compatibility between the radial stresses in the matrix and the stresses in the fibres oriented at 0° is shown. This agreement is observed for different relative densities and different loading conditions.

4 PARAMETRIC ANALYSIS

In this chapter, a parametric analysis is performed in order to evaluate the influence of soil and fibre parameters in the cyclic behaviour of fibre-reinforced sands.

The parametric analysis is performed under undrained conditions as liquefaction occurs under these drainage conditions. In that sense, a loose sand (υ_c = 1.95; I_D = 23%) will be analysed in the parametric analysis.

4.1 INFLUENCE OF FIBRE PARAMETERS

The fibre parameters whose influence is analysed herein are: elastic modulus (E_f), fibre length (l_f) and diameter (d_f). Also, the fibre content (w_f), the sliding function (f_b) and the specific volume of the fibres (υ_f) are subjected to this parametric analysis. The composite behaviour is assessed under three aspects: q-p*, stress-strain and pore water pressure. All the simulations were performed to simulate undrained tests for 10 cycles of compression-extension, with amplitude between q = -50 kPa and q = 50 kPa. The initial parameters are the ones listed in Table 3.6.

4.1.1 Elastic modulus of the fibres

The influence of the elastic modulus of the fibres is presented in Figure 4.1. The first remark, from Figure 4.1 (a) is that fibres with higher elastic modulus produce lower axial strains as the cycles develop. This observation is intuitive to a certain extent, because the higher E_f, the more the fibres will absorb stresses, hence less strains will occur. From Figure 4.1 (b) and (c), it is possible to observe that the fibres with higher elastic modulus generate slightly higher pore water pressures. This occurs because stiffer fibres produce more confinement in the sand and consequently generate more pore pressure. While in monotonic tests the strength performances of the composite materials increase with the stiffness of the fibres (DIAMBRA, 2010), for cyclic tests they might accelerate pore pressure build up. For this reason, there is a trade-off between decreasing axial strain and pore pressure generation. Additional triaxial tests would help to understand how the elastic modulus of the fibres affects the cyclic behaviour of sands, but there is no evidence of such experiments with fibres of different stiffness.

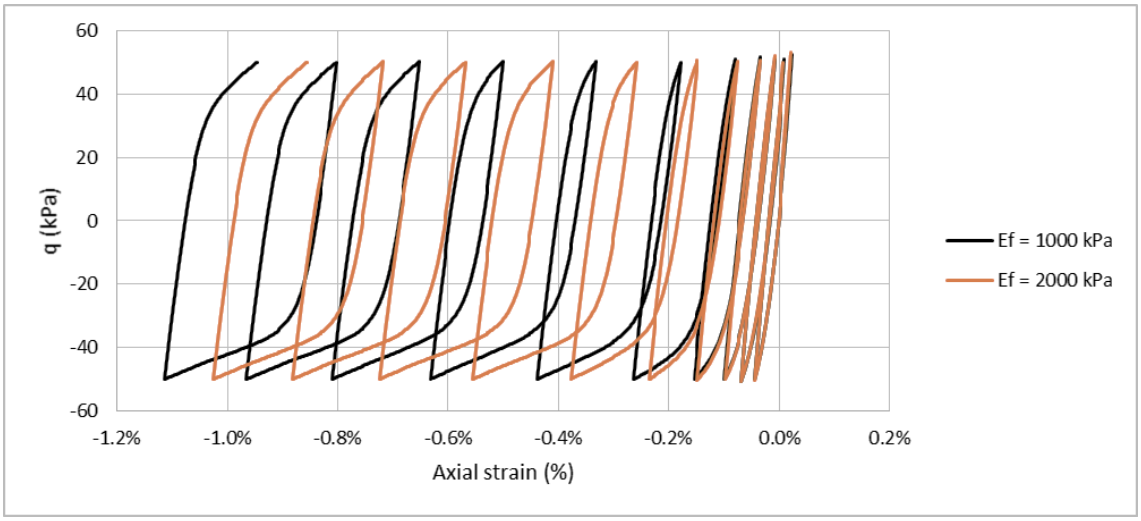

(a)

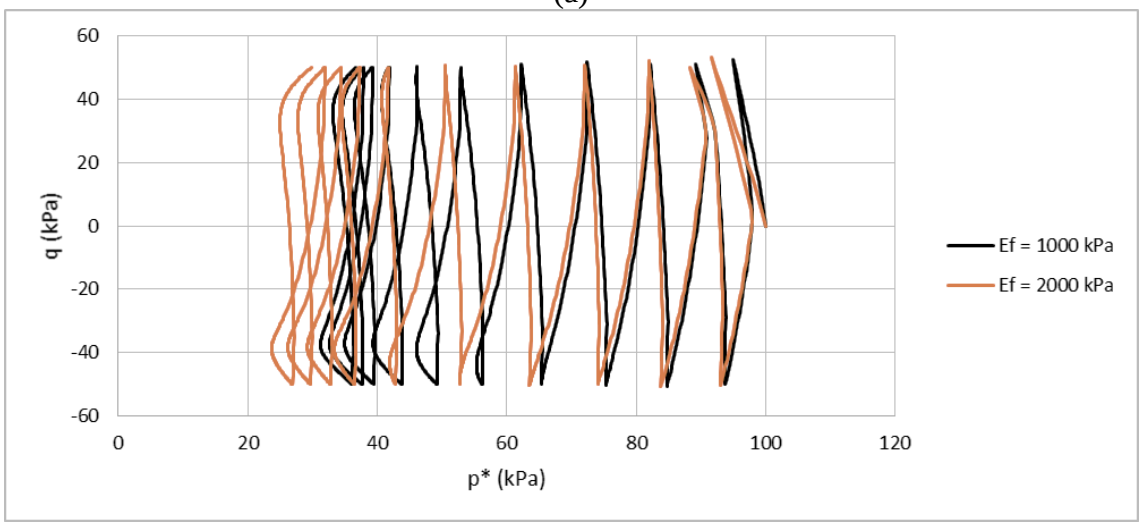

(b)

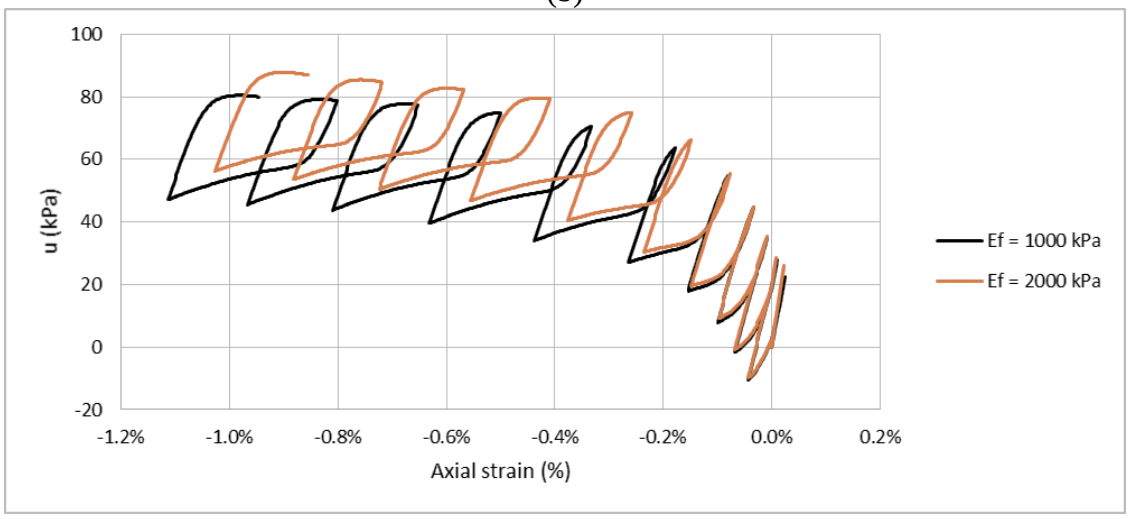

(c)

Figure 4.1 – Influence of the elastic modulus (E_f) on the undrained behaviour of the composite: (a) stress-strain; (b) *q*-*p** and (c) pore water pressure

4.1.2 Fibre content

Even though the fibre content is not exactly a fibre parameter, its influence on the behaviour of the composite is essential and is worth being assessed. Two fibre contents have been analysed: 0.5% and 1.0%.

The first clear evidence is that axial strain is smaller for higher fibre content (Figure 4.2 (a)). This finding is intuitive and has been shown by Noorzad and Amini (2014) and also by Florez et al. (2016) in cyclic triaxial tests. This occurs mainly due to the extra confinement the fibres provide to the sand matrix and also due to the bond between grains and fibres, which gives some tensile strength to the composite. The second finding is that for the sand with w_f = 0.5% the rate of decrement of the mean effective stress p^* is more significant respect to the sand with w_f = 1.0% (Figure 4.2 (b)). In other words, the simulation with smaller fibre content generates more pore pressure (Figure 4.2 (c)) and hence the stress path approaches liquefaction (p^* = 0) more rapidly. This may be more evident for a bigger number of cycles, where the addition of fibres would probably delay liquefaction, i.e. p* = 0 would be reached for a higher number of cycles. This behaviour will be further observed in Chapter 5.

4.1.3 Sliding function

As previously mentioned in 3.2.1, the sliding function f_b relates the strain in the fibres to the strain in the composite. Therefore, the closer f_b is to 1, the closer these strains will be. The higher the sliding function, the higher the strain values, and consequently the more the fibres will absorb stresses (equation (3.12)). So, it is expected that the fibre contribution to the composite is more significant (and consequently the strains are smaller) for sliding functions whose values are closer to 1. This assumption is confirmed by Figure 4.3 (a), which shows that the axial strain is lower for higher sliding functions. On the other hand, a sliding function f_b = 1 generates higher pore pressure and leads to liquefaction more rapidly respect to the case where f_b = 0.5 (Figure 4.3 (b) and (c)).

As for the elastic modulus of the fibres (4.1.1) there is a trade-off between reducing axial strain and pore pressure. Further cyclic triaxial tests – with fibres of different roughness, for example – would allow more conclusive observations.

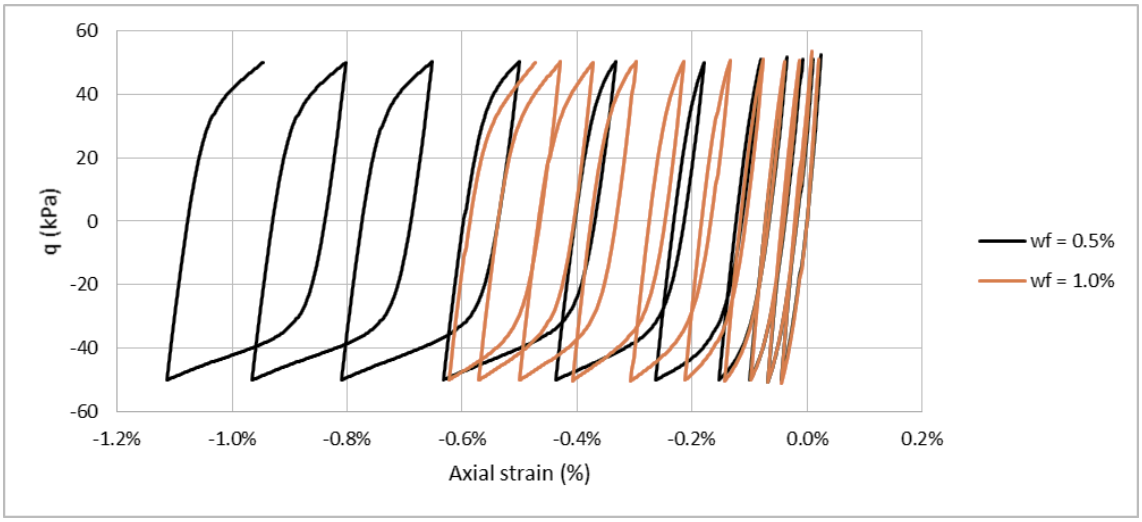

(a)

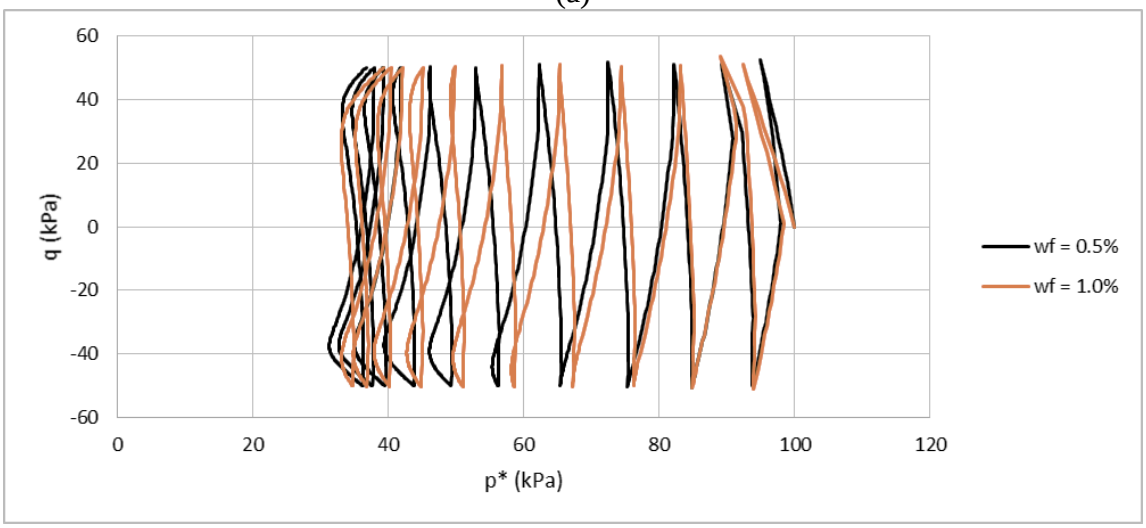

(b)

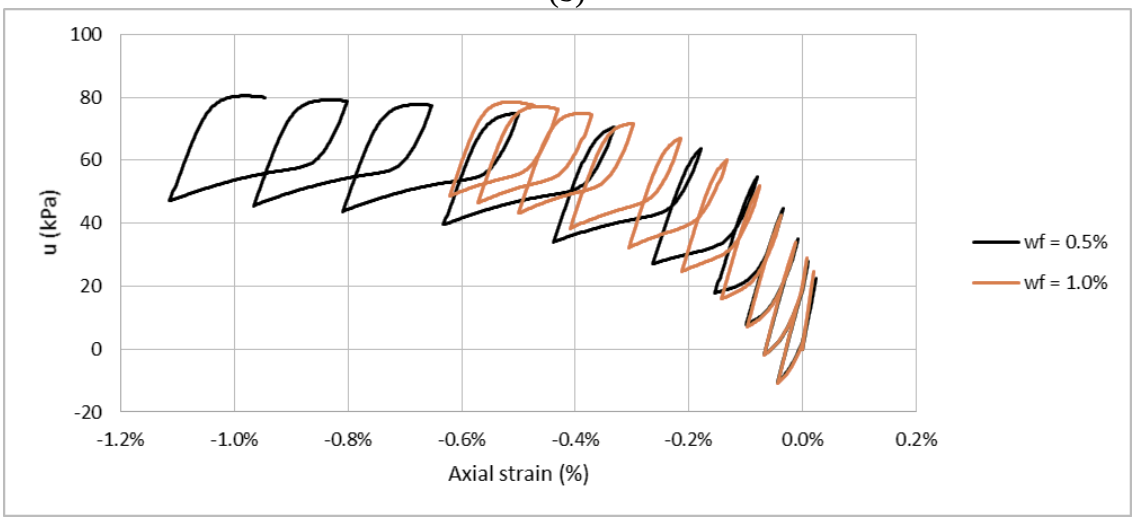

(c)

Figure 4.2 – Influence of the fibre content (w_f) on the undrained behaviour of the composite: (a) stress-strain; (b) q-p^* and (c) pore water pressure

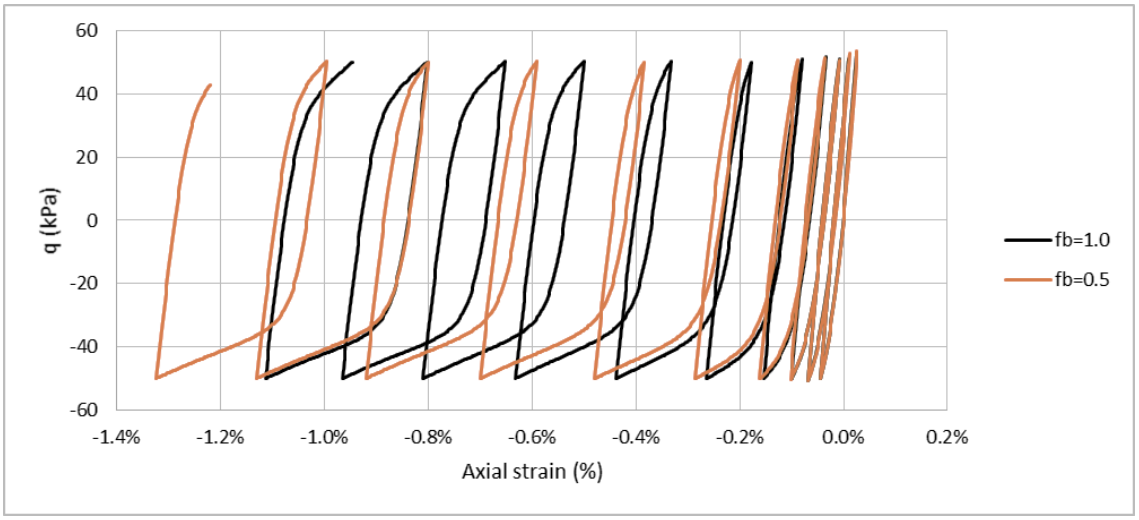

(a)

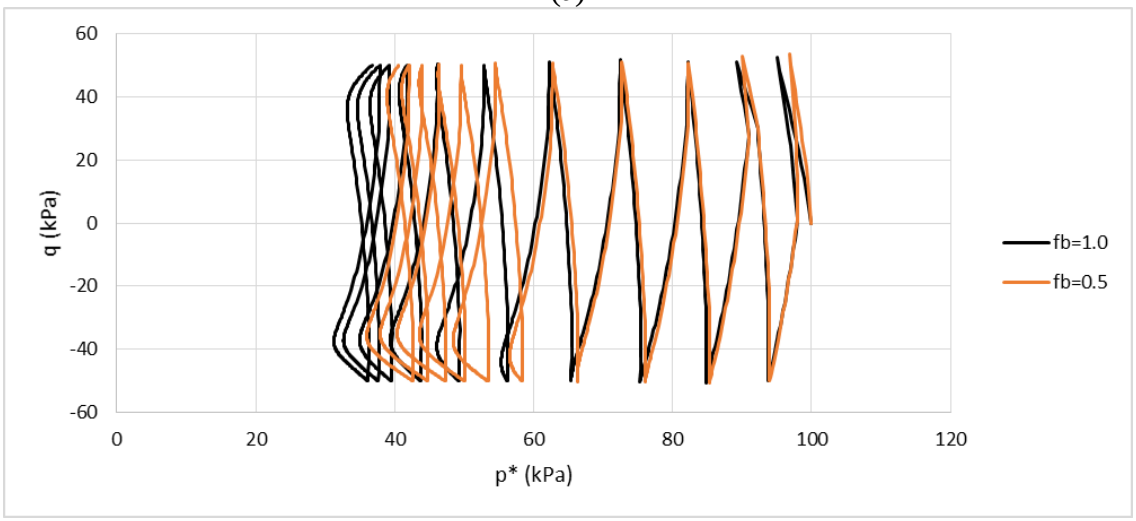

(b)

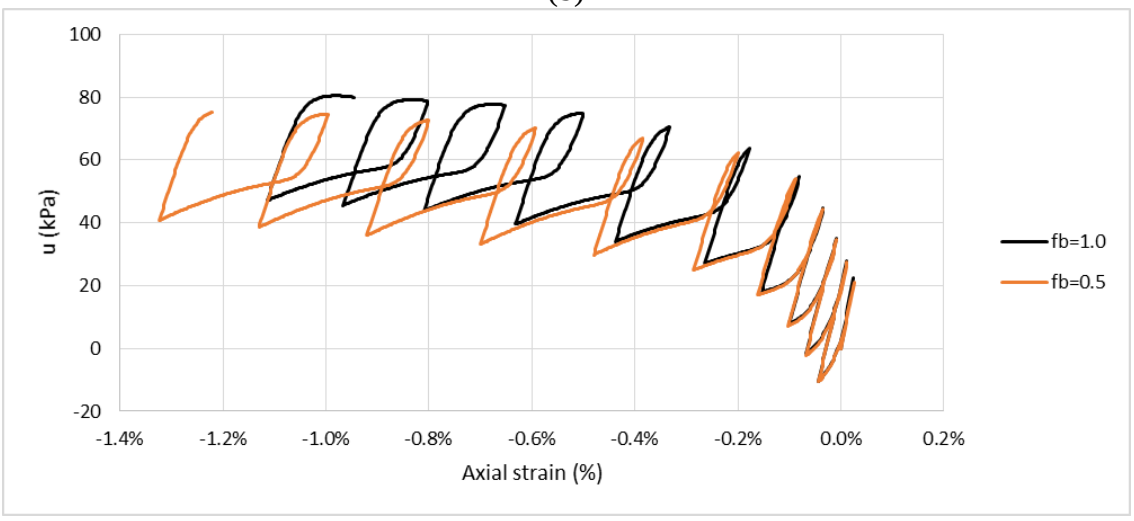

(c)

Figure 4.3 – Influence of the sliding function (f_b) on the undrained behaviour of the composite: (a) stress-strain; (b) q-p^* and (c) pore water pressure

4.1.4 Fibre length and diameter

As stated in section 3.2.2, equation (3.15), the fibre-soil bonding occurs up to a threshold σ_f^L, which is the stress where pull-out of the fibre occurs. This threshold is influenced by the fibre length l_f and diameter d_f. Up to this stress, it is assumed that l_f and d_f do not have any influence in the composite behaviour. The influence of the fibre length and diameter is accounted for by the specific volume of the fibres (υ_f). Longer fibres usually steal more voids from the matrix, leading to higher values of υ_f.

Therefore the stress-strain, q-p^* and pore pressure plots are coincident for the first cycles irrespective of the fibre length (Figure 4.4 (a), (b) and (c)), which shows that, according to the model assumptions, the behaviour of the composite is not affected by these characteristics for the first cycles. Once the pull-out stress is reached, the plots start diverging. From this diverging point on, higher axial strains take place for shorter fibres. The second Ishihara's criterion for liquefaction (ε_a = 5%) will then be reached firstly for the composite with shorter fibres. On the contrary, longer fibres generate slightly higher pore water pressures and hence the specimens with longer fibres tend to reach p^*= 0 for a smaller number of cycles if compared to the samples with shorter fibres. So, on the one hand, longer fibres seem to reach the first Ishihara's criterion firstly, whereas shorter fibres reach the second Ishihara's criterion first. Once again, the trade-off between axial strain and pore water pressure arises.

Noorzad and Amini (2014) showed that an increase in fibre length increases the number of cycles needed to reach liquefaction. However, the authors affirm that liquefaction onset was considered as the state when axial strain becomes equal to 5%, i.e. the second Ishihara's criterion. Therefore, the model response is consistent with the authors' finding, as it has been shown herein that longer fibres reduce axial strains. However, it is not possible to affirm what would have happened to the number of cycles to reach liquefaction if the first Ishihara's criterion had also been considered. The authors do not mention the influence of fibre length in the pore pressure build up.

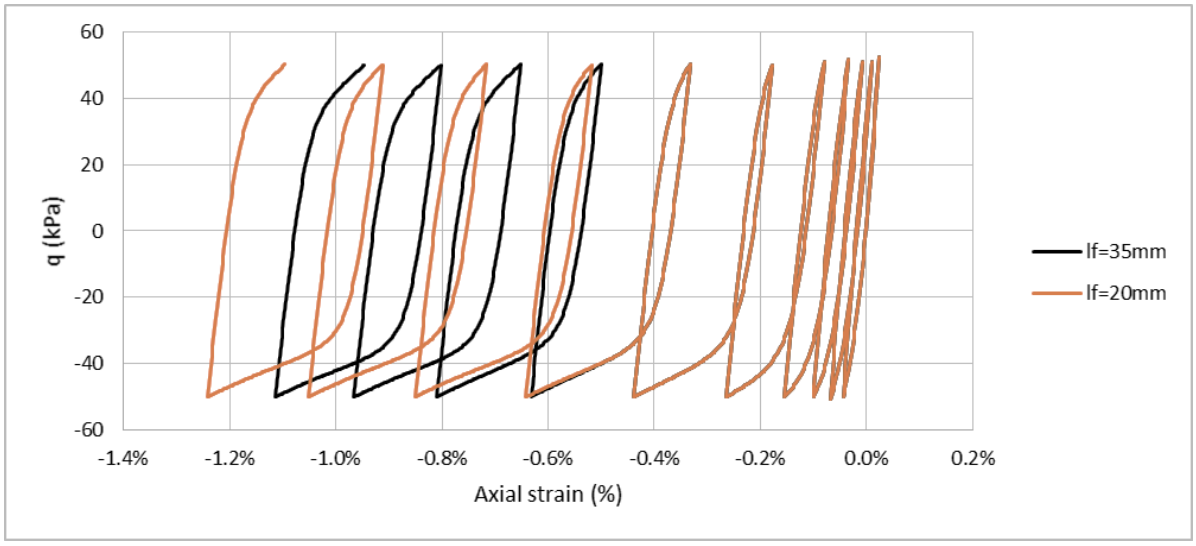

(a)

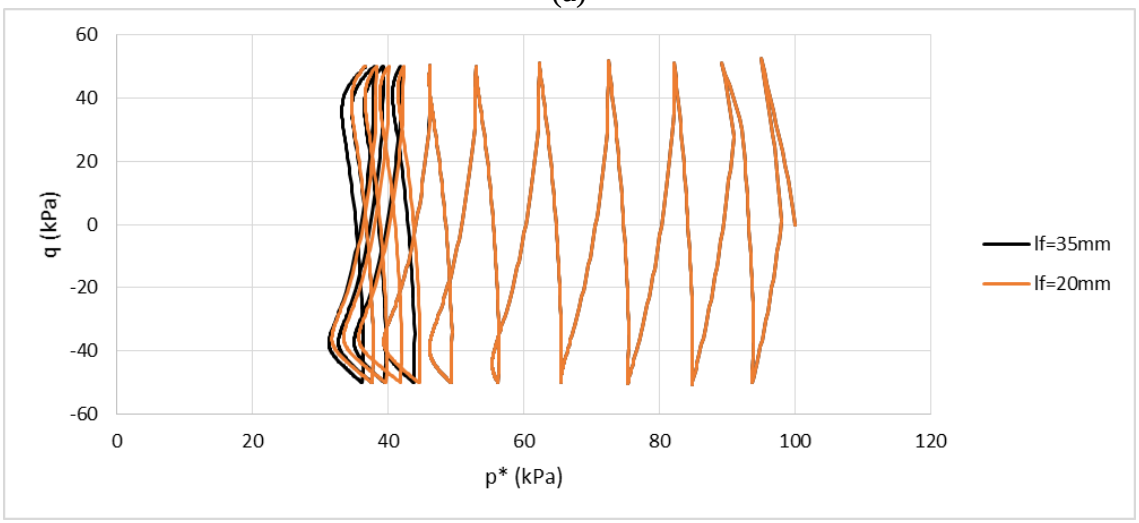

(b)

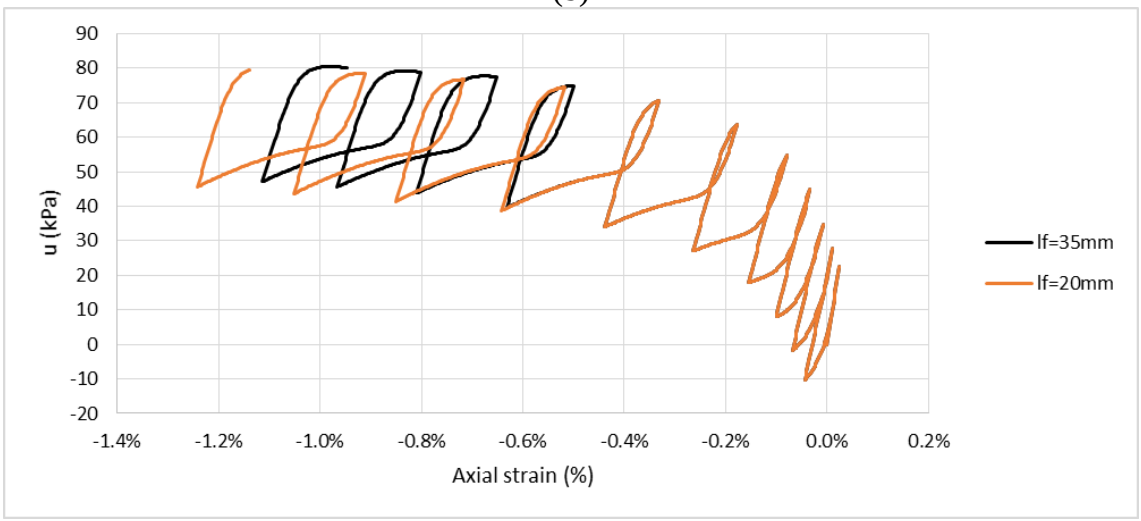

(c)

Figure 4.4 – Influence of the fibre length (l_f) on the undrained behaviour of the composite: (a) stress-strain; (b) q-p^* and (c) pore water pressure

4.1.5 Specific volume of the fibres

As cited in 2.6.2, Diambra et al (2013) stated that part of the voids within the matrix is "stolen" by the fibres. The more voids attached to the fibres, the higher the specific volume and consequently the more significant the densification of the specimen. In that sense, it seems logical that an increase in specific volume decrease the axial strain, as shown in Figure 4.5 (a). Concerning the stress paths, υ_f seems not to play an important role in the decrement rate of effective mean pressure p^*, especially for the first cycles. It is worth noticing, though, that as the stress path approaches $p^* = 0$, increasing υ_f seems to produce slightly higher pore pressures. Hence, higher specific volumes of the fibres may hasten the approximation of stress paths to the first Ishihara's criterion for liquefaction ($p^* = 0$) but on the other hand they seem to delay the occurrence of the second criterion (5% axial strain). More conclusive findings could only be stated with actual tests using different types of fibres, especially those whose υ_f have already been calibrated in previous studies.

4.2 INFLUENCE OF SOIL PARAMETERS

The soil parameters whose influence is analysed herein are those that need to be calibrated: k_r, B, R, A, k_d (parameters of the Severn-Trent model) and ζ (constitutive parameter of the proposed adjustment factor). The influence of Severn-Trent parameters on the monotonic response of sands was examined by Gajo and Muir Wood (1999). The composite behaviour is assessed under three aspects: stress-strain, q-p^* and pore water pressure. All the simulations were carried out for undrained tests after 10 cycles of compression-extension, with stress amplitude between q = -50 kPa and q = 50 kPa. The initial parameters are the ones listed in Table 3.6.

The first parameter is k_r, which links the state parameter to the current strength. Figure 4.6 shows that this parameter plays an important role in the development of the cycles under undrained conditions. Both the stress-strain behaviour and the stress path of the composite are notably affected by k_r. Figure 4.6 (a) shows that, after 10 cycles of load-unload, the axial strain was roughly -1.1% for k_r = 1.5. On the other hand, the axial strain was almost -1.8% for k_r = 3.0. From Figure 4.6 (b) and (c), it is also evident that this parameters affects the pore pressure generation and hence the stress path of the composite. It is possible to observe that increasing k_r hastens the approach of the stress path to $p^* = 0$. From $p^* = 100$ kPa to $p^* = 60$ kPa, for instance, the model developed 4 cycles for k_r = 1.5 and 3 cycles for k_r = 3.0. Thus, it can be affirmed that an increase of k_r enables the model to prevent liquefaction from the point of view

of both criteria – decreasing axial strain and delaying the approximation of the stress path to $p^* = 0$.

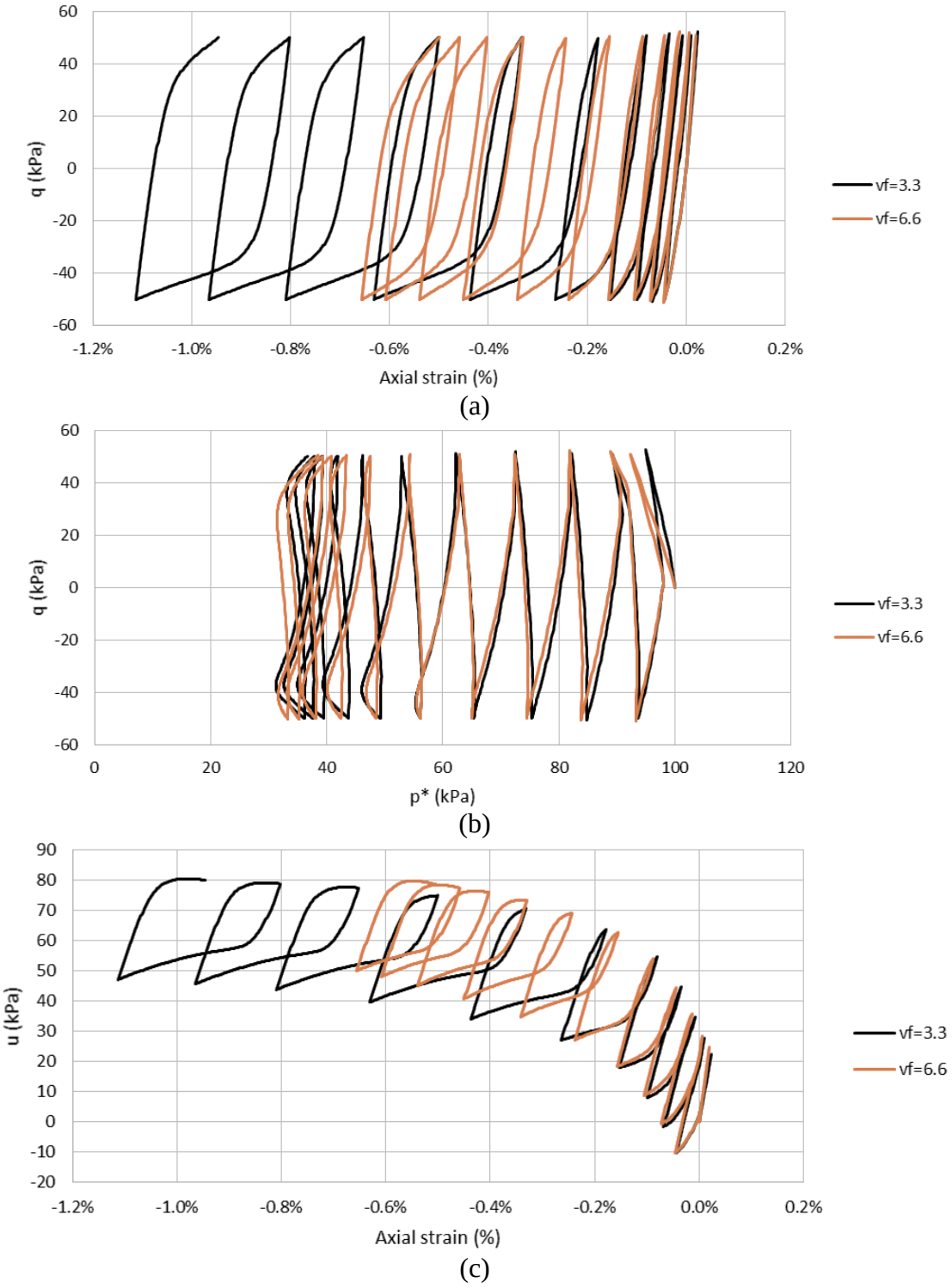

Figure 4.5 – Influence of the specific volume of the fibres (υ_f) on the undrained behaviour of the composite: (a) stress-strain; (b) q-p^* and (c) pore water pressure

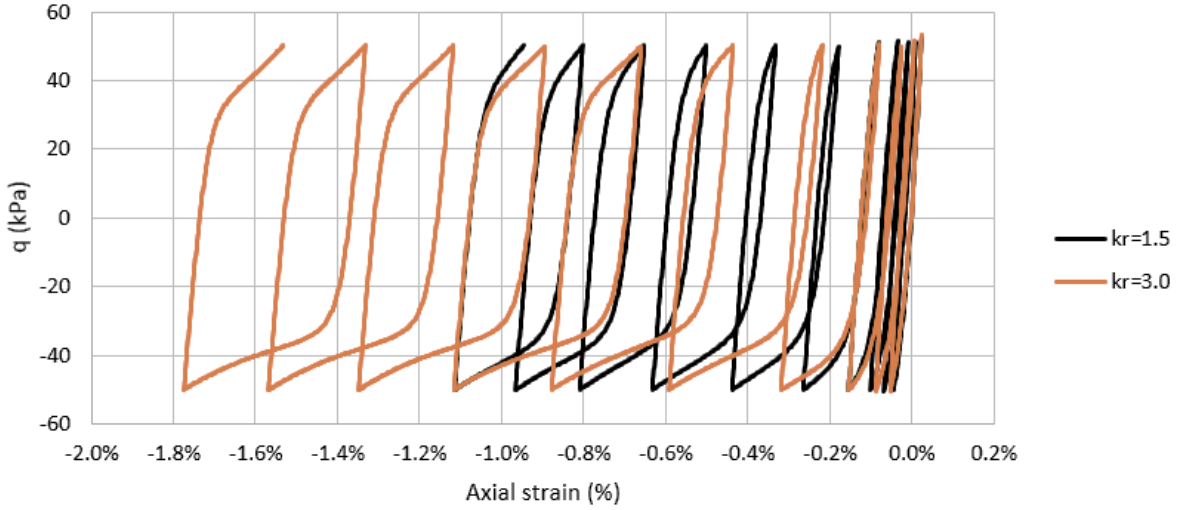

(a)

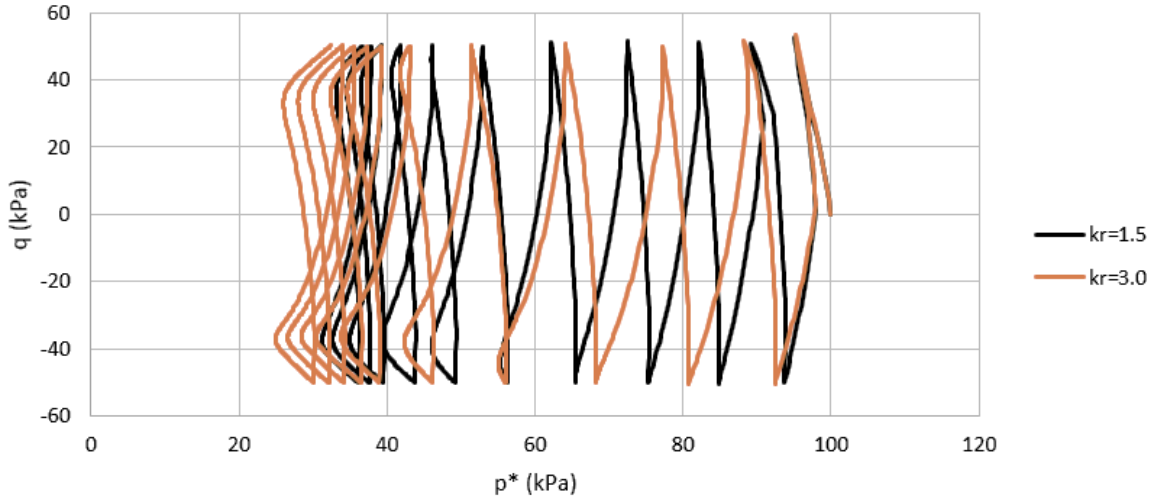

(b)

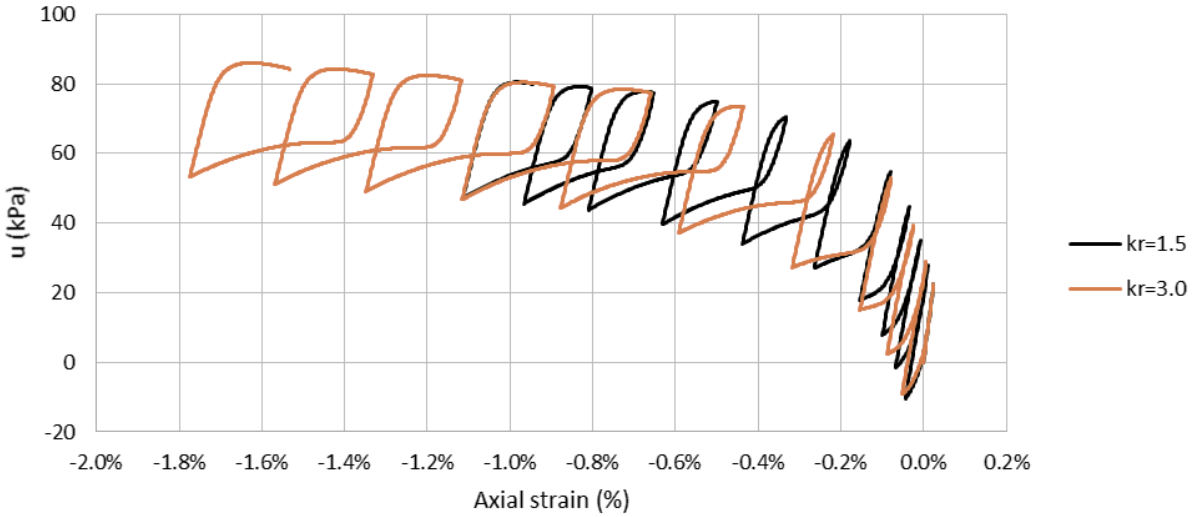

(c)

Figure 4.6 – Influence of the parameter k_r on the undrained behaviour of the composite: (a) stress-strain; (b) *q*-*p** and (c) pore water pressure

The second parameter is *B*, which controls the hyperbolic stiffness relationship. Figure 4.7 shows that this parameter has an essential influence on the cyclic behaviour of the composite. Not only does *B* significantly affect the magnitude of axial strains but also has a noticeable influence on the pore pressure generation. Figure 4.7 (a), for example, demonstrates that for $B = 0.00012$ the simulation presents -2.3% axial strain after 10 cycles. In turn, for $B = 0.00006$ the axial strain is less than -1.2% for the same number of cycles. Still, Figure 4.7 (b) shows that for $B = 0.00012$ the stress path reaches $p^* = 40$ kPa during the fourth cycle, whereas for $B = 0.00006$ the reaches the same effective mean pressure after seven cycles. These findings clearly indicate that the cyclic behaviour of the composite is importantly affected by the calibration of *B*.

The third parameter is *R*, which is the ratio of sizes of yield surface and strength surface. Even though this parameter does not have a significant influence in the axial strains (Figure 4.8 (a)), it may be important to define the first Ishihara's criterion for liquefaction ($p^* = 0$) as it seems to affect the number of cycles wherefore the mean pressure approaches zero (Figure 4.8 (b) and (c)). From the author's knowledge, *R* usually is usually assumed to be 0.1, as it can be confirmed in prior studies (DIAMBRA, 2010; DIAMBRA et al., 2013; CORTI, 2016).

The fourth parameter is *A*, which is a multiplier in the flow rule. From Figure 4.9, it can be seen that the parameter *A* plays an important role not only in the axial strains but also in the pore pressure and hence in the stress path. Higher *A* values are shown to lead to higher axial strains and higher pore water pressures. Therefore, increasing *A* seems to make the specimen liquefy for a smaller number of cycles, considering both Ishihara's criteria. This finding can be confirmed by Figure 4.9 (a) and (b). Figure 4.9 (a) shows that for $A = 0.75$ the axial strain reaches -1.1% for 10 cycles while for $A = 0.375$ it is less than -0.5% for the same number of cycles. Additionally, Figure 4.9 (b) shows that the stress path approaches $p^* = 60$ kPa in the fifth cycle when $A = 0.75$, while for $A = 0.375$ this only happens after the eighth cycle.

Finally, the fifth parameter is k_d, which represents the state parameter contribution in the flow rule. Figure 4.10 shows that it significantly influences the axial strains and the stress path. It is evident that an increase in k_d reduces both axial strain and pore pressure generation. Thus, k_d is an important parameter for the cyclic behaviour of the composite, since it affects both Ishihara's criteria for liquefaction.

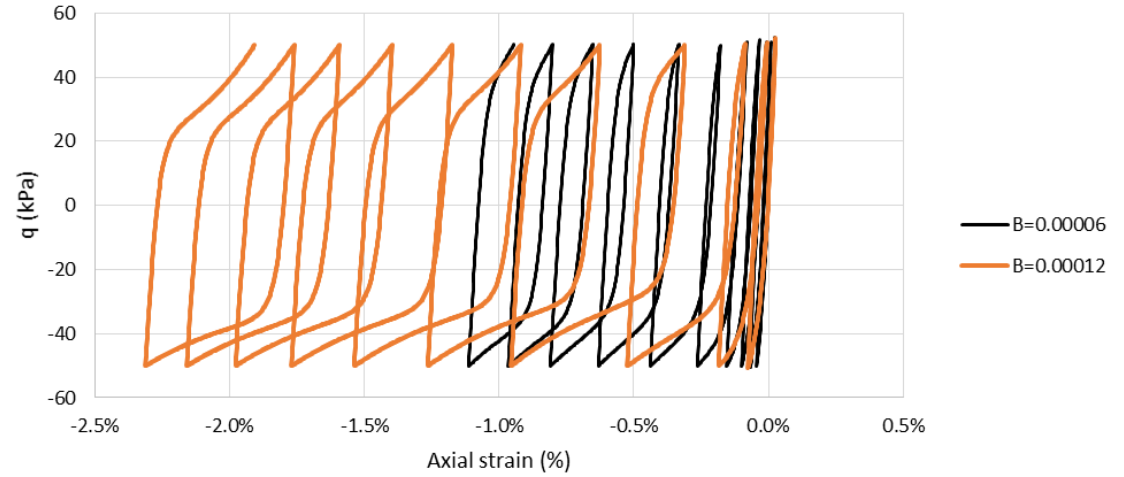

(a)

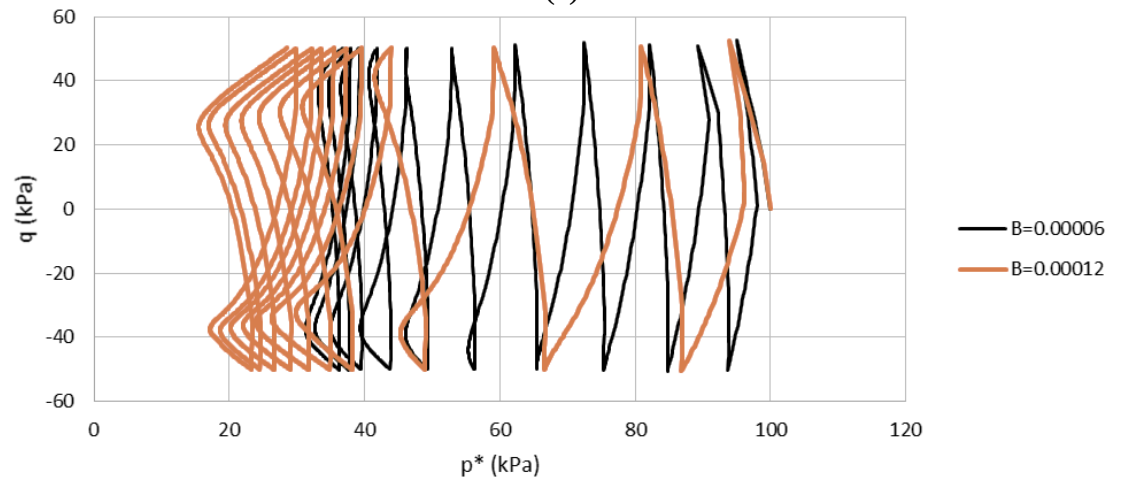

(b)

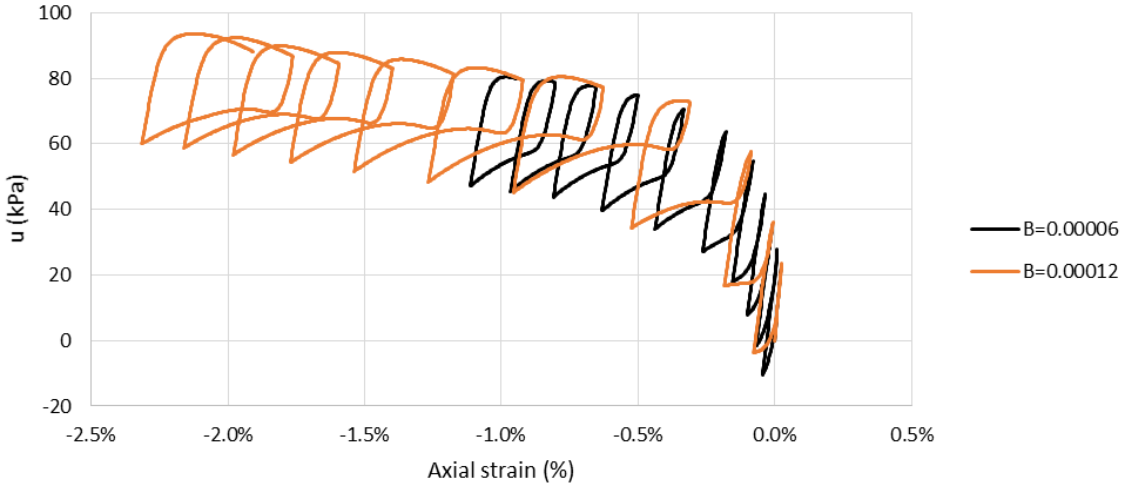

(c)

Figure 4.7 – Influence of the parameter *B* on the undrained behaviour of the composite: (a) stress-strain; (b) *q*-*p** and (c) pore water pressure

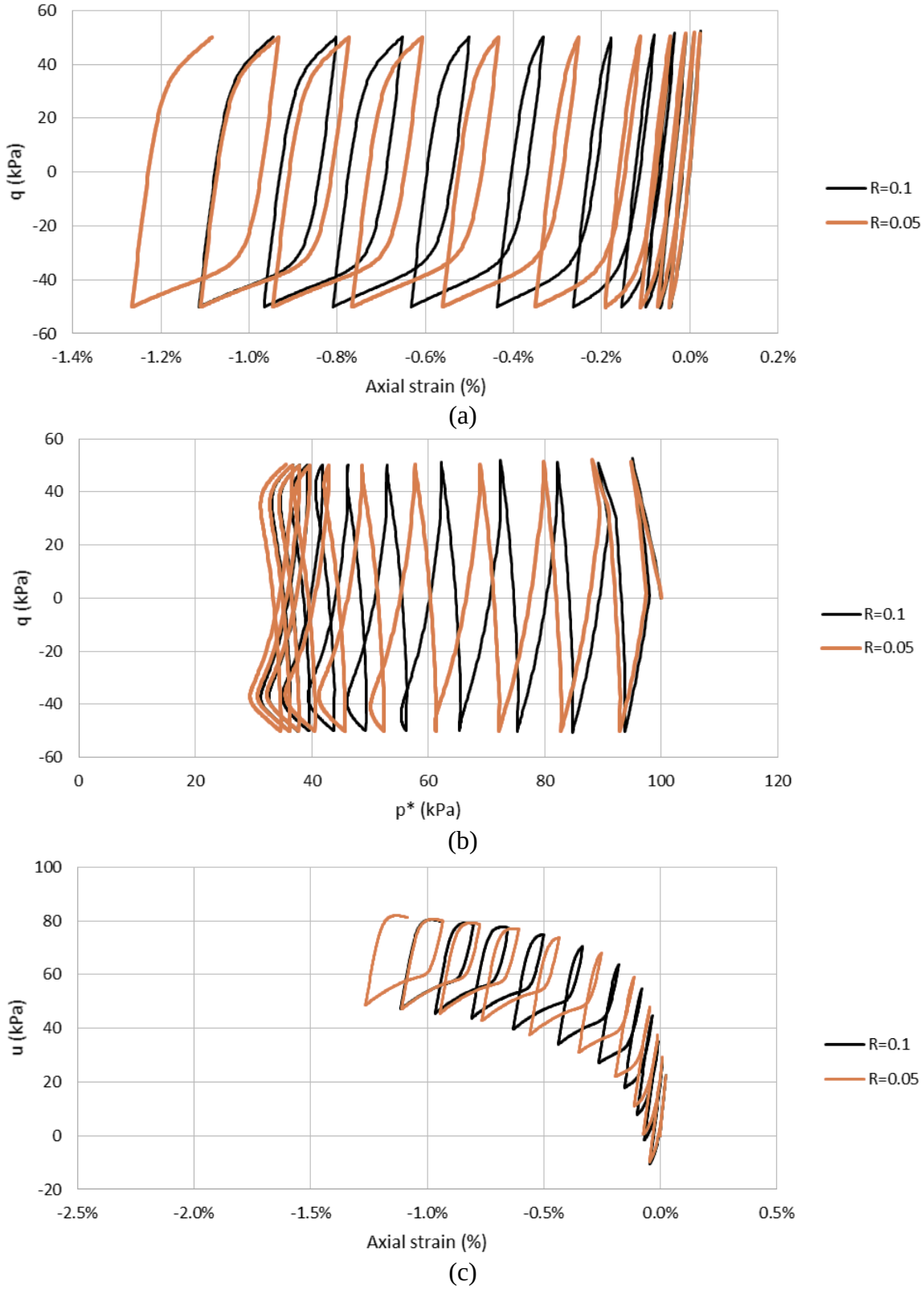

Figure 4.8 – Influence of the parameter *R* on the undrained behaviour of the composite: (a) stress-strain; (b) *q*-*p** and (c) pore water pressure

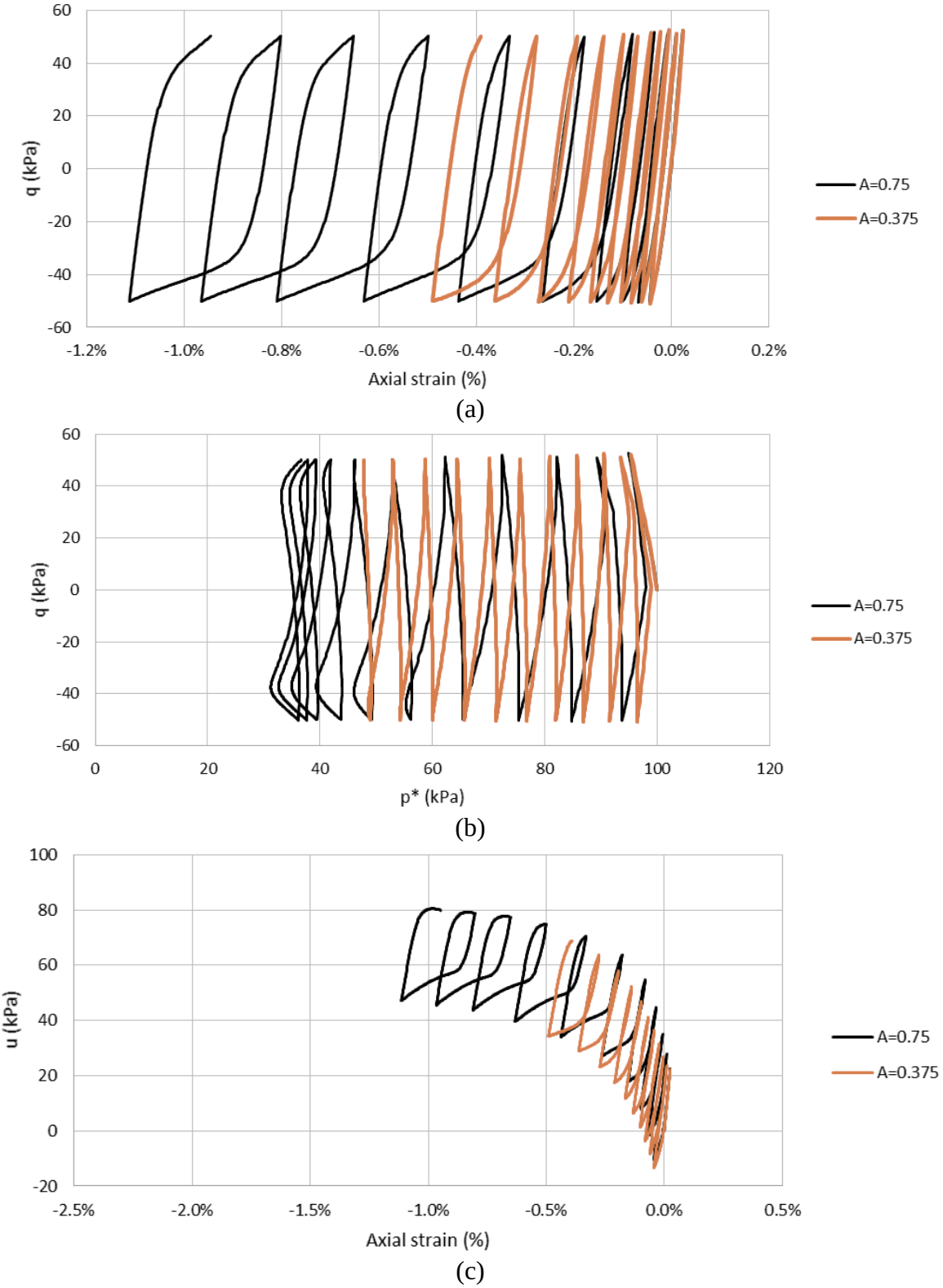

Figure 4.9 – Influence of the parameter *A* on the undrained behaviour of the composite: (a) stress-strain; (b) *q*-*p** and (c) pore water pressure

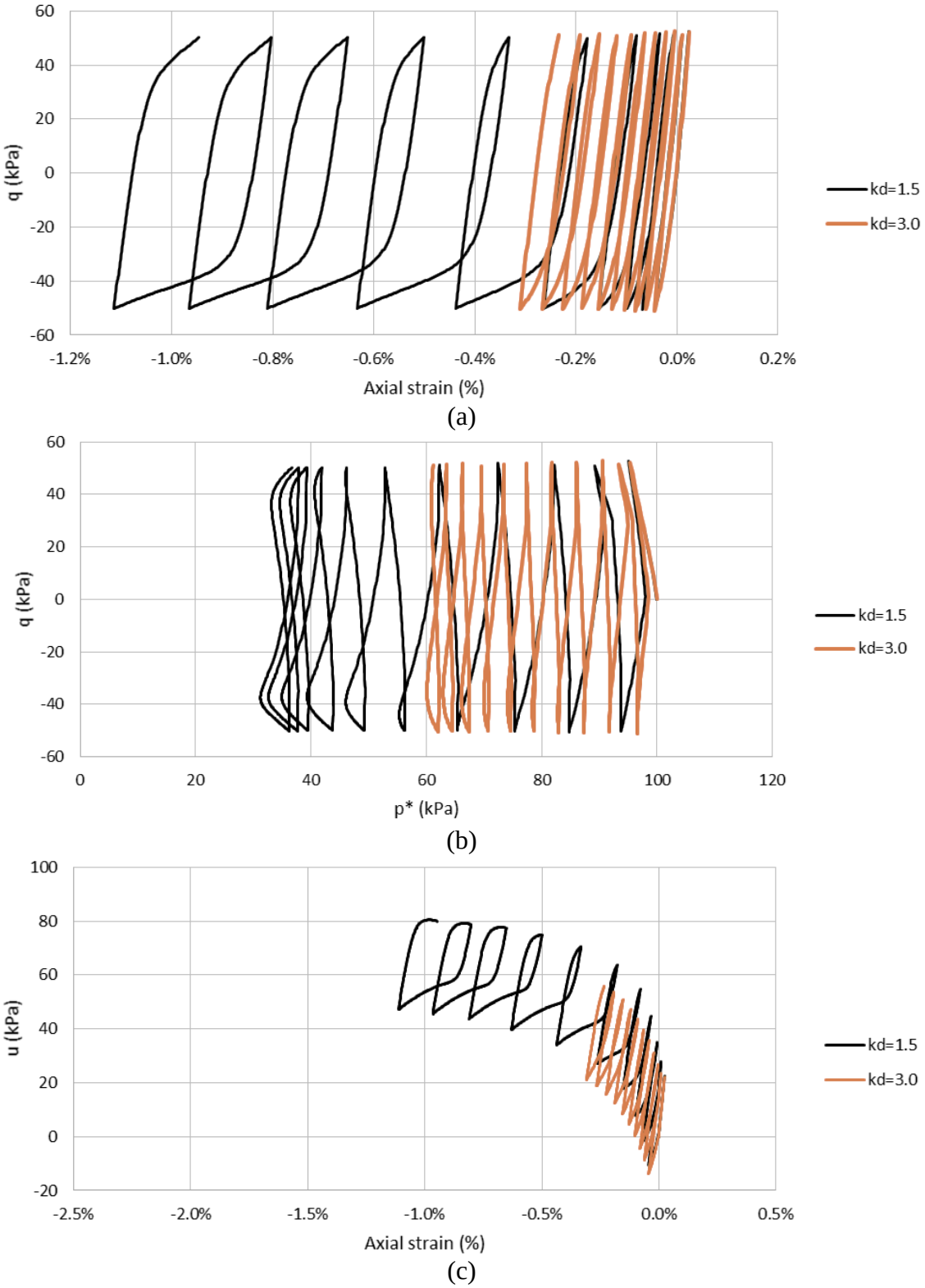

Figure 4.10 – Influence of the parameter k_d on the undrained behaviour of the composite: (a) stress-strain; (b) *q*-*p** and (c) pore water pressure

Finally, a parametric analysis of the proposed constitutive parameter ζ for the adjustment factor *AF* needs to be carried out.

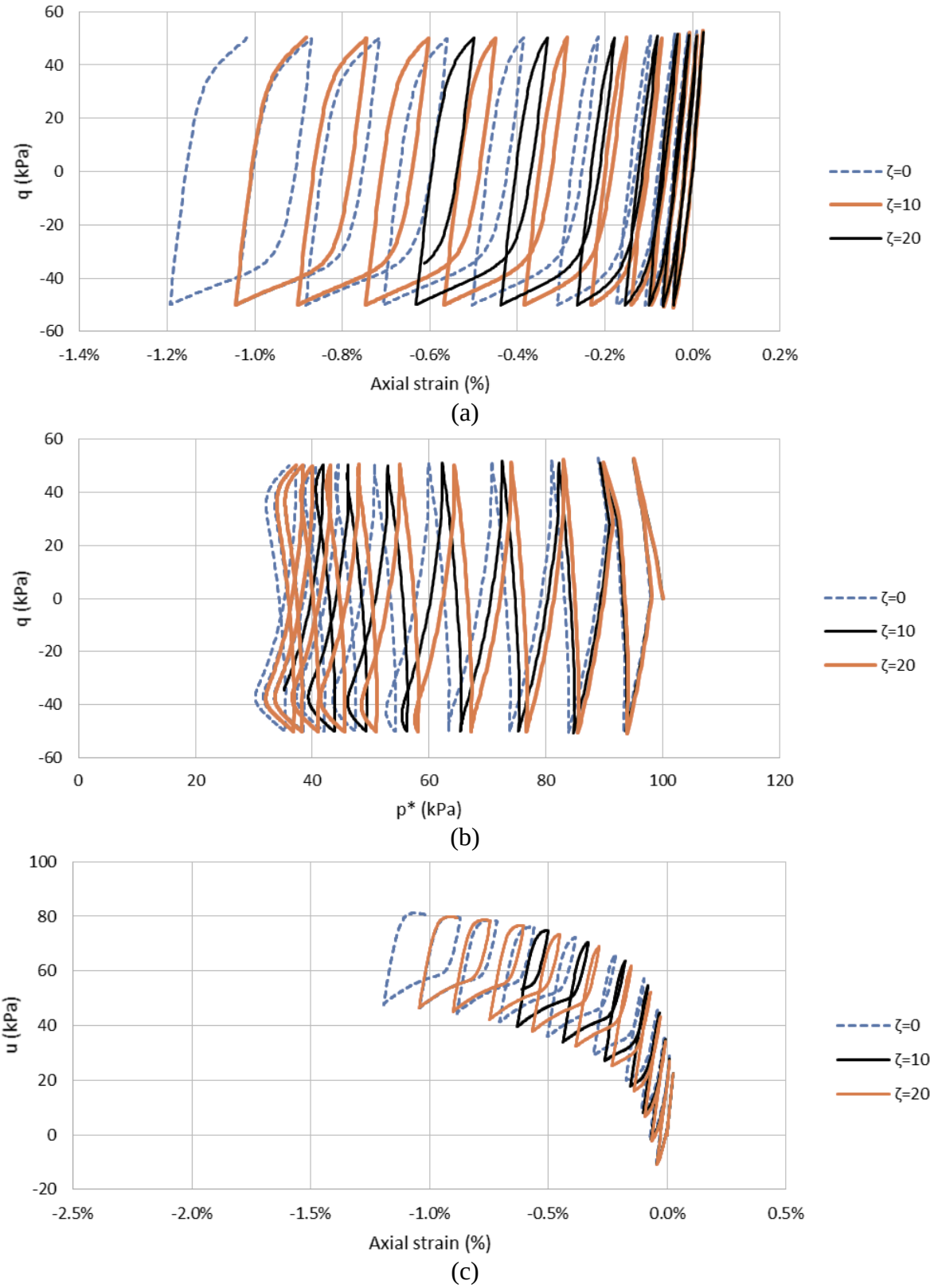

Figure 4.11 – Influence of the parameter ζ on the undrained behaviour of the composite: (a) stress-strain; (b) *q*-*p** and (c) pore water pressure

Figure 4.11 shows that smaller ζ cause higher axial strains and generate more pore pressure, accelerating liquefaction under both Ishihara's criteria. The effect of the multiplier ζ in the

adjustment factor is important to account for the fibre contribution in the *q-p** behaviour for the first cycles. It is known from experimental results (NOORZAD; AMINI, 2014; FLOREZ et al., 2016) that fibre inclusions reduce pore pressure generation since the first cycles. However, without the adjustment factor *AF*, this effect is only perceived after a certain number of cycles. Further calibration will show that ζ ranges from 10 to 20 to the studied sands. Hence these values are also used in the parametric analysis. Despite the importance of the adjustment factor and its multiplier ζ, it is hard to relate its values to any characteristic of the sand, being such values merely empirically based so far.

After analysing all the parametric analysis, it is possible to observe that some parameters affect both liquefaction's criteria whereas others only affect one of them. Still, some of them are consistent in delaying or hastening liquefaction according to both criteria whereas others present a trade-off between the 1st and the 2nd Ishihara's criteria. Table 4.1 summarises the effect of the *increase* of each parameters in the two criteria for liquefaction.

Parameter	Ishihara's criterion	
	Approach p*=0 (1st criterion)	Axial strain (2nd criterion)
k_r	Delays	Decreases
B	Hastens	Increases
R	Slightly delays	-
A	Hastens	Increases
k_d	Delays	Decreases
ζ	Delays	Decreases

Table 4.1 – Effect of the increase of each parameter in the Ishihara's liquefaction criteria

Analysing Table 4.1 and Figure 4.6 to Figure 4.10, it can be stated that the parameters k_r, B, A, k_d and ζ are those which mostly affect the cyclic behaviour of fibre-reinforced soils under undrained conditions. Such parameters not only affect both liquefaction criteria but also seem to affect the composite behaviour in a more remarkable magnitude.

Thus, these parameters are the most important parameters in the calibration of the constitutive model. Therefore, special attention will be given to these parameters while calibrating them for model validation.

5 VALIDATION OF THE MODEL

In this chapter, the model is validated and calibrated with experimental results. Due to the scarcity of cyclic triaxial tests on fibre-reinforced sands in the literature, the proposed model will firstly be compared to monotonic drained tests carried out by Festugato (2008) and Consoli et al. (2009b). The authors used Osorio sand reinforced with polypropylene fibres. Most of the soil and fibre characteristics were obtained from this study. The critical state parameters, though, were drawn by Dos Santos et al. (2010). After the calibration with these monotonic triaxial tests, cyclic simulations are performed and compared to cyclic undrained triaxial tests carried out by Florez et al. (2016). Additionally, other experimental research conducted by Noorzad and Amini (2014) will be utilised.

5.1 MATERIALS

5.1.1 Osorio sand

Osorio sand was used by Festugato (2008), Dos Santos et al. (2010) and Florez et al. (2016). This sand was recovered from the Osorio region in southern Brazil and can be described as a fine, clean quartzitic sand with a uniform grading (DOS SANTOS et al., 2010). No organic matter was observed. The properties of Osorio sand are given in Table 5.1 whereas the particle size distribution is presented in Figure 5.1.

The critical state parameters for confining pressures less than 1000 kPa were given by Dos Santos et al. (2010): Γ = 1.95 and λ = 0.022. The critical state friction angle found by these authors is 30.5°.

Table 5.1– Properties of Osorio sand (DOS SANTOS et al., 2010)

Properties	Osorio sand
Specific gravity of solids	2.62
Uniformity coefficient, C_u	2.1
Curvature coefficient, C_c	1.0
Effective diameter, D_{10}, mm	0.09
Mean diameter, D_{50}, mm	0.16
Minimum void ratio, e_{min}	0.6
Maximum void ratio, e_{max}	0.9

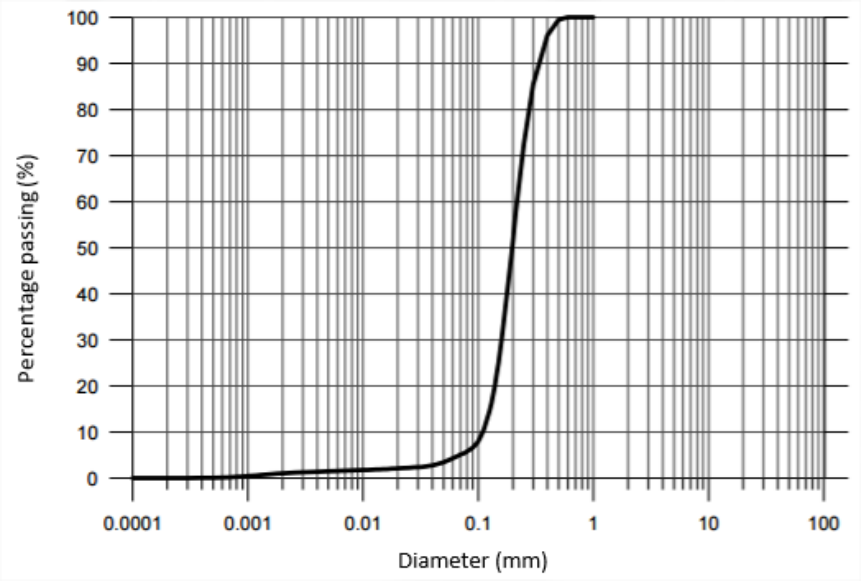

Figure 5.1– Particle size distribution of Osorio sand (FESTUGATO, 2008)

5.1.2 Fibres for Osorio sand

Polypropylene fibres were employed by Festugato (2008) and Florez et al. (2016) as reinforcement elements. These fibres have a relative density of 0.91, a tensile resistance of 120 MPa and an elastic modulus of 3 GPa. The fibre content was 0.5% by weight in both studies. Two fibre lengths were used by Festugato (2008): 24 mm and 50 mm, both of them with 0.100 mm of diameter. Florez et al. (2016) used 24 mm fibres only.

5.1.3 Babolsar sand

Noorzad and Amini (2014) analysed the performance of fibre reinforcement in enhancing the liquefaction resistance of loose and medium sand deposits. The properties and the particle size distribution of Babolsar are displayed in Table 5.2 and in Figure 5.2, respectively.

Table 5.2– Properties of Babolsar sand (NOORZAD; AMINI, 2014)

Properties	Babolsar sand
Specific gravity of solids	2.74
Uniformity coefficient, C_u	1.8
Curvature coefficient, C_c	1.3
Mean diameter, D_{50}, mm	0.19
Minimum void ratio, e_{min}	0.58
Maximum void ratio, e_{max}	0.86

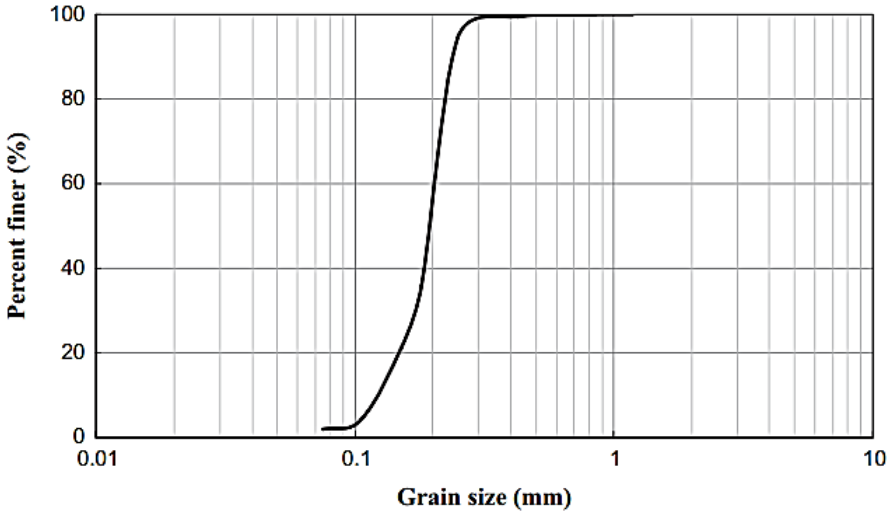

Figure 5.2– Particle size distribution of Babolsar sand (NOORZAD; AMINI, 2014)

5.1.4 Fibres for Babolsar sand

Monofilament polypropylene fibres were used as soil reinforcement. The fibre diameter was 0.023 mm and the fibre lengths were 6, 12 and 18 mm. They presented specific gravity of 0.91, tensile strength of 400 MPa and elastic modulus of 4.1 GPa. The specimens were reinforced with fibre contents of 0.5% and 1.0% by weight of dry soil.

5.2 MONOTONIC TRIAXIAL TESTS

5.2.1 Osorio sand

Festugato (2008) carried out monotonic drained triaxial tests in specimens 50 mm diameter and 100 mm long. Two confining pressures are analysed herein: 50 kPa and 100 kPa for unreinforced specimens and 20 kPa and 100 kPa for fibre-reinforced specimens. Stress-strain response and volumetric behaviour are used to calibrate the parameters. The calibration process starts with the unreinforced specimens. In this stage, only the Severn-Trent parameters need to be calibrated, once there is no fibre contribution. Even though the parametric analysis presented in Chapter 4 concerned exclusively cyclic undrained tests, a full parametric analysis for monotonic – both drained and undrained – triaxial tests was presented by Gajo and Muir Wood (1999). Based on such authors' research, the parameters k_r, B, R, A and k_d were calibrated for Osorio sand. The values for these parameters are given in Table 5.3.

Table 5.3 – Severn-Trent model parameters for Osorio sand

Soil parameter	Value
k_r	3.0
B	0.0006
R	0.1
A	0.75
k_d	1.5
ζ	14

A comparison between experimental results and model simulations for unreinforced specimens is shown in Figure 5.3.

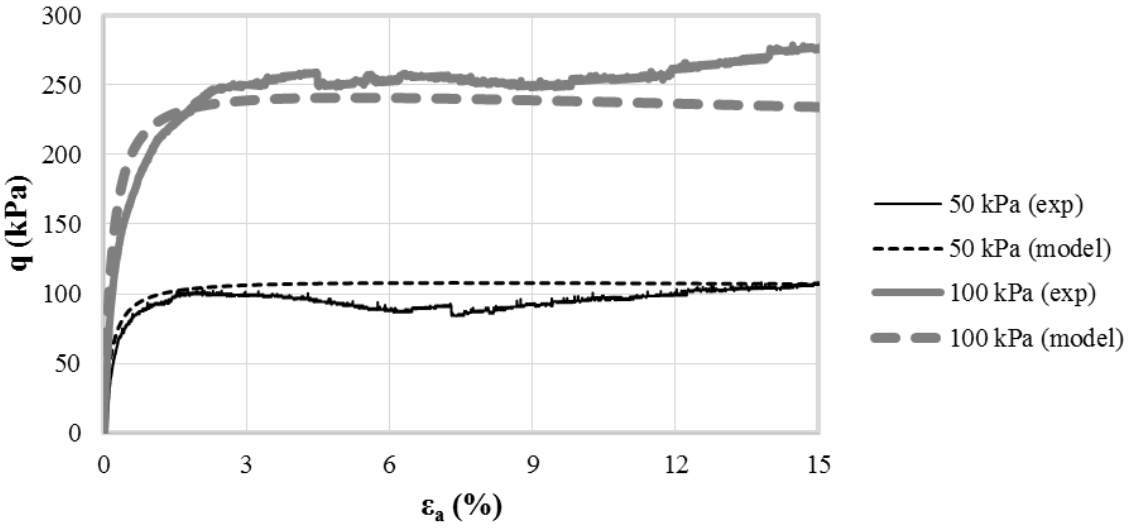

(a)

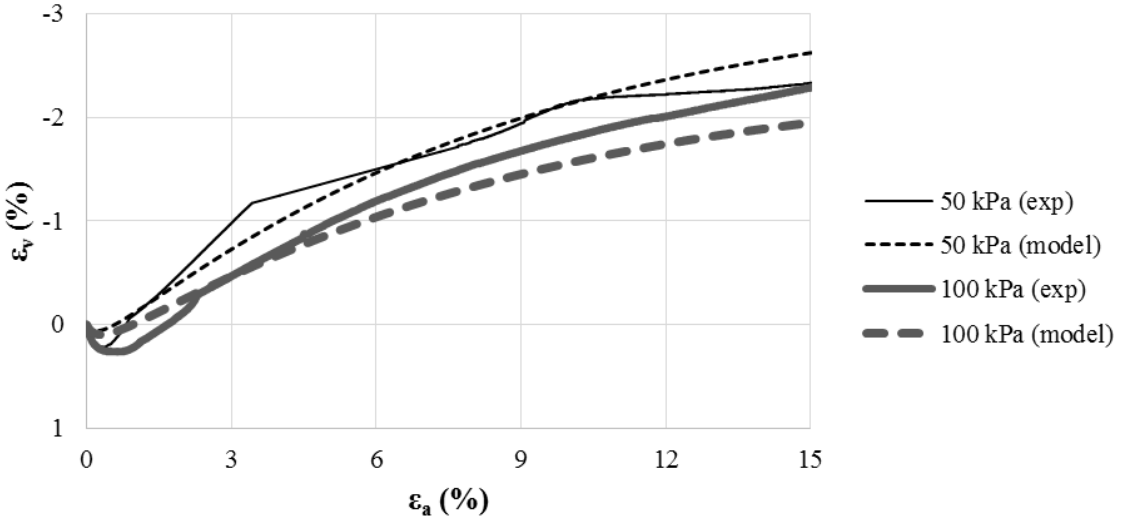

(b)

Figure 5.3– Drained triaxial test results and model simulations for unreinforced Osorio sand: (a) stress-strain and (b) volumetric behaviour

Good agreement between test results and model simulations is observed for unreinforced specimens. The model successfully captured the influence of the confining pressure in the stress-strain behaviour and in the volumetric response of Osorio sand.

For fibre-reinforced sands, the parameters related to the fibres have to be calibrated. This includes the sliding function (f_b) and the grain-fibre pull-out stress (a_{sf} and δ_{sf}), as well as the specific volume of the fibres (υ_c).

The values for these parameters are given in Table 5.4.

Table 5.4 – Fibre parameters for Osorio sand reinforced with fibres

Fibre parameter	Value
f_b	0.1
a_{sf}	5 kPa
δ_{sf}	5°
υ_f	3.0

The values for the fibre parameters are within the range reported in the literature. Diambra (2010) and Diambra et al. (2013) used different types of fibres and reported the following ranges for such parameters: f_b [0.08-0.5], υ_f [2.4-6.9], a_{sf} [4-76 kPa], δ_{sf} [0°-10°].

Both the soil and fibre parameters calibrated above will be employed in the cyclic simulations. Similar methodology has been used in unreinforced sands by Corti (2016) and Corti et al. (2016), who used drained monotonic triaxial tests to calibrate soil parameters and then employed these parameters to simulate cyclic undrained triaxial tests.

The simulations were performed considering two confining pressures (20 kPa and 100 kPa) for two fibre lengths (24 mm and 50 mm). Comparisons with monotonic drained triaxial tests conducted by Festugato (2008) are presented in Figure 5.4 and Figure 5.5.

Figure 5.4 shows that the 24 mm fibre inclusions increased shear strength for different confining stresses. A slight hardening is observed in the simulations of fibre-reinforced specimens. Good agreement is observed for both stress-strain and volumetric behaviour. Despite some divergence in the volumetric response, the model simulations seem to follow a reasonable trend.

Figure 5.5 shows the effect of 50 mm fibres reinforcement. These inclusions caused a much more pronounced hardening behaviour respect to the 24 mm inclusions. The model is able to

capture this important trend between different fibre lengths. This capacity of reproducing such response can be explained by the pull-out stress (equation (3.15)). For fibre stresses higher than the pull-out stress, the incremental fibre contribution is null. For longer fibres, the pull-out stress is higher and hence more difficult to be reached. Thus, the pull-out stress of fibres was probably reached for the 24 mm fibre simulations at some point near ε_a = 3% (for p' = 20 kPa) and ε_a = 6% (for p' = 100 kPa). From these points on, it is clear that there is no fibre stress contribution, as no hardening behaviour is observed. On the other hand, for 50 mm fibre simulations, hardening is observed up to ε_a = 15%. It can be inferred that fibre pull-out did not take place because in such case the hardening behaviour would have ceased for small deformations.

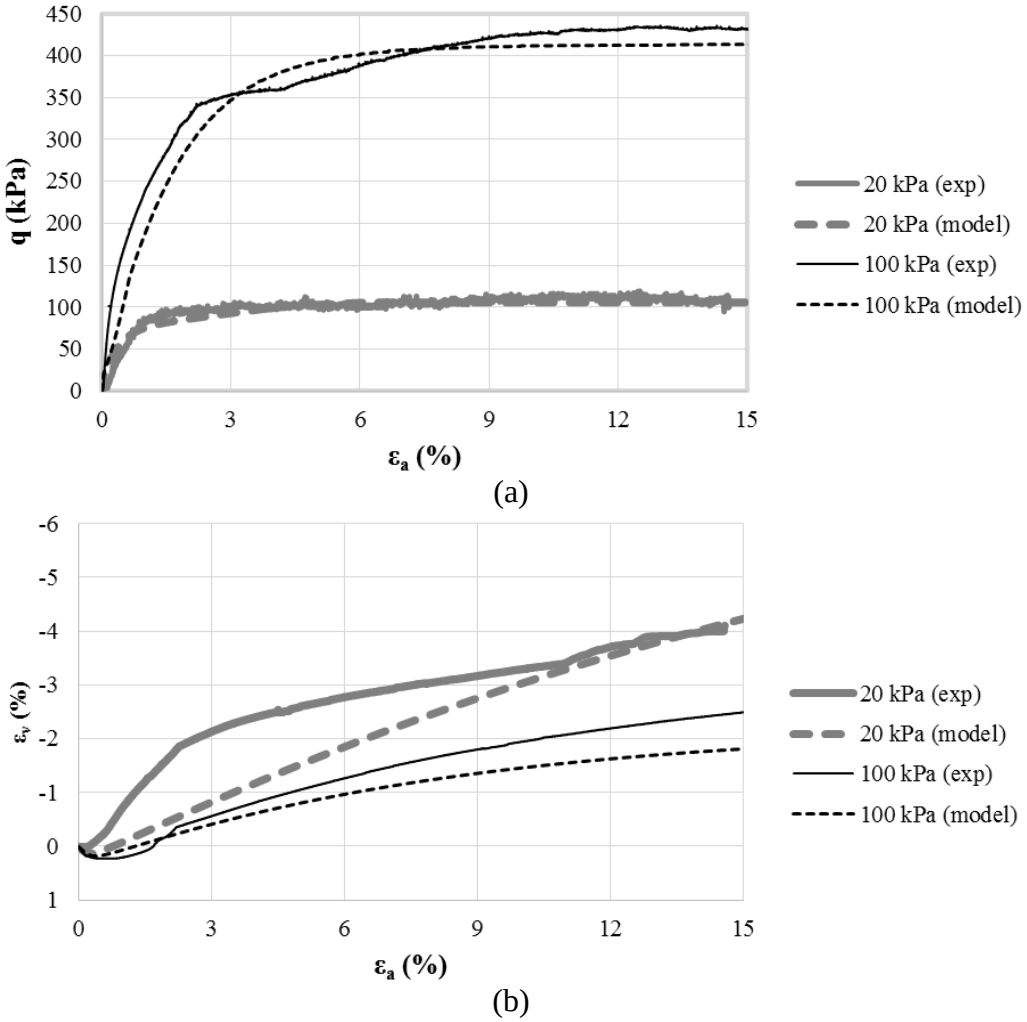

Figure 5.4– Drained triaxial test results and model simulations for Osorio sand reinforced with fibres 24 mm length: (a) stress-strain and (b) volumetric behaviour

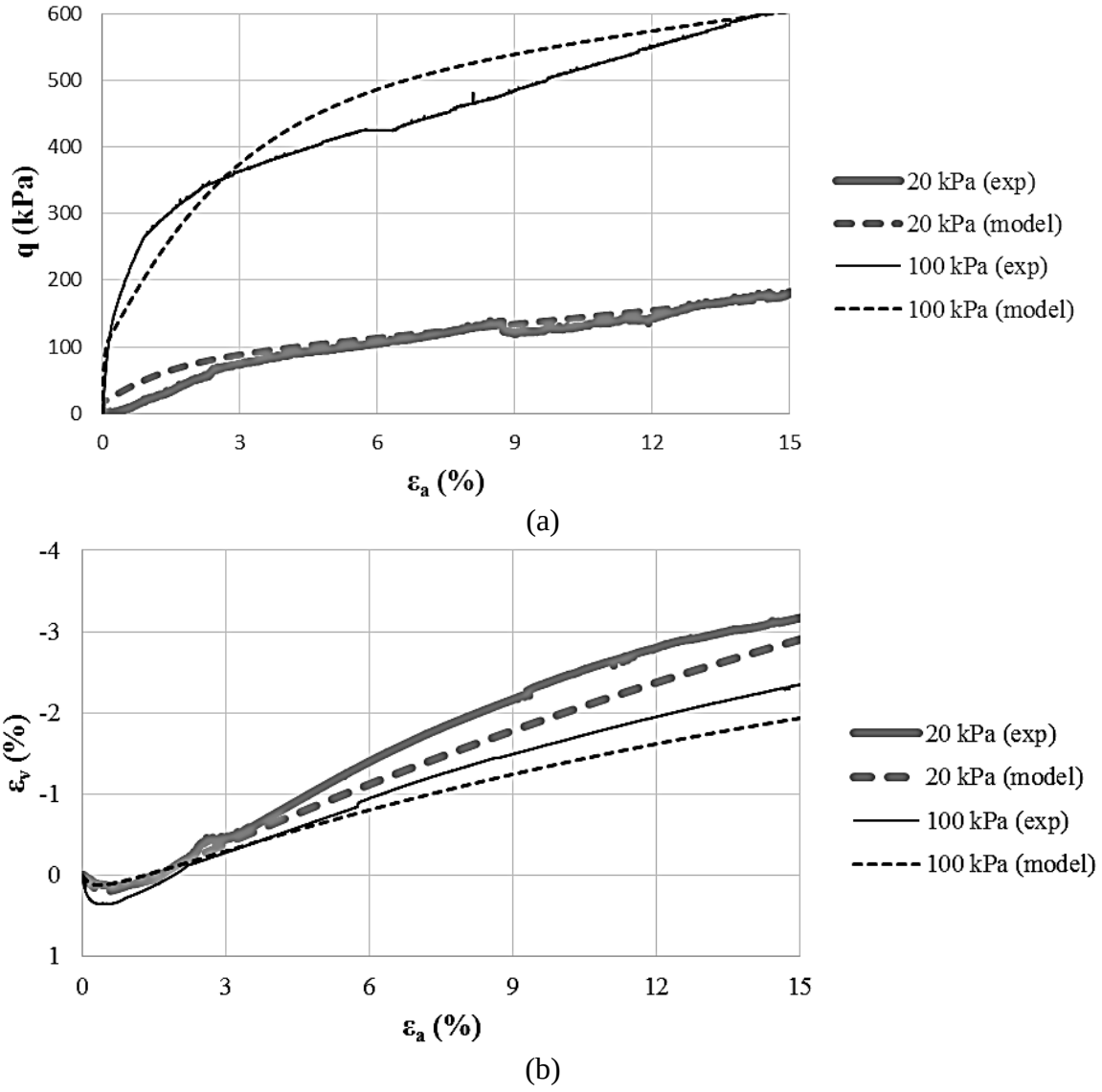

Figure 5.5– Drained triaxial test results and model simulations for Osorio sand reinforced with fibres 50 mm length: (a) stress-strain and (b) volumetric behaviour

From the exposed above, the effectiveness of Severn-Trent model in reproducing triaxial tests with (unreinforced and reinforced) Osorio sand was verified.

5.2.2 Babolsar sand

Salamatpoor and Salamatpoor (2014) carried out monotonic undrained triaxial tests using Babolsar sand with properties almost identical to those reported by Noorzad and Amini (2014). One particular test by Salamatpoor and Salamatpoor (2014) is used herein to calibrate the model parameters. In this test, the relative density of soil was approximately 63% and the initial confining pressure was 300 kPa. The critical state parameters (Γ and λ) for Babolsar sand were not found in the literature. However, most of the characteristics of Babolsar sand are very

similar to those of Osorio sand, e.g. specific gravity of solids, e_{max} and e_{min}, D_{50} and C_u. Moreover, both sands are described as clean quartzitic sands with uniform grading. The particle size distributions are actually very similar (see Figure 5.1 and Figure 5.2). For this reason, critical state parameters Γ and λ for Babolsar sand were assumed to be the same as for Osorio sand. The soil parameters that provide the best fit with triaxial tests are presented in Table 5.5. Figure 5.6 compares triaxial test results and model simulations for Babolsar sand.

Table 5.5 – Severn-Trent model parameters for Babolsar sand

Soil parameter	Value
k_r	1.5
B	0.00005
R	0.1
A	0.75
k_d	1.5
ζ	10

Although the model simulation was not able to capture the post-peak behaviour of the sand, good agreement is verified between model and test results for both stress-strain and *q-p'* response.

Despite the similarities between Osorio and Babolsar sand, a careful reader may notice that the soil parameters for these sands are significantly different. This may be due to differences in testing equipment, test operators, specimen dimensions, mixing and compacting techniques. In fact, Diambra (2010) and Corti (2016) reported very different Severn-Trent parameters for the same Hostun Sand, even though these tests were performed at the same laboratory. Additionally, Diambra (2010) also demonstrated the difference in the response of Hostun sand for different moulding techniques. It is not surprising, though, that soil parameters diverge from Osorio to Babolsar sand.

Unlike for Osorio sand, no triaxial tests with fibre reinforcement was found in the literature for Babolsar sand. Therefore, fibre parameters will be calibrated with cyclic triaxial test for this particular sand.

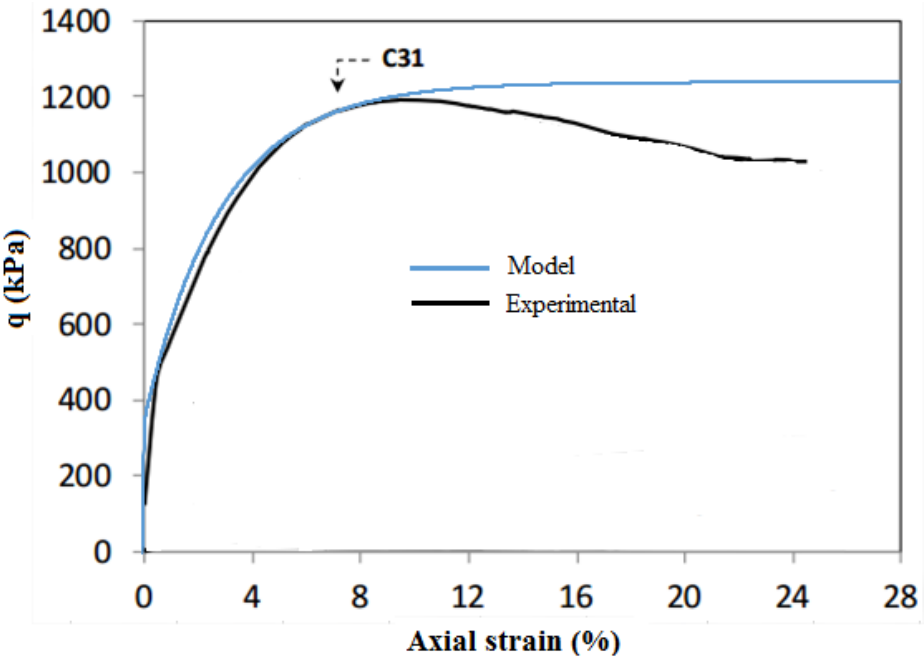

(a)

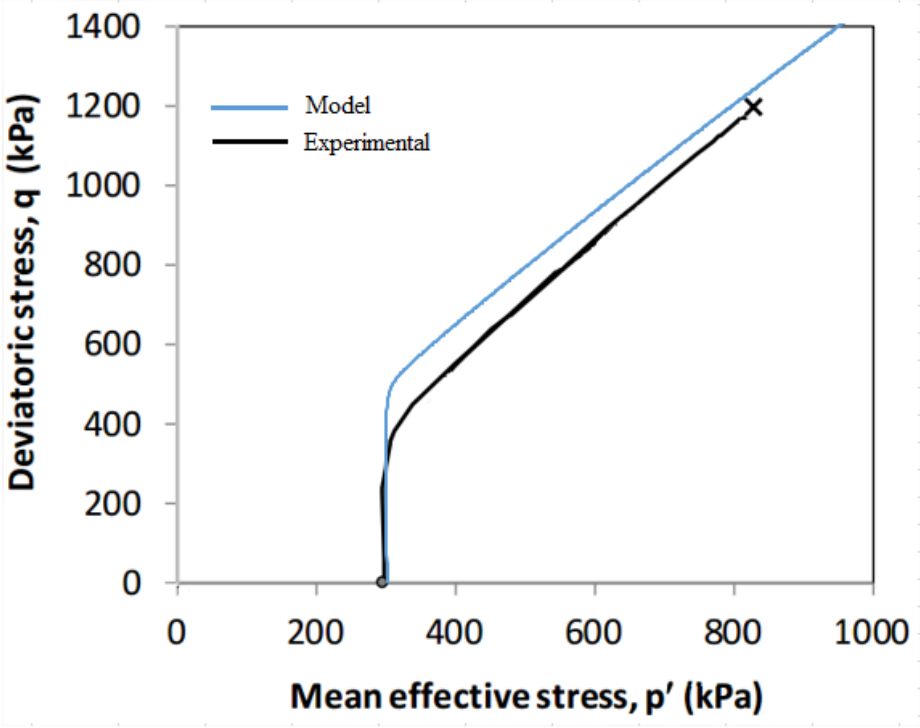

(b)

Figure 5.6– Undrained triaxial test results and model simulations for Babolsar sand: (a) stress-strain and (b) *q-p'*

5.3 CYCLIC TRIAXIAL TESTS

Florez et al. (2016) carried out undrained triaxial tests with Osorio sand and the same 50 mm fibres used by Festugato (2008). The researcher analysed unreinforced and fibre-reinforced specimens under several load amplitudes, confining pressures and void ratios. Moreover,

Noorzad and Amini (2014) analysed the liquefaction resistance of Babolsar sand reinforced with fibres under cyclic loading. The experimental results from these studies are compared with model simulations as follows.

5.3.1 Osorio sand

Florez et al. (2016) performed undrained triaxial tests under repeated loading for relative density index I_D of 50% (e_0 = 0.75). Using the same parameters as for the monotonic drained tests (Table 5.4), the model simulations are compared to the triaxial test results: *q-p** (Figure 5.7 for unreinforced sand and Figure 5.9 for reinforced sand) and stress-strain (Figure 5.8 for unreinforced sand and Figure 5.10 for reinforced sand).

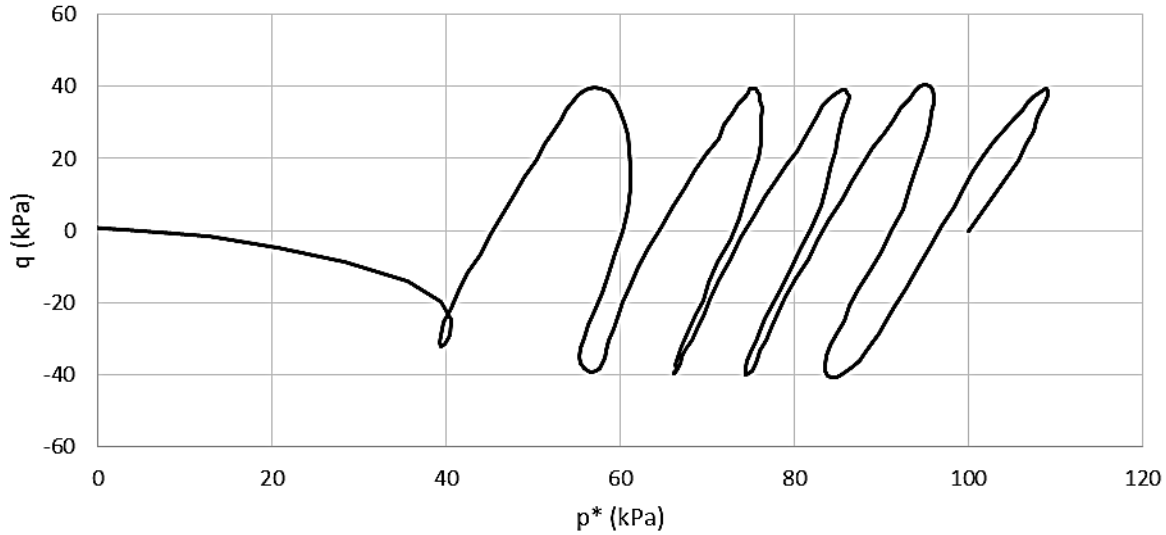

(a)

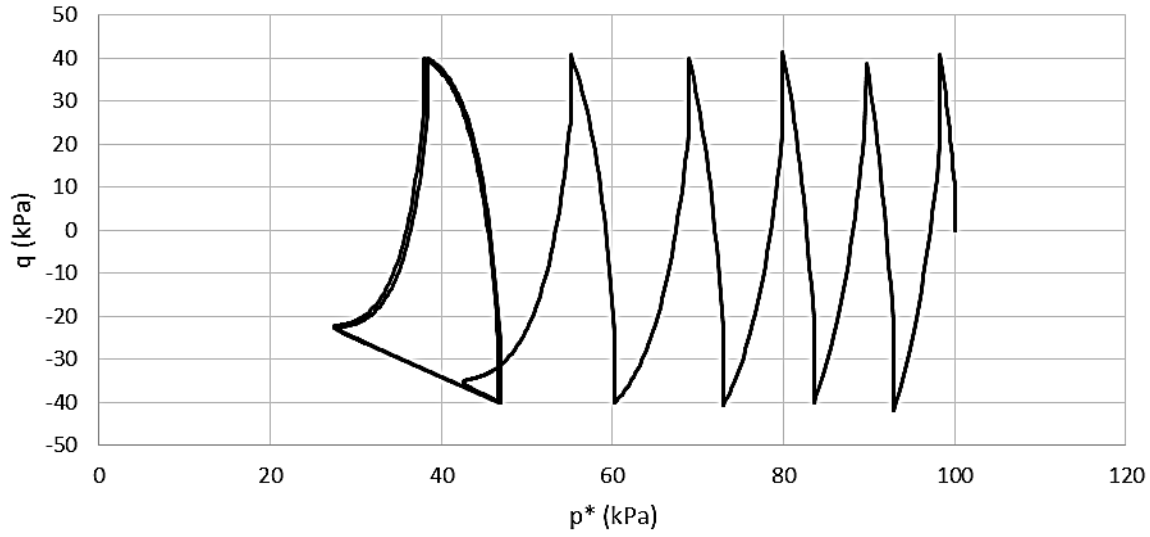

(b)

Figure 5.7 – Comparison between *q-p** cyclic behaviour for (a) undrained triaxial test and (b) model simulation for unreinforced Osorio sand (w_f = 0%)

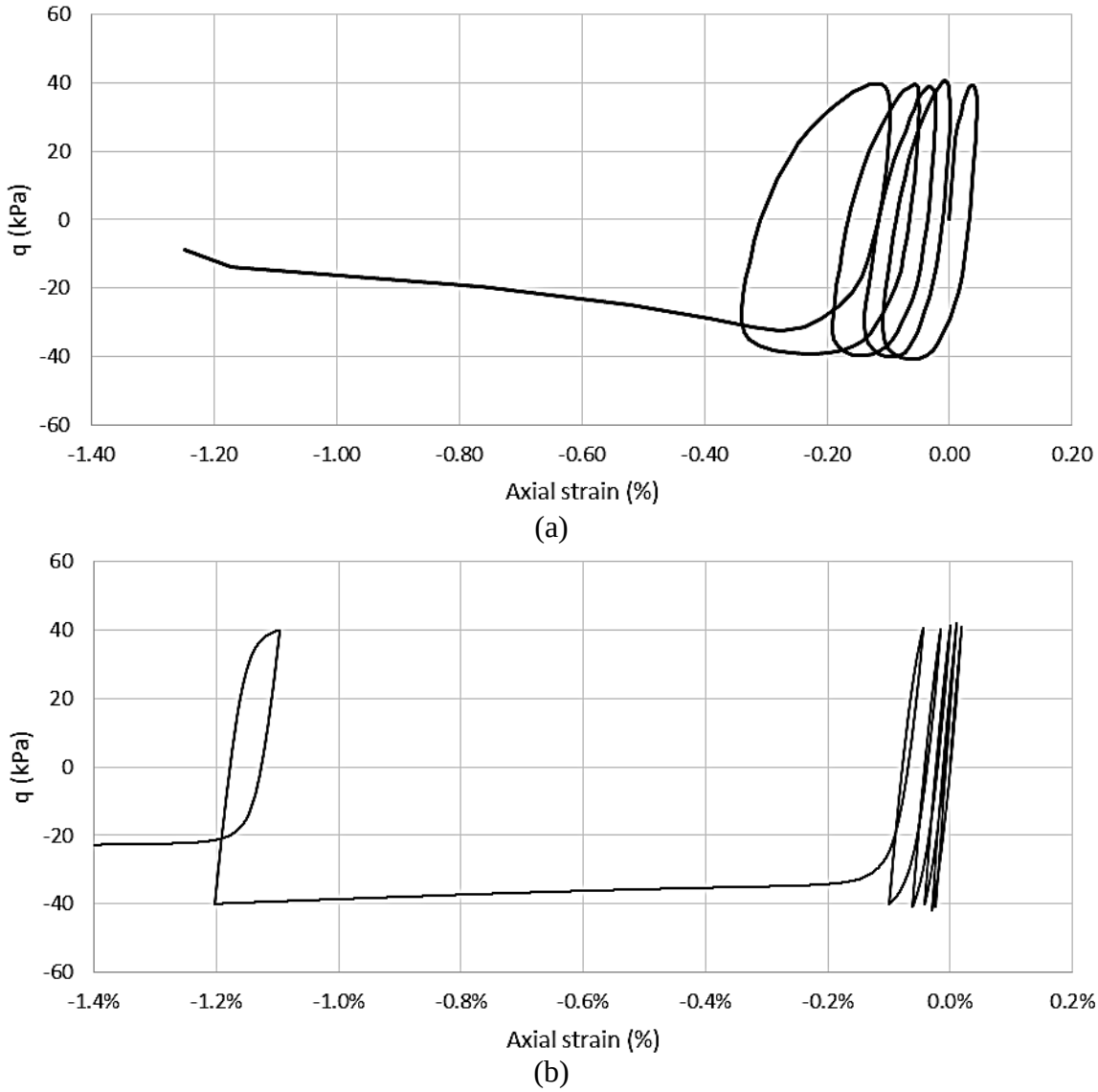

Figure 5.8 – Comparison between stress-strain cyclic behaviour for (a) undrained triaxial test and (b) model simulation for unreinforced Osorio sand (w_f = 0%)

It is worth noting that under this relative density index liquefaction is unlikely to occur. Bedin et al. (2012) showed that the liquefaction phenomena only happens for soils whose state parameter is positive. For medium-dense and dense sands the state parameter is negative, hence liquefaction does not occur for such soils. In this case, the two criteria for liquefaction proposed by Ishihara (1996) will be used as a failure criteria for cyclic tests. This assumption has been employed by Florez et al. (2016).

From Figure 5.7, it is clear that the model simulations are effective in reproducing soil cyclic behaviour for the first cycles. Both figures show that the effective mean stress approaches zero during the application of stress cycles. Despite some difference in the form of the stress paths,

there seems to be good agreement between the graphs in terms of amplitude of the cycles and the decrease rate in the mean effective stress p^* for each cycle. For example, from p^* = 100 kPa to p^* = 60 kPa, both the test results and the model developed 4 cycles of loading-unloading. This shows that the pore pressure build-up can be reasonably captured by the model. On the other hand, as the stress path approaches p^* = 0 (1st failure criterion), the model behaviour looks different from the experimental results. The triaxial test response shows that when the stress path reaches p^* = 40 kPa it goes straight to p^* = 0, evidencing the occurrence of failure. However, the model simulation presents a hysteretic loop after reaching p^* = 40 kPa. Hence, it seems that the model is not able to capture soil response when it approaches a failure state. Nevertheless, it is worth noticing that in both experimental and model results the stress path behaviour changes its pattern when it reaches the same value of p^* = 40 kPa. This change indicates the onset of soil instability that leads to failure. This point was previously observed by Noorzad and Amini (2014). Therefore, despite some visual differences in the plots for the final cycles, the model seems to properly indicate the starting point of such soil instability.

The very same behaviour is verified for fibre-reinforced sand in Figure 5.9. Similar cyclic behaviour is observed from p^* = 100 to approximately 45 kPa. From that point on, the experimental stress path approaches p^* = 0 very rapidly whereas the model simulation goes into a hysteretic loop. Nevertheless, it is possible to see that the model adequately captures the influence of fibre inclusions. While for the unreinforced sand four cycles developed from p^* = 100 kPa to p^* = 60 kPa, for instance, almost seven cycles developed in the same interval for fibre-reinforced sand. Again, the model perfectly captured the number of cycles developed until a certain point from which the soil (and the model) exhibits instability.

Concerning the stress-strain behaviour (Figure 5.8 for unreinforced sand and Figure 5.10 for fibre-reinforce sand) it is clear that the model simulations differ from the triaxial test results, especially for the reinforced sand (Figure 5.10). This discrepancy has also been reported by Corti (2016), who affirmed that continuous cycling induced a progressive soil stiffening and hence prevented the model to accurately reproduce stress-strain behaviour. In fact, the referred author also observed the same hysteretic loop for the stress paths reported herein. A damage mechanism in the strength surface was proposed by Corti (2016) to get over this inaccuracy. Despite mathematically complex, such mechanism allows the model to effectively capture soil behaviour close to failure.

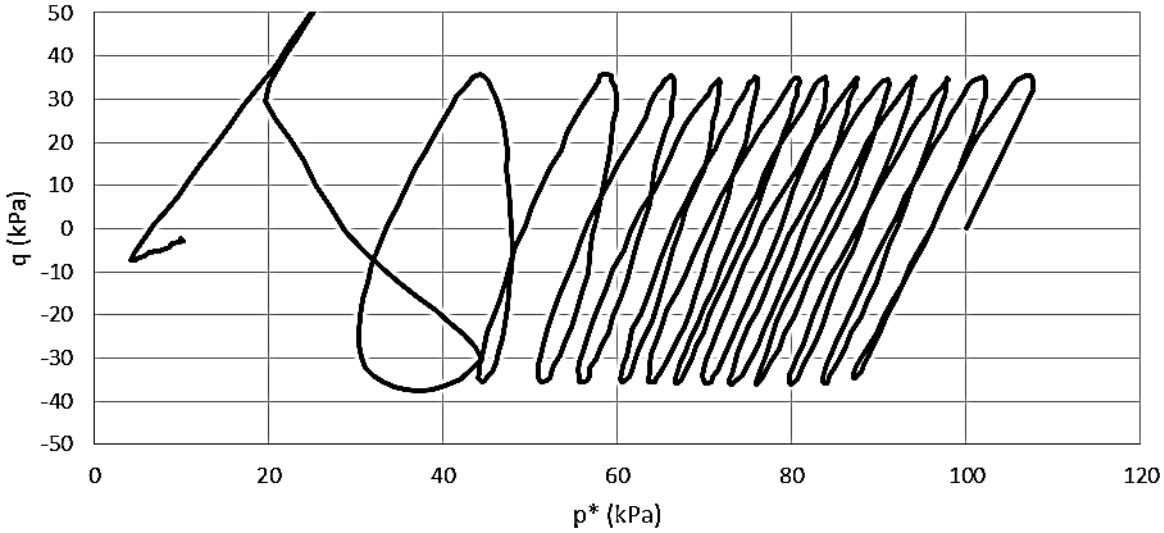

(a)

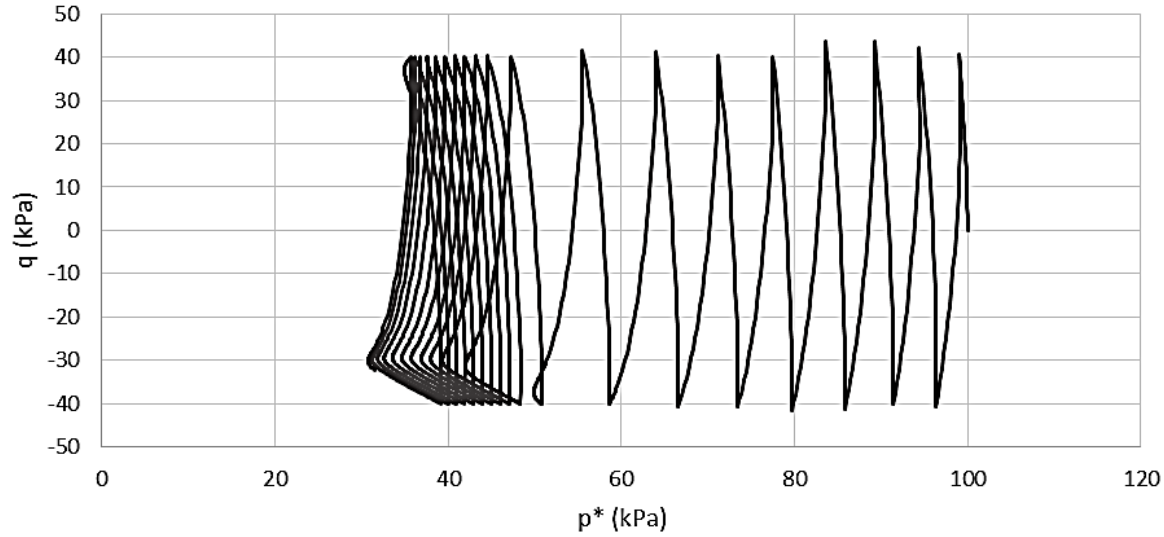

(b)

Figure 5.9 – Comparison between *q-p** cyclic behaviour for (a) undrained triaxial test and (b) model simulation for fibre-reinforced Osorio sand (w_f = 0.5%)

Florez et al. (2016) also analysed the cyclic stress ratio (CSR) in terms of the number of cycles required to cause failure. In undrained cyclic triaxial tests, cyclic stress ratio is defined in equation (5.1).

$$\mathrm{CSR} = \frac{\sigma'_d}{2\,\sigma'_c} \tag{5.1}$$

where σ_d' is the deviatoric stress (half the amplitude of cyclic load) and σ_c' is the initial confining stress.

As mentioned in Chapter 1, it is usually assumed that failure – or liquefaction – state occurred when at least one of Ishihara's criteria was satisfied: 5% axial strain or 100% pore pressure build-up ($p^* = 0$). However, it has been shown in the present study that the proposed model is not able to capture the stress path patterns when it approaches $p^* = 0$. For this reason, it was assumed herein that the failure occurs at the instability point observed in Figure 5.7 (b) and in Figure 5.9 (b), as it was shown that in actual tests the specimen fails after reaching such point. Figure 5.11 shows the resistance curves of Osorio sand in terms of the relationship between the cyclic stress ratio and corresponding number of cycles required to cause failure.

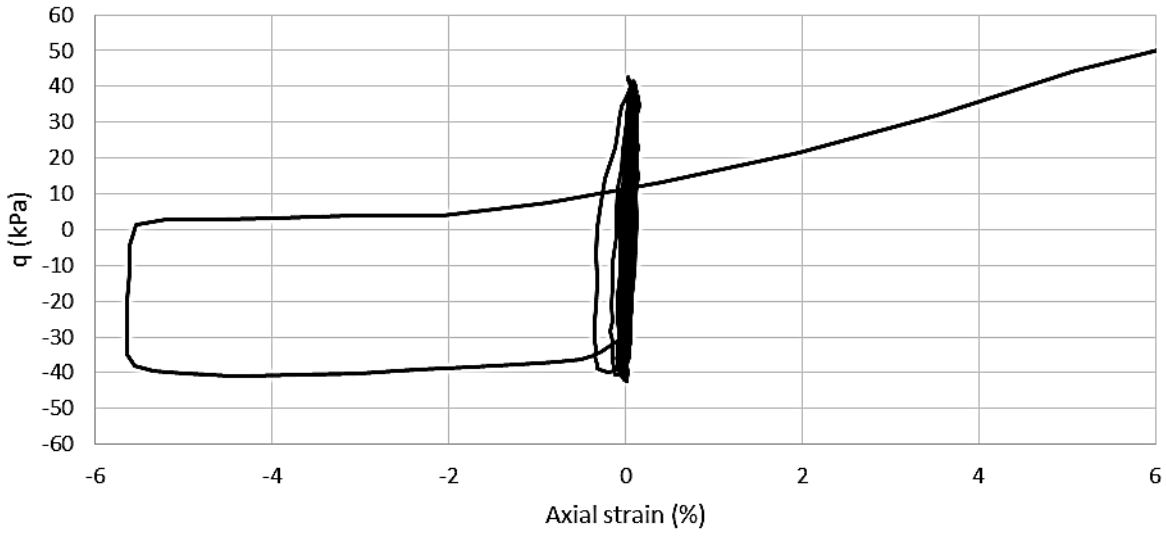

(a)

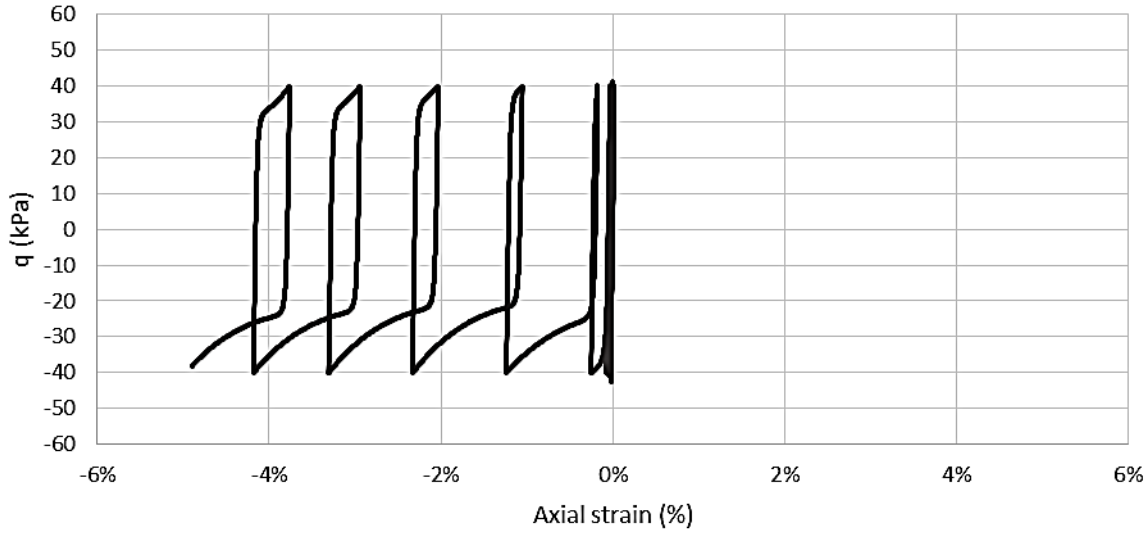

(b)

Figure 5.10 – Comparison between stress-strain cyclic behaviour for (a) undrained triaxial test and (b) model simulation for fibre-reinforced Osorio sand ($w_f = 0.5\%$)

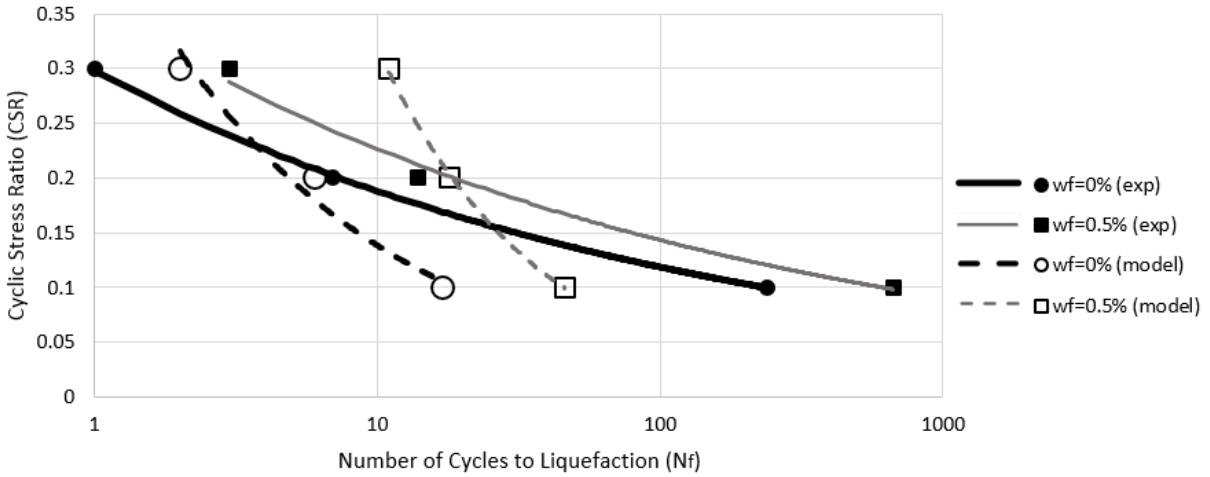

Figure 5.11 – Comparison between the cyclic stress ratio (CSR) for undrained triaxial test and model simulations for Osorio sand

It is possible to observe that the curves do not agree well. The experimental curves exhibit a larger difference in the number of cycles between tests with *CSR* = 0.3 and tests with *CSR* = 0.1. N_f goes from 1 to 240 for unreinforced specimens and from 3 to 666 to fibre-reinforced specimens. On the other hand, for model simulations, N_f varies between 6 and 17 to unreinforced sand and between 11 and 46 to fibre-reinforced sand. This divergence might be due to the density of the sand (I_D = 50%). As the model relates both strength and stiffness to the state parameter (and hence to the proximity between the stress state and the CSL), it might not be able to capture the response of soils whose state is below the critical state line. This occurs because during the application of stress cycles, the effective mean pressure *p** decreases and for denser soils the stress state moves away from the critical state line (Figure 5.12). Accordingly, such stress will never approach the CSL. On the contrary, denser sands that are above the critical state line will approach it during the application of stress cycles and hence the model will be able to capture failure more accurately. Therefore, the proposed model is more likely to work in looser sands, for which the stress state is above the critical state line. To confirm this hypothesis, further simulations in looser sands will be performed as follows.

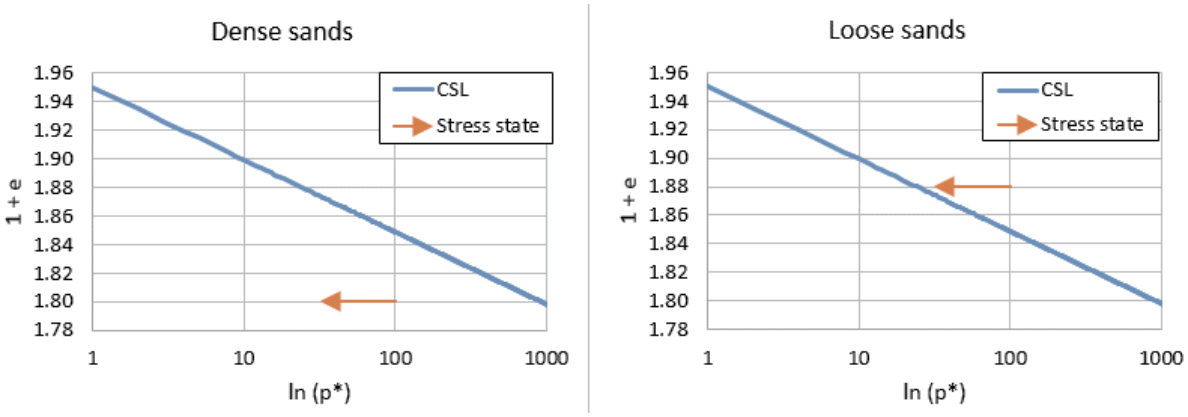

Figure 5.12 – Stress states and critical state line for dense and loose sands

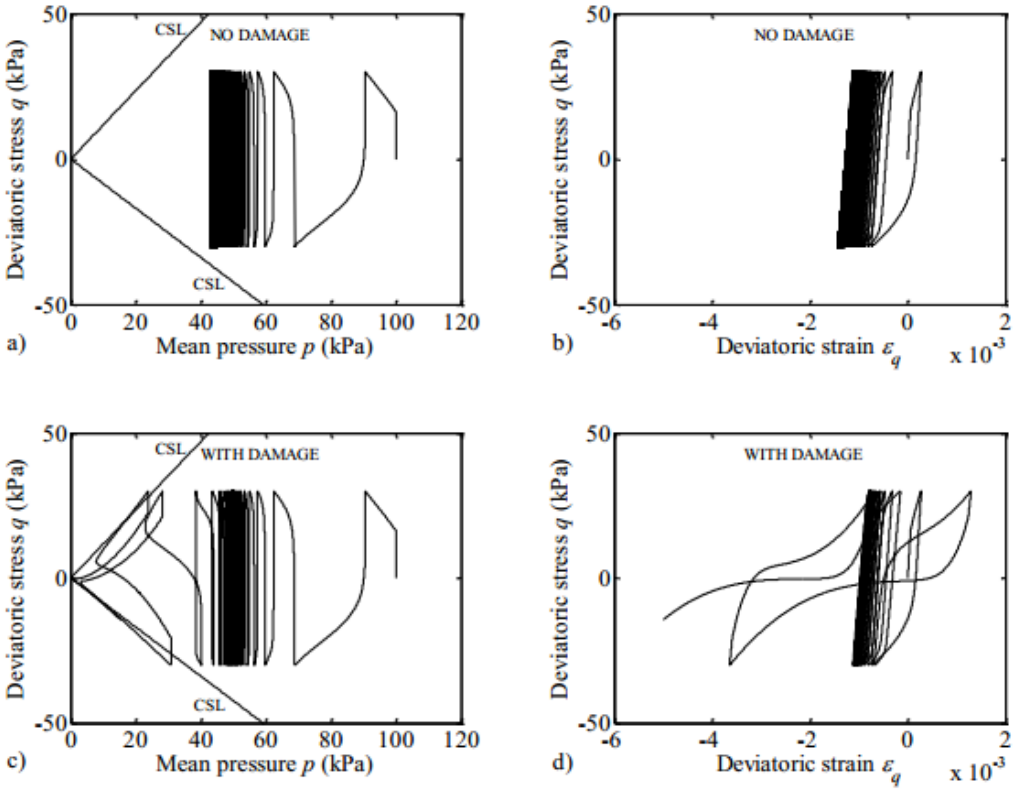

Figure 5.13 – Model performances proposed by Corti (2016) without the damage mechanism implemented a) *q-p*; b) *q-*ε_q and accounting for the damage mechanism c) *q-p*; d) *q-*ε_q (CORTI, 2016)

5.3.2 Babolsar sand

Undrained triaxial tests under cyclic loads were carried out by Noorzad and Amini (2014). These tests are used herein to check the compatibility with model results for cyclic loading conditions. Since no previous monotonic triaxial tests on fibre-reinforced Babolsar were found, fibre parameters were calibrated with cyclic tests. Fibre parameters are displayed in Table 5.6.

Table 5.6 – Fibre parameters for Babolsar sand reinforced with fibres

Fibre parameter	Value
f_b	0.6
a_{sf}	0 kPa
δ_{sf}	30°
υ_f	3.3

Firstly, the *q-p** and stress-strain responses are analysed. The triaxial tests were performed for specimens with relative density of 20%, confining pressure of 200 kPa, fibre length of 12 mm and fibre contents of 0%, 0.5% and 1%. Figure 5.14, Figure 5.15 and Figure 5.16 show the comparison between test results and model simulations for Babolsar sand with fibre contents of 0%, 0.5% and 1%, respectively.

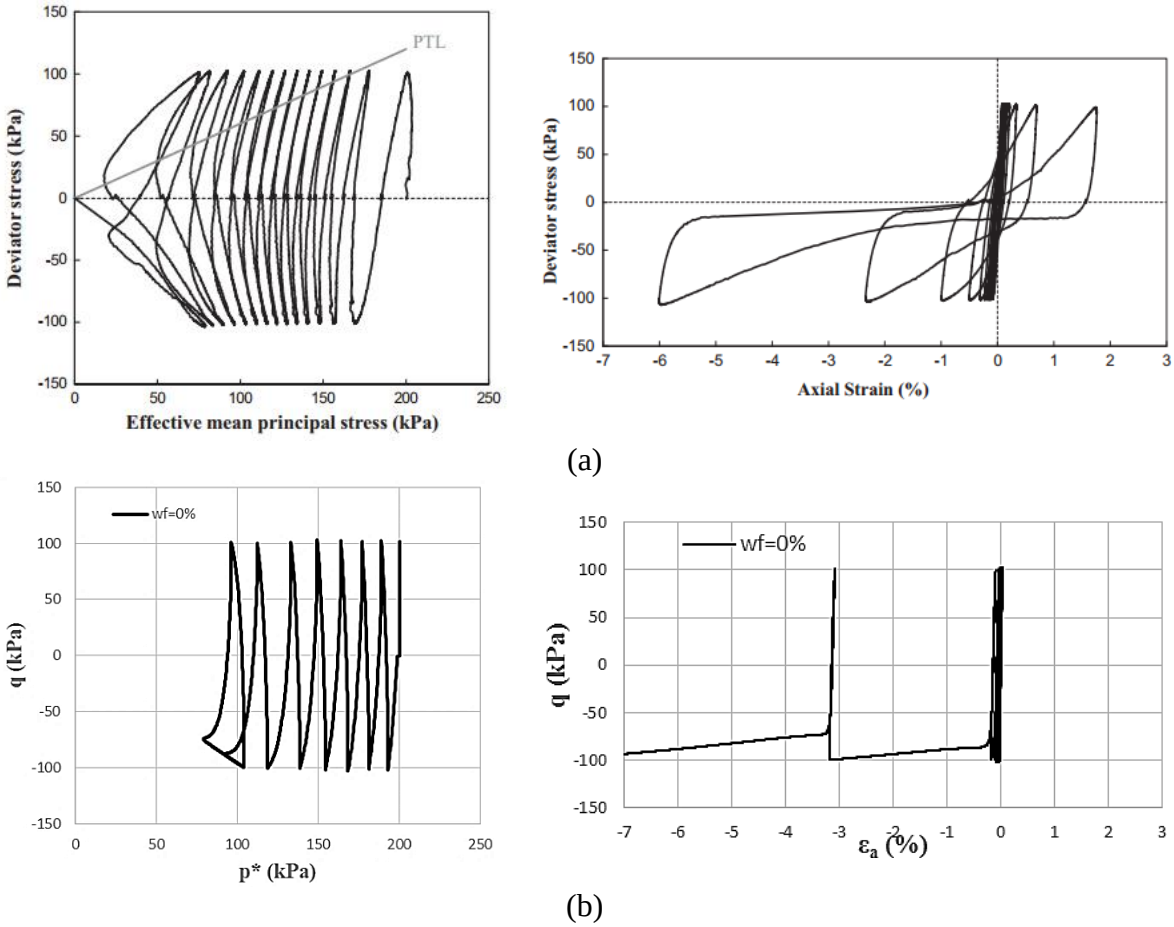

Figure 5.14 – Comparison between *q-p** and stress-strain behaviour for (a) undrained triaxial test and (b) model simulations for unreinforced Babolsar sand (w_f = 0%)

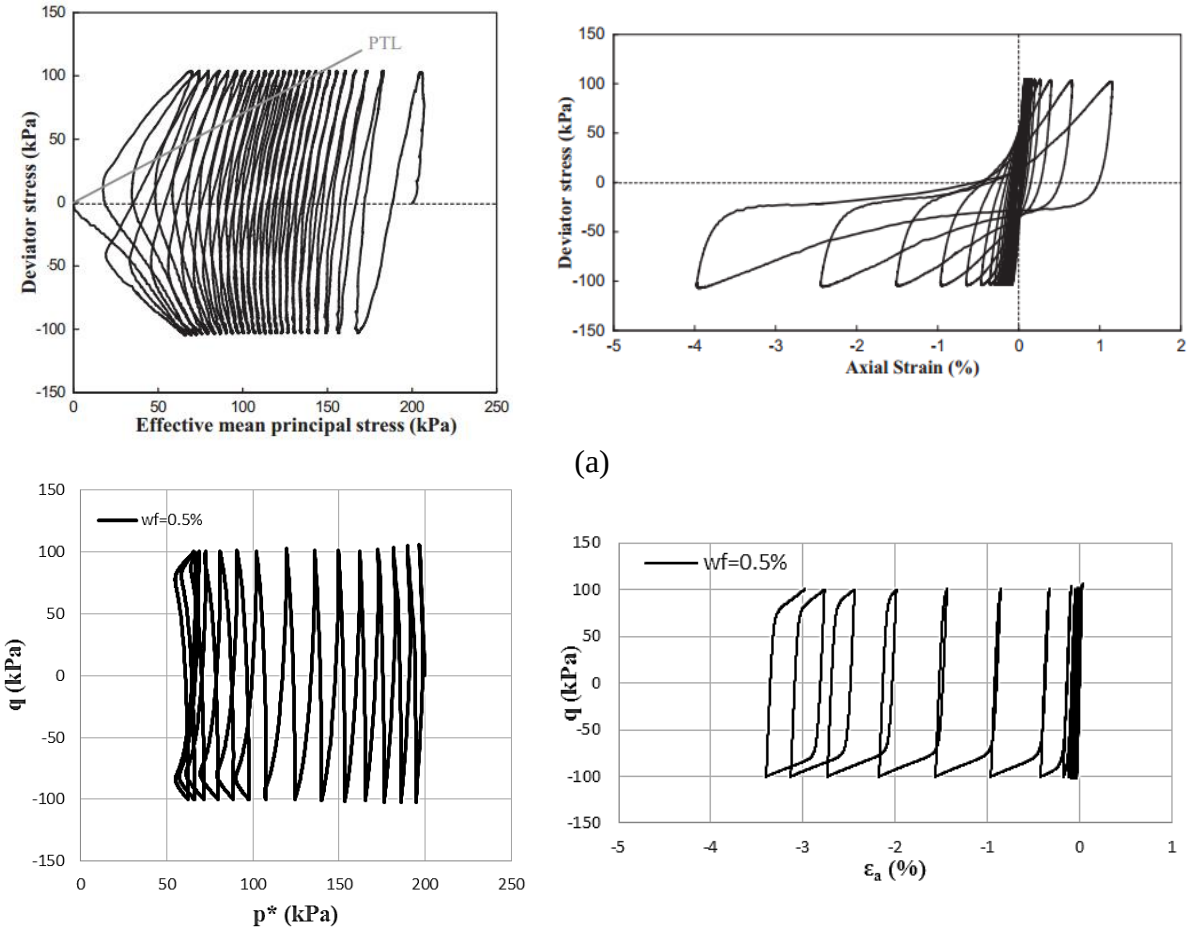

Figure 5.15 – Comparison between *q*-*p** and stress-strain behaviour for (a) undrained triaxial test and (b) model simulations for fibre-reinforced Babolsar sand (w_f = 0.5%)

As for the Babolsar sand the relative density index I_D is 20%, the state parameter is positive, i.e. the void ratio is higher than those on the CSL. For this reason, liquefaction is likely to occur and hence the criteria for liquefaction proposed by Ishihara (1996) apply herein.

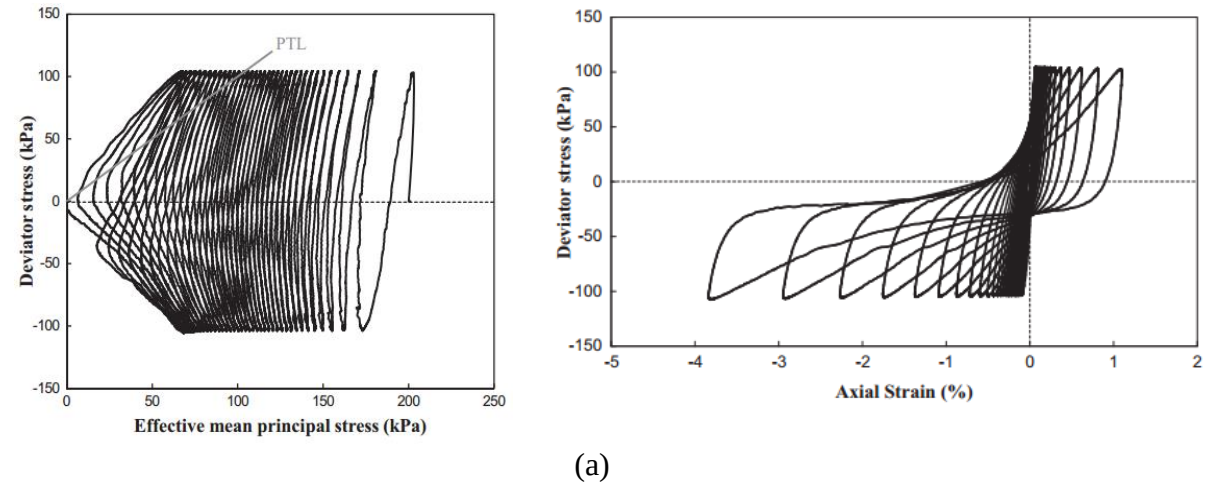

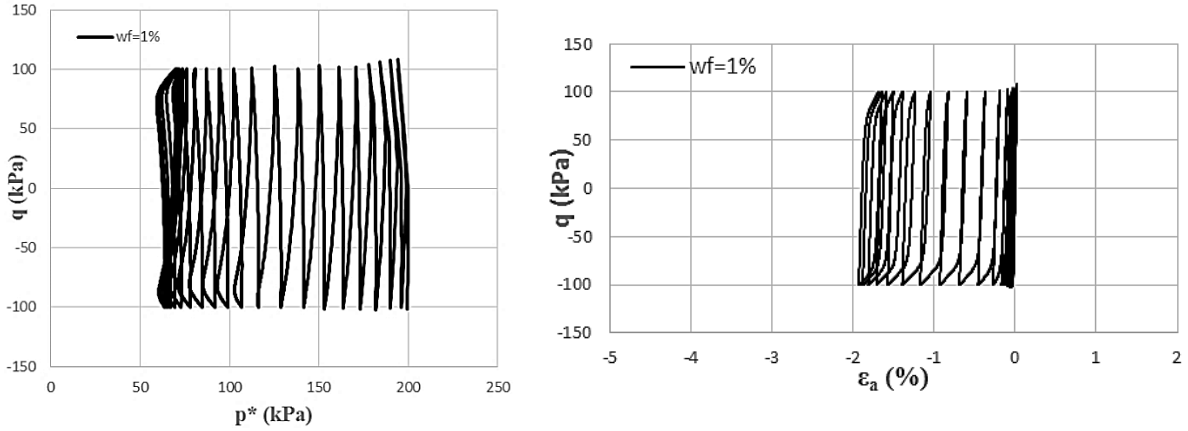

(b)

Figure 5.16 – Comparison between *q*-*p** and stress-strain behaviour for (a) undrained triaxial test and (b) model simulations for fibre-reinforced Babolsar sand (w_f = 1.0%)

It is clear that, despite some visual divergences (especially for the stress-strain behaviour) the model simulations capture the three main trends of the triaxial tests:

a) the addition of fibres reduces axial strains;

b) the addition of fibres delays the occurrence of liquefaction; and

c) the mean stress from which soil instability leads to liquefaction ($p^* = 0$) is approximately the same where the hysteretic loop begins in the model simulations.

The liquefaction resistance for different confining pressures and stress amplitudes has also been assessed for Babolsar sand. Figure 5.17 depicts the cyclic stress ratio in terms of N_f for this soil.

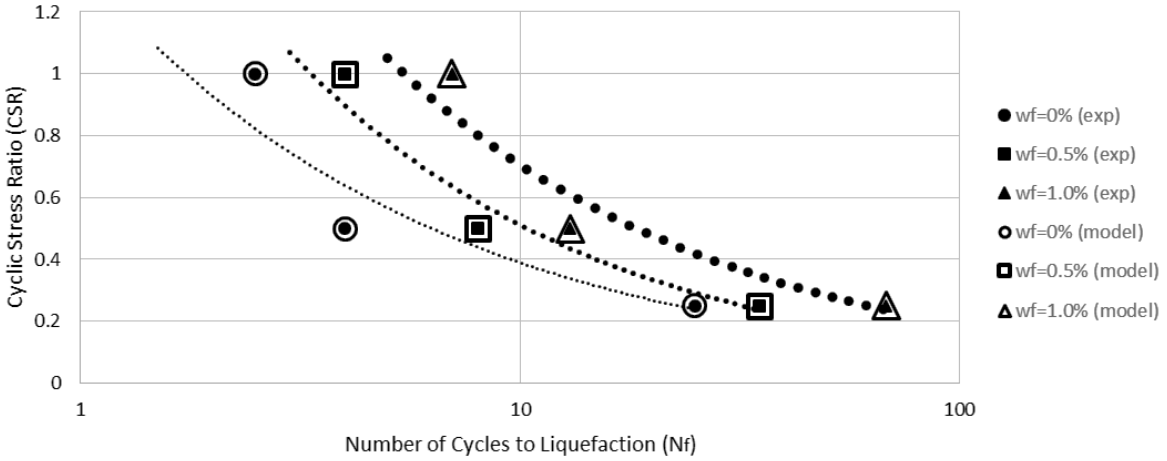

Figure 5.17 – Comparison between the cyclic stress ratio (CSR) for undrained triaxial test and model simulations for Babolsar sand

The accuracy between experimental and model results is almost perfect. The model captures well the number of cycles to liquefaction for different cyclic stress ratios and fibre contents. These findings confirm that the model is more effective in reproducing the response of looser soils rather than denser ones.

6 CONCLUDING REMARKS

First of all, it is worth emphasizing the originality of the present research. To the author's knowledge, for the first time a model for fibre-reinforce sands under cyclic loads is proposed. For this reason, it should be seen as a first attempt to model this type of soils under such conditions and any contribution is of great value.

6.1 SUMMARY OF MAIN CONCLUSIONS

The main conclusions of the present research are presented below:

a) The Severn-Trent model seems able to reproduce the behaviour of fibre-reinforced sands under cyclic loads. Even though results do not visually agree very well, the trends are consistent with triaxial test results. An adjustment factor was added to two Severn-Trent parameters (*B* and *A*) to account for the change in interparticle contact after fibres are added to sand.

b) The model captures important key aspects of fibre-reinforced soils, such as: compatibility between radial strain and strain in the horizontal fibres when perfect sand-fibre bond is assumed and agreement between stresses in fibres with symmetric orientations ($\pm$20°, $\pm$40°, $\pm$60° and $\pm$80°).

c) The effect of fibre inclusions in model simulations is consistent with what has been reported in the literature: the inclusions reduce axial strains and reduce pore pressure build-up, delaying liquefaction.

d) The parametric analysis has shown that, from model simulations, it is difficult to assess whether certain fibre parameters, such as E_f, f_b, l_f and υ_f, prevent liquefaction or hasten the occurrence of this phenomenon. That happens because on the one hand, increasing these parameters reduces axial strain, but on the other hand, they increase pore pressure generation and hence anticipate pore pressure build-up. This brings up a contradiction between the first and the second Ishihara's criterion. The lack of experimental studies on this matter impedes us to state whether stiffer and longer fibres, for example, are effective in preventing liquefaction.

e) The parametric analysis of soil parameters has shown that k_r, B, A and k_d are the most important parameters affecting the cyclic behaviour of fibre-reinforced sands.

f) The proposed model was calibrated with monotonic triaxial tests with Osorio and Babolsar sand. Good agreement was found for stress path, stress-strain and volumetric behaviour.

g) Good agreement is observed between the stress paths from triaxial test results and model simulations for both Osorio and Babolsar sand. The development of stress cycles is well captured until a certain stress state, from which the actual stress paths go straight to $p^* = 0$ and the model stress paths go into a hysteretic loop. This point is called "instability point" which further leads to failure or liquefaction. This hysteretic loop has also been reported by Corti (2016), who suggested a damage mechanism in the strength surface to properly reproduce soil behaviour close to failure.

h) Stress-strain pattern from model simulations diverges from actual test results. However, an important trend is captured by model simulations: the decrease in axial strains for fibre-reinforced sands respect to unreinforced sands.

i) The liquefaction resistance curves from model simulations for Osorio sand do not show good agreement with actual curves from experimental results. This might be due to the high density of sand, as the proposed model was developed for initial stress states laying on the "loose side" of the critical state line. The model relates both strength and stiffness to the state parameter (and hence to the distance to the critical state line). Consequently, sands on the "dense side", which do not approach the CSL, do not have its behaviour close to failure well reproduced by the proposed model. The number of cycles to reach liquefaction then diverges between model and actual test results.

j) The liquefaction resistance curves from model simulations for Babolsar sand show perfect agreement with actual experimental curves. The better performance of Babolsar sand can be attributed to the lower relative density if compared to Osorio sand. The high void ratio of Babolsar sand placed it on the loose side of the critical state line and, as a consequence of that, the

approximation to CSL with the development of stress cycles allowed the model to successfully capture the number of cycles to reach liquefaction.

6.2 SUGGESTION FOR FURTHER RESEARCH

It is clear that the model successfully captures the general trends of fibre-reinforced sands under cyclic loads, but it fails to capture soil behaviour close to failure. Corti (2016) developed the Memory Surface Hardening model, which incorporated a damage mechanism to strength surface. This model was shown to capture soil behaviour when it approaches liquefaction. Therefore, employing that model as the constitutive model for the matrix (instead of Severn-Trent) seems promising and may be an encouraging trial for further research.

Concerning experimental studies, cyclic undrained triaxial tests with fibre-reinforced sands could be conducted with fibres of different elastic modulus, different roughness (in order to account for different sliding functions) and different fibre lengths. This would enable researchers to understand the trade-off between reducing axial strains and pore water pressures, which has been reported in the parametric analysis.

REFERENCES

AHMAD, F.; BATENI, F.; AZMI, M. Performance evaluation of silty sand reinforced with fibres. **Geotextiles and Geomembranes**, v. 28, p. 93-99, 2010.

BEDIN, J.; SCHNAID, F.; VIANA DA FONSECA, A.; COSTA FILHO, L. M. Gold tailings liquefaction under critical state soil mechanics. **Géotechnique**, v. 62, n. 3, p. 263-267, 2012.

BEEN, K.; JEFFERIES, M. G. A state parameter for sands. **Géotechnique**, v. 35, n. 2, p. 99-112, 1985.

BRITTO, A. M.; GUNN, M. J. **Critical State Soil Mechanics via Finite Elements**. Chichester, England: Ellis Horwood Limited, 1987.

BUDINSKI, K. G. **Engineering Materials: Properties and Selection**. 5. ed. New Jersey: Prentice Hall International, 1996.

CASAGRANDE, M. D. T. **Estudo do comportamento de um solo reforçado com fibras de polipropileno visando o uso como base de fundações superficiais**. 2001. 94 p. MSc Dissertation (Master of Engineering) – Programa de Pós-Graduação em Engenharia Civil, PPGEC/UFRGS, 2001.

CASAGRANDE, M. D. T. **Comportamento de solos reforçados com fibras submetidos a grandes deformações**. 2005. 243 p. PhD Thesis (Doctor of Engineering) – Programa de Pós-Graduação em Engenharia Civil, PPGEC/UFRGS, 2005.

CONSOLI, N. C.; PRIETTO, P. D. M.; ULBRICH, L. A. Influence of fiber and cement addition on behavior of sandy soil. **Journal of Geotechnical and Geoenvironmental Engineering**, v. 124, n. 12, p. 1211-1214, 1998.

CONSOLI, N. C.; VENDRUSCOLO, M. A.; PRIETTO, P. D. M. Behavior of plate load tests on soil layers improved with cement and fiber. **Journal of Geotechnical and Geoenvironmental Engineering**, v. 129, n. 1, p. 96-101, 2003.

CONSOLI, N. C.; CASAGRANDE, M. D. T.; COOP, M. R. Effect of fiber reinforcement on the isotropic compression behaviour of sand. **Journal of Geotechnical and Geoenvironmental Engineering**, v. 131, n. 11, p. 1434-1436, 2005.

CONSOLI, N. C.; CASAGRANDE, M. D. T.; COOP, M. R. Performance of a fibre-reinforced sand at large shear strains. **Géotechnique**, v. 57, n. 9, p. 751-756, 2007.

CONSOLI, N. C.; VENDRUSCOLO, M. A.; FONINI, A.; DALLA ROSA, F. Fiber reinforcement effects on sand considering a wide cementation range. **Geotextiles and Geomembranes**, v. 27, n. 3, p. 196-203, 2009b.

CONSOLI, N. C.; FESTUGATO, L.; HEINECK, K. S. Strain-hardening behaviour of fibre-reinforced sand in view of filament geometry. **Geosynthetics International**, v. 16, n. 2, p. 109-115, 2009a.

CORTI, R. **Hardening memory surface constitutive model for granular soils under cyclic loading conditions**. 2016. 238 p. PhD thesis (Doctor of Philosophy in the Faculty of Engineering) – Department of Civil Engineering, University of Bristol, Bristol, UK, 2016.

CUNDALL, P. A. A computer model for simulating progressive, large scale movements in blocky rock systems. In: SYMPOSIUM OF THE INTERNATIONAL SOCIETY OF ROCK MECHANICS, 1971, Nancy 2. **Proceedings**, 1971, pp. 129-136.

CUNDALL, P. A.; STRACK, O. D. A discrete numerical model for granular assemblies. **Géotechnique**, v. 21, n. 1, p. 47-65, 1979.

CURCIO, D. S. **Comportamento hidromecânico de compósito solo-fibra**. 2008. 169 p. PhD thesis (Doctor in Civil Engineering) – COPPE, Federal University of Rio de Janeiro (UFRJ), Rio de Janeiro, Brazil, 2008.

DAVIS, R. O.; SELVADURAI, A. P. S. **Plasticity and Geomechanics**. Cambridge, UK: Cambridge University Press, 2002.

DI PRISCO, C.; NOVA, R. A constitutive model for soil reinforced by continuous threads. **Geotextiles and Geomembranes**, v. 12, n. 2, p. 161-178, 1993.

DIAMBRA, A. **Fibre reinforced sands: experiments and constitutive modelling**. 2010. 266 p. PhD Thesis (Doctor of Philosophy) – Faculty of Engineering, Department of Civil Engineering, University of Bristol, UK, 2010.

DIAMBRA, A.; IBRAIM, E. Modelling of fibre-cohesive soil mixtures. **Acta Geotechnica**, v. 9, n. 6, p. 1029-1043, 2014.

DIAMBRA, A.; IBRAIM, E.; MUIR WOOD, D.; RUSSEL, A. R. Fibre reinforced sands: experiments and modelling. **Geotextiles and Geomembranes**, v. 28, p. 238-250, 2010.

DIAMBRA, A.; IBRAIM, E.; RUSSEL, A. R.; MUIR WOOD, D. Modelling the undrained response of fibre reinforced sands. **Soils and Foundations**, v. 51, n. 4, p. 625-636, 2011.

DIAMBRA, A.; IBRAIM, E.; RUSSEL, A. R.; MUIR WOOD, D. Fibre reinforced sands: from experiments to modelling and beyond. **International Journal for Numerical and Analytical Methods in Geomechanics**, v. 37, p. 2427-2455, 2013.

DIAMBRA, A.; RUSSEL, A. R.; IBRAIM, E.; MUIR WOOD, D. Determination of fibre orientation distribution in reinforced sands. **Géotechnique**, v. 57, n. 7, p. 623-628, 2007.

DING, D.; HARGROVE, S. K. Nonlinear stress-strain relationship of soil reinforced with flexible geofibers. **Journal of Geotechnical & Geoenvironmental. Engineering**, v. 132, n. 6, p. 791-794, 2006.

DOS SANTOS, A. P. S.; CONSOLI, N. C. C.; BAUDET, B. A. The mechanics of fibre-reinforced sand. **Géotechnique**, v. 60, n. 10, p. 791-799, 2010.

ESCRIBANO, D. **Evolution of stiffness and deformation of Hostun sand under drained cyclic loading**. 2014. 395 p. PhD thesis (Doctor of Philosophy in the Faculty of Engineering) – Department of Civil Engineering, University of Bristol, Bristol, UK, 2014.

FERREIRA, C. A. **Estudo do comportamento mecânico de solos reforçados com fibras através do método de elementos discretos**. 2010. 118 p. MSc Dissertation (Master of Civil Engineering) – Department of Civil Engineering, Pontifical Catholic University of Rio de Janeiro (PUC-Rio), Rio de Janeiro, Brazil, 2010.

FESTUGATO, L. **Análise do comportamento mecânico de um solo micro-reforçado com fibras de distintos índices aspecto**. 2008. 146 p. Dissertation (Master in Engineering) – Programa de Pós-Graduação em Engenharia Civil, PPGEC/UFRGS, 2008.

FESTUGATO, L. **Comportamento de hidratação e resposta cisalhante cíclica de resíduo de mineração cimentado reforçado com fibras**. 2011. 224 p. PhD Thesis (Doctor of Engineering) – Programa de Pós-Graduação em Engenharia Civil, PPGEC/UFRGS, 2011.

FEUERHARMEL, M. R. **Comportamento de solos reforçados com fibras de polipropileno**. Porto Alegre, 2000. 131 p. Dissertation (Master in Engineering) – Programa de Pós-Graduação em Engenharia Civil, PPGEC/UFRGS, 2000.

FREITAG, D. R. Soil randomly reinforced with fibers. **Journal of Geotechnical Engineering**, v. 122, n. 3, p. 823-826, 1986.

FLOREZ, J. H.; FESTUGATO, L.; CONSOLI, N. C. C. Efeito da adição de fibras na resposta ante carregamentos cíclicos em areias limpas. In: CONGRESSO BRASILEIRO DE MECÂNICA DOS SOLOS E ENGENHARIA GEOTÉCNICA, 13th, 2016, Belo Horizonte, Brazil. **Proceedings**, ABMS, 2016.

GAJO, A.; MUIR WOOD, D. Severn-Trent sand model: a kinematic-hardening constitutive model: the q-p formulation. **Géotechnique**, v. 49, n. 5, p. 595-614, 1999.

GRAY, D. H.; OHASHI, H. Mechanics of fiber reinforcement in sand. **Journal of Geotechnical Engineering**, v. 109, n. 3, p. 335-353, 1983.

GRAY, D. H.; AL-REFEAI, T. Behavior of fabric versus fiber reinforced sand. **Journal of Geotechnical Engineering**, v. 112, n. 8, p. 804-820, 1986.

HANNANT, L. Polymers and composites. In: ILLSTON, J. M. **Construction materials: their nature and behavior**. 2. ed. London: J. M. Illston & FN Spon, 1994, p. 359-403.

HARDIN, B. O.; BLACK, W. L. Sand stiffness under various triaxial stresses. **Journal of the Soil Mechanics and Foundation Division**, v. 92, n. 2, p. 353-369, 1966.

HEINECK, K. S.; COOP, M. R.; CONSOLI, N. C. Effect of microreinforcement of soils from very small to large shear strains. **Journal of Geotechnical and Geoenvironmental Engineering**, v. 131, n. 8, p. 1024-1033, 2005.

IBRAIM, E.; DIAMBRA, A.; MUIR WOOD, D.; RUSSEL, A. R. Static liquefaction of fibre reinforced sand under monotonic loading. **Geotextiles and Geomembranes**, v. 28, p. 374-385, 2010.

IBRAIM, E.; MUIR WOOD, D.; MAEDA, K.; HIRABAYASHI, H. Fibre-reinforced granular soils behaviour: numerical approach. In: INTERNATIONAL SYMPOSIUM ON GEOMECHANICS AND GEOTECHNICS OF PARTICUALTE MEDIA, 2006, Ube, Japan. **Proceedings**... London: CRC Press, 2006, p. 443-448.

ISHIHARA, K. **Soil Behaviour in Earth Geotechnics**. Oxford Engineering Science Series. Oxford: Oxford University Press, 1996.

JEWELL, R. A. **Some factors which influence the shear strength of reinforced sand**. CUED/D-Soils/TR85, Cambridge University Engineering Department, Cambridge, 1980.

JOHNSTON, C. D. Fibre-reinforced cement and concrete. In: JOHNSTON, C. D. (Ed.). **Advances in concrete technology**. 2. ed. Otawwa: Malhorta, 1994, p. 603-673.

KATZ, V. The history of Stoke's Theorem. **Mathematics Magazine**, n. 52, p. 146-156, 1979.

KOERNER, R. M.; WELSH, J. P. **Construction and Geotechnical Engineering Using Synthetic Fabrics**. New York: Wiley Series of Practical Construction Guides, 1980.

KOERNER, R. M. **Designing with Geosynthetics**. 6th ed. Bloomington, USA: Xlibris Corp., 2012. v. 1.

LEE, K. L.; ADAMS, B. D.; VAGNERON, J. M. Reinforced earth retaining walls. **Journal of Soil Mechanics and Foundations Division**, v. 99, n. 10, p. 745-764, 1973.

LI, C.; ZORNBERG, J. G. Validation of discrete framework for fiber-reinforcement. In: NORTH AMERICAN CONFERENCE ON GEOSYNTHETICS, Winnipeg, Canada. **Proceedings...** Winnipeg: NAGS, 2003.

LI, J.; DING, D. W. Nonlinear elastic behavior of fiber-reinforced soil under cyclic loading. **Soil Dynamics and Earthquake Engineering**, v. 22, p. 977-983, 2002.

MACHADO, S. L.; CARVALHO, M. F.; VILAR, O. M. Constitutive model for municipal solid waste. **Journal of Geotechnical and Geoenvironmental Engineering**, v. 128, n. 11, p. 940-951, 2002.

MAEDA, K.; IBRAIM, E. DEM analysis of 2D fibre-reinforced granular soils. In: INTERNATIONAL SYMPOSIUM ON DEFORMATION CHARACTERISTICS OF GEOMATERIALS, 4th, 2008, Atlanta, USA. **Proceedings**… Atlanta: IOS Press, 2008 p. 623-628.

MAHER, M. H.; GRAY, D. H. Static response of sands reinforced with randomly distributed fibers. **Journal of Geotechnical Engineering**, v. 116, n. 11, p. 1661-1667, 1990.

MAHER, M. H.; HO, Y. C. Behavior of fiber-reinforced cemented sand under static and cyclic loads. **Geotechnical Testing Journal**, Philadelphia, v. 16, n. 3, p. 330-338, 1993.

MCGOWN, A.; ANDRAWES, K. Z.; AL-HASANI, M. M. Effect of inclusion properties on the behaviour of sand. **Géotechnique**, London, v. 28, n. 3, p. 327-346, 1978.

MICHALOWSKI, R. L.; ZHAO, A. Failure of Fiber-Reinforced Granular Soils. **Journal Geotechnical Engineering**, v. 122, n. 3, p. 226-234, 1996.

MICHALOWSKI, R. L.; CERMAK, J. Strength anisotropy of fiber-reinforced sand. **Computers and Geotechnics**, v. 29, p. 279-299, 2002.

MICHALOWSKI, R. L.; CERMAK, J. Triaxial compression of sand reinforced with fibers. **Journal of Geotechnical and Geoenvironmental Engineering**, v. 129, n. 2, p. 125-136, 2003.

MUIR WOOD, D. **Soil Behaviour and Critical State Soil Mechanics**. Cambridge: Cambridge University Press, 1990.

MUIR WOOD, D. **Geotechnical Modelling**. London: CRC Press, 2004, v. 1.

NOORZAD, R.; AMINI, P. F. Liquefaction resistance of Babolsar sand reinforced with randomly distributed fibers under cyclic loading. **Soil Dynamics and Earthquake Engineering**, 66, p. 281-292, 2014.

RALSTON, A.; RABINOWITZ, P. **A First Course in Numerical Analysis**. 2nd. ed. New York: Dover Publications, 1978.

RAM, B. **Engineering Mathematics**. Chennai, India: Pearson Education India, 2009.

RANJAN, G.; VASAN, R. M.; CHARAN, H. D. Probabilistic analysis of randomly distributed fibre reinforced soil. **Journal of Geotechnical Engineering**, v. 122, n. 6, p. 419-422, 1996.

ROSCOE, K. H.; BURLAND, J. B. **On the generalized stress-strain behaviour of wet clay**. In: CONFERENCE IN ENGINEERING PLASTICITY. Papers. Cambridge, UK: Cambridge University Press, 1968, p. 536-609.

ROWE, P. W. **The stress-dilatancy relation for static equilibrium of an assembly of particles in contact**. In: ROYAL SOCIETY OF LONDON. Proceedings Series A, 269. London: Mathematical and Physical Sciences, 1962. p. 500-527.

SALAMATPOOR, Sina; SALAMATPOOR, Siavash. Evaluation of Babolsar sand behaviour by using static triaxial tests and comparison with case history. **Open Journal of Civil Engineering**, v. 4, p. 181-197, 2014.

SCHOFIELD, A. N.; WROTH, C. P. **Critical State Soil Mechanics**. London: McGraw-Hill, 1968.

SIVAKUMAR BABU, G. L.; VASUDEVAN, A. K.; HALDAR, S. Numerical simulation of fiber-reinforced sand behavior. **Geotextiles and Geomembranes**, v. 26, p. 181-188, 2008.

TEODORO, J. M.; BUENO, B. S. **Estudo do comportamento de solos reforçados com fibras plásticas de polipropileno**. In: CONGRESSO BRASILEIRO DE MECÂNICA DOS SOLOS E ENGENHARIA GEOTÉCNICA, 11, Brasília, 1998. **Anais**… v. 2, p. 1093-1100, 1998.

ULBRICH, L. A. **Aspectos do comportamento mecânico de um solo reforçado com fibras**. Porto Alegre, 1997. 122 p. Dissertação (Mestrado em Engenharia) – Programa de Pós-Graduação em Engenharia Civil, PPGEC/UFRGS, 1997.

VELLOSO, R. Q.; CASAGRANDE, M. D. T.; VARGAS JUNIOR, E. A.; CONSOLI, N. C. Simulation of the mechanical behavior of fiber reinforced sand using the Discrete Element Method. Soils and Rocks, v. 35, n. 2, p. 201-206, 2012.

VILLARD, P.; JOUVE, P. Behaviour of granular materials reinforced by continuous threads. **Computers and Geotechnics**, v. 7, p. 83-98, 1989.

VILLARD, P.; JOUVE, P.; RIOU, Y. Modélisation du compertment mécanique du Texsol. **Bullétin de liaison des laboratoires de ponts et chaussées**, v. 168, p.15-28, 1990.

WALDRON, L. J. The shear resistance of root-permeated homogeneous and stratified soil. **Soil Science Society of America Journal**, vol. 41, p. 843-849, 1977.

WICHTMANN, T.; TRIANTAFYLLIDIS, T. Behaviour of granular soils under environmentally induced cyclic loads. In: DI PRISCO, C.; MUIR WOOD, D. (Eds.). **Mechanical Behaviours of Soils under Environmentally Induced Cyclic Loads**. v. 534. Udine, Italy: Springer, 2012, p. 1-136.

WU, T. H.; MCKINNEL, W. P. III; SWANSTON, D. N. Strength of tree roots and landslides on Prince of Wales Island, Alaska. **Canadian Geotechnical Journal**, Ottawa, Canada, v. 16, n. 1, p. 19-33, 1979.

YETIMOGLU, T.; SALBAS, O. A study on shear strength of sands reinforced with randomly distributed discrete fibers. **Geotextiles and Geomembranes**, v. 21, p. 103-110, 2003.

YU, H. S. **Plasticity and Geotechnics**. New York: Springer, 2006.